CRANFIELD UNIVERSITY

SURYANARAYANAN KRISHNASWAMY

MANUFACTURING OF NOVEL AEROGEL BASED THERMAL COATING SYSTEMS FOR CARBON/EPOXY COMPOSITE SUBSTRATES

SCHOOL OF AEROSPACE, TRANSPORT AND MANUFACTURING
Transport Systems

PhD
Academic Year: 2017 - 2018

Supervisor: Dr. Hrushikesh Abhyankar
Associate Supervisor: Dr. Zhaorong Huang
June 2018

CRANFIELD UNIVERSITY

SCHOOL OF AEROSPACE, TRANSPORT AND MANUFACTURING
Transport Systems

PhD

Academic Year 2017 - 2018

SURYANARAYANAN KRISHNASWAMY

MANUFACTURING OF NOVEL AEROGEL BASED THERMAL COATING SYSTEMS FOR CARBON/EPOXY COMPOSITE SUBSTRATES

Supervisor: Dr. Hrushikesh Abhyankar
Associate Supervisor: Dr. Zhaorong Huang
June 2018

Abstract

To try and increase the applicability of carbon fibre composites, the present work considers the use of thermal coatings on its surface. After a study on relevant literature pertaining to conventional and alternate thermal barrier coatings, it was believed that YSZ-based and/or aerogel-based systems had the most potential. But successful application of these coatings required additional research, particularly on processing routes and long-term performance. Therefore to try and achieve a more efficient thermal coating on composite substrates, aerogel-based materials were investigated since they showed the most promise. These aerogel/polymer composites were further characterized using different morphological, optical and thermal techniques. The experimental results showed particularly promising trends for aerogel/epoxy materials whose best sample had an aerogel damage coefficient value of 18.3%. Hence, this system was applied as a coating on a carbon fibre reinforced polymer substrate and the whole system showed better thermal performance compared to a pure epoxy coating. The coating and the substrate were subsequently modelled and solved using finite element analysis to determine the most effective system under a cyclic thermal load. Although, the selection of the coating type (double, top or bottom) is dependent on the exact application; the top coating displayed the best performance balance. Nevertheless, both, experimental measurements and simulation results in the current work point to a potential application of the coating in industries such as aerospace, automotive and/or construction.

Keywords: Composites, Aerogels, Coating, Thermal Conductivity, Finite Element Analysis, Damage Coefficient

Acknowledgements

I would firstly like to thank my parents for their tireless and unconditional love. Without their support, I couldn't have even started this venture, let alone finish it and this would have remained a distant dream. From buying my first LEGO set to helping me make career choice, their relentless faith has no equal; mere words wouldn't do them justice! Next, my sister, she has managed to find that thin line between a sibling and a friend that still remains elusive to me. As an elder brother, I am incredibly proud of her achievements which show no signs of slowing down.

Coming to Cranfield and carrying out research in a topic that was new to me was a daunting task. But fortunately, I had the support and the assistance of my supervisor Dr. Hrushikesh Abhyankar who made the whole process effortless and enjoyable. Rishi's guidance and knowledge was irreplaceable and ensured that my love for the subject remained untarnished even after multiple days (sometimes months) of frustration. I must also thank my associate supervisor Dr. Zhaorong Huang for suggesting the idea of aeorgels and helping me plan and execute multiple experiments along with their data analysis. Speaking of data analysis, I am also greatly indebted to Dr. Veronica Marchante for spending countless hours helping me plan and understand experimental procedures along with the number crunching afterwards, be it hand calculations or writing a MATLAB script. I am also extremely thankful to Prof Mark Savill for advising me on the general direction of my research and giving me invaluable suggestions on ways to improve it. I would also like to extend my gratitude to the entire motorsport group at Cranfield led by Dr. James Brighton for inspiring me further with their world-class research endeavours.

I would also like to use this opportunity to thank the technical officers and other staff members at the university- Andrew Stallard, Steve Pope, Dr. Lawrence Cook, Dr. Pavan Addepalli, Lawrence Tinsley, Dr. Chris Shaw, Simon Stranks, Abdenour Achour, Dr. Christine Kimpton, Dr. Vijay Kumar Thakur, Dr. Debabrata Bhattacharyya, Dr. Alex Skordos and everyone else for their assistance throughout the course of this work. A special mention

to Jim Hurley, Ben Hopper and Dr. David Ayre who went out of their way to help me prepare, test and analyse the numerous samples during the course of my work; this work and the experience would have been completely different without them around. I would also like to thank Mr Thomas Buss at the University of Nottingham for his assistance with the direct thermal conductivity measurements.

I have also been fortunate enough to have met some wonderful people over the last few years; thank you Josh, Arun, Sravan, Jose and Paras for just being there! My office mates (past and present) Ian, Satya, Laura (s), Abu, Chris and Jonathan for all the advice, movies and activities! Of course, the greatest thing that has happened to me whilst in Cranfield was love! I met Ximena towards the final year of my studies and my only regret is that it didn't happen sooner. She has stood by me through thick and thin and has always supported and encouraged me to reach new heights. Thank you so much for everything (and Oreo of course)!

I am also deeply thankful to Prof Raghuraman and Dr Doni Daniel for rekindling the lamp of curiosity within me, my uncle Jayaram for his advice and guidance, my cousin's Kasturi, Champa, Savithri, Sunil and Badri for putting up with me, my extended family and grandparents, Srikanth (and the rest of IBEX) for giving me the opportunity to work in their company and learning things I wouldn't have even thought about and, Eshan, Vishwas, PB, Praveen, Raghav, Rohit, Billy, Nischal, DK, Anirudh and the rest of the Bangalore crew. I feel this would not be complete without thanking all my teachers and lectures, as each day goes by, I realise the importance of their tireless and (often) thankless task more and more. Finally, I would like to express my gratitude to 'Akka' for all patient guidance and counselling I have been lucky enough to receive, thank you.

Contents

List of Figures

List of Tables

Common Abbreviations

CFRP –	Carbon fibre reinforced Polymer
DSC -	Differential scanning calorimetry
EDX -	Energy dispersive spectra
FE -	Finite Element
FT-IR -	Fourier transform infrared spectroscope
FT-IR -	Fourier transform infrared spectroscope
HGM-	Hollow glass microspheres
hrs -	Hours
IPA -	Isoproponol
mins -	Minutes
PA -	Polyamide
SEM -	Scanning electron microscope
SN curve-	Stress-Number of cycles curve
TBC -	Thermal Barrier Coating
TGO -	Thermally Grown Oxide
XRD -	X-ray diffraction
YSZ -	Ytrria stabilised Zirconia

List of Publications associated with the current work*

1) **Krishnaswamy, S**., Tinsley, L., Marchante, V., Addepalli, S., Huang, Z., & Abhyankar, H. (2018). Effect of extrusion and compression moulding on the thermal properties of nylon-6/silica aerogel composites. *Journal of Thermoplastic Composite Materials*, *31*(7), 992–1009. https://doi.org/10.1177/0892705717729198
2) **Krishnaswamy, S**., Bhattacharyya, D., Abhyankar, H., Marchante, V., Huang, Z., & Brighton, J. (2018). Morphological, optical and thermal characterisation of aerogel-epoxy composites for enhanced thermal insulation. *Journal of Composite Materials*. https://doi.org/10.1177/0021998318793194
3) **Krishnaswamy, S.,** Abhyankar, H., Marchante, V., Huang, Z. & Brighton, J. (2019). Aerogel/epoxy thermal coatings for carbon fibre reinforced plastic substrates. *Journal of Adhesion Science and Technology*. https://doi.org/10.1080/01694243.2018.1558476
4) **Krishnaswamy S**., Marchante V., Abhyankar H., Huang Z. & Brighton J. (2019) Non Isothermal cure kinetics of Aerogel/Epoxy composites using Differential Scanning Calorimetry, *Polymer-Plastics Technology and Materials*. https://doi.org/10.1080/25740881.2019.1576194

*Information at the time of submission

1 Introduction

The application of thermal coatings is a critical cost and energy saving measure for many materials used in a medium-high temperature environment. According to one article [1], the TBC market is expected to grow from a revenue of $14,643.8 million (USD) in 2017 to opportunities worth $22,497.0 million (USD) by 2024. Another report [2] valued the thermal insulation coating market at $6,660.5 million (USD) in 2016. The same report also identified manufacturing, automotive and transportation, building and construction and, aerospace and defence as the major contributors to the market. If just one of the above mentioned industries (aerospace) is considered, it is estimated that annual fuel savings for a 250 aircraft fleet could be as high as 38 million litres, if the TBC's were applied successfully to all high temperature aerofoils in a modern gas turbine engine [3]. Similarly, it is believed that the introduction of thermal coatings onto carbon fibre reinforced polymers would increase the operating temperature of the composites and widen their application thereby further reducing costs and energy consumption.

Therefore, this study looks to create an effective thermal insulation coating for carbon fibre reinforced polymers (CFRPs) by identifying the suitable materials and processes along with the relevant characterisation and experimental data. Although conventional TBC's are expected to work in extreme environments and temperatures, the materials in the present study are subjected to much lower temperatures (~100°C) since one of the main objectives of the present work is to increase the service life of CFRPs operating at elevated temperatures between 50-100°C.

To achieve this, the present work first identifies certain key properties required for thermal barrier coatings (TBCs) using existing research. Next, the importance of carbon fibre composites will be described thereby signalling the importance of the

current work. Once this is undertaken, the relevant literature surrounding traditional TBCs and their application process will be studied and their limitations identified. As an alternative to these materials, there will also be a study of other insulators, which may be able to satisfy the requirements of a carbon fibre reinforced plastic (CFRP) substrate. The chapter will end by summarising the reviewed studies through the identification of gaps/additional research and subsequently using them as the aim (and additional objectives) of the present work. Then, the work will move onto the description of different methods used to process the materials considered in this study, this will be then be followed by a list and explanation of the various experimental apparatus and, modelling techniques used. The results from these experiments and models will subsequently be presented in chapter 4. Using the results, the material's performance will be discussed and put into perspective with assistance from relevant literature (if and where possible). The results will likewise be used to determine if the objectives of the study have been met. Finally, the work will conclude by summarising the key points and findings of the study together with suggestions of possible areas for future research that could improve and add to the existing data given here.

1.1 Properties of Thermal Barrier Coatings

According to Hocking et al., [4] the main requirement of a protective surface (i.e., coating) is to have "qualities superior to that of the substrate in order to shield the component from an aggressive environment". Keeping this in mind, some basic properties to be considered while selecting a TBC coating system are [5][6][7][8]:

1. High melting points
2. Low thermal conductivity
3. Phase stability between room and operation temperature

4. Good adherence between the substrate and the coating (if a multi-layer system is adopted, the other layers must be considered as well)
5. Chemical inertness
6. Thermal expansion match between the coating and substrate (and other layers in a multi-layered system)
7. Low sintering rate of microstructure
8. Low rate of oxidisation and corrosion (of all the layers)

Amongst these, thermal conductivity and thermal expansion coefficient are seen to be the most critical parameters [5]. The TBCs must also be able to maintain these properties for extended service times and multiple thermal cycles and must remain intact during heating, cooling and sometimes, thermal shock [9]. Additionally, depending on the application, there may be a requirement to satisfy a specific property in addition to the ones mentioned above, such as the application of TBCs in gas turbine engines, wherein the effects due to the resistance to CMAS (calcium magnesium- alumina- silicate) attack, low weight and operation at gas velocities greater than Mach 1 [9] must also be taken into account.

Although the requirements for the TBCs may be numerous and quite often, difficult to achieve, the benefits gained by the successful application of these coatings outweigh any other drawbacks and issues. For example, an almost 50% increase in the efficiency of a gas turbine engine is predicted for a design which doesn't utilise auxiliary cooling (the application of which can be reduced or removed by TBCs) without even considering the other accompanying benefits such as the weight saved and the complexity of the cooling system [10].

2 Literature Review

2.1 Carbon fibre Composites

Although Carbon composites exhibit a large strength to weight ratio and excellent retention of high temperature properties such as modulus and strength in an inert atmosphere, high thermal conductivity and shock resistance, low coefficient of thermal expansion (CTE) and recession in ablative environments [11][12][13], carbon/epoxy composites are thermally limited by the degradation of the resin (as discussed in section 2.1.2.1). Additionally, composite materials are resistant to corrosion and fatigue in most cases [14], making them an ideal choice for various high performance applications in the aerospace and automotive industry (amongst many others). Examples of these applications include the use of carbon fibre composites in the wings of combat aircraft, carbon/carbon in disc brakes, carbon/carbon or silicon carbide/silicon carbide in rocket engine nozzles [15] for the aerospace industry. There are also instances of aircrafts/gliders made completely from composites such as the Beech Starship aircraft and the Marrianne Centrair Airplane [14]. In the automotive industry application of composites is limited to high performance race cars and high-end luxury vehicles primarily due to the higher cost of these materials [16]. The use of carbon/epoxy in the cross beam and honeycomb/carbon/epoxy in the body of a Ferrari F1 racing car [14], carbon fibre in the battery box of a Formula E car [17] illustrate this point. However, this scenario might change in the future with companies like BMW, General Motors, Toyota, Ford, Aston Martin etc., showing interest in carbon composites [16].

2.1.1 Processing of Carbon Fibres

Although, the precursors used to manufacture carbon fibres are varied, the basic method of preparation is similar (as illustrated in Figure 1). Since, Polyacrylonitrile (PAN) and Pitch based fibres are the two most common types of precursor materials for carbon fibre, they alone are considered in this work. The properties of a fibre are primarily guided by its major structural parameters; orientation, crystallinity and defect content [18].

Figure 1 Carbon Fibre Production. Taken from Dienfendorf in [19], and [20]

2.1.1.1 PAN Fibres

PAN fibres are forms of textile fibres and are currently, the most common precursors used in the production of carbon fibres. They have a density of approximately 1.17 g/cm^3 and are white in colour [20]. According to Bunsell & Renard [21], the following steps are employed in the manufacture of PAN fibres:

- Heating in the presence of air to about 250°C with the PAN fibres held in tension. This ensures that the fibres are made infusible by cross linkages
- Heating in a nitrogen atmosphere at 1000°C. At this temperature, both oxygen and hydrogen are removed and only nitrogen (7% weight) remains
- Further heating removes the nitrogen as well and at approximately 1500-1600°C, a whole/pure carbon fibre is attained

After this, a surface treatment is advised to ensure that there is a proper bonding between the fibres and the matrix (this usually involves the creation of carboxyl, carbonyl and hydroxyl groups on the surface of the fibre) [20]. The fibres produced using PAN display a diameter of 7 μm, although diameters of 5 μm (higher strength) are possible through improvements in drawing techniques and precursor quality [21].

The popularity of PAN based carbon fibres can be put down to them generating carbon fibres with a balance in properties such as high tensile and compressive strengths, low modulus, high strain rates at failure [18][20]. The low modulus of these fibres can also be see in Table 1 wherein, the 'high modulus' PAN fibres show lower values of tensile modulus as compared to their pitch-based counterparts. Finally, PAN fibres also have the added benefit of being able to be spun easily into highly oriented fine fibres [22].

2.1.1.2 Pitch Fibres

Pitch is a mixture of aromatic hydrocarbons and is derived from petroleum, asphalt, PVC or coal tar (Donnet & Bansal in [20]). The high yield of carbon (close to 90%) makes it a cheap and attractive choice, however the purification costs of the fibre must be kept in mind [21].To align the precursor fibres for high performance carbon fibres, the pitch must be converted into a mesophase/liquid crystal solution by heating it to a temperature of 400-450°C [21]. After this, the production sequence is similar to that of PAN fibres with only the process parameters such as temperatures, time and ramp rates being different [20].

One advantage of pitch based fibres is that unlike PAN fibres, they do not peak in strength at 1500°C which makes it more economical to produce high modulus carbon fibres however, their increased costs and difficulty in production must be considered [21]. Other advantages include superior axial thermal and electrical conductivity, high

axial modulus (fibres which approach the theoretical value of 1000GPa for graphite crystals have been produced) and negative coefficient of thermal expansion [20][18][22]. One drawback of pitch-based fibres is their poor compressive strength which, Pilato & Michno [18] put down to the fibres microstructure that is sensitive to shear.

A list of certain common properties for PAN-based and pitch-based fibres is given in Table 1. A point to remember is that Table 1 doesn't give the final properties of the composite; it only serves as a guideline. For a more comprehensive treatment, the matrix must also be considered.

Table 1 Properties of Carbon Fibres. Data taken from [20]

Precursor	**Modulus**	**Tensile Modulus (GPa)**	**Tensile Strength (MPa)**	**Elongation at break (%)**	**Thermal Conductivity (W/(mK))**	**Coefficient of Thermal Expansion (Axial Direction) (10^{-6} K)**	**Density (g/(cm^3))**
PAN-based Fibres	Standard Modulus	220-241	3450-4830	1.5-2.2	20	-0.4	1.8
	Intermediate Modulus	290-297	3450-6200	1.3-2.0	20	-0.55	1.8
	High Modulus	345-448	3450-5520	0.7-1.0	50-80	-0.75	1.9
Pitch-based Fibres	Low Modulus	170-241	1380-3100	0.9	N/A	N/A	1.9
	High Modulus	380-620	1900-2750	0.5	N/A	-0.9	2.0
	Ultra-High Modulus	690-965	2410	0.4-0.27	400-110	-1.6	2.2

2.1.2 Limitations of carbon fibre composites

Although carbon/epoxy composites are viewed as prime candidates for various applications, there are certain drawbacks and limitations that the designers and

engineers must take into account/rectify before the material is implemented successfully. Apart from their higher cost, composite materials exhibit low impact resistance, fracture toughness and ductility [14][15]. The operating temperatures of the polymers also limit the polymer matrix composites' usage as discussed earlier. From the examples given in Peel's [15] work, it is seen that only two (out of five) polymers have their maximum operating temperatures in excess of 200°C: thermoset polyamides and semi-thermoplastic polyether ether ketone (PEEK). Another, perhaps a more critical drawback for high temperature applications, is the oxidation (and subsequent burning) of carbon at and over 500°C [23][24]. Therefore, there is a great interest in reducing the rate of oxidation of these materials. Smeacetto et al. [23] and Smeacetto et al. [25] considered the use of oxygen inhibitors or coatings to mitigate this problem. It was soon found out that although inhibitors slow the oxidation, they are not efficient for extended use at temperatures greater than 900°C [25]. Hence, the coating of the base composite with appropriate refractory materials is seen as the most viable route [13][26].

In the present work, the first of the material's drawbacks is mitigated through the development and application of a coating on its surface thereby allowing the application of carbon fibre composites at elevated temperatures.

2.1.2.1 Thermal degradation of CFRP

These limitations, like the low operating temperature of epoxy, result in the degradation of CFRP performance at higher temperatures. The thermal degradation (as a function of temperature) of CFRP, GFRP (Glass fibre reinforced plastics) and their hybrids are shown by Vanaja & Rao [27] using DSC thermograms. In their study, the resin and the reinforcements start to degrade at 250°C and 300°C respectively with the former showing much greater degradation levels (thereby further

proving the greater contribution of the resin to this process). As a result, the thermal degradation contributes to the reduction in mechanical performance of the composites as seen in the work of Wolfrum et al. [28] who noticed an increased mass loss with higher aging temperatures and a significant reduction in mechanical strength when the CFRP specimens were aged between 180^0C to 200^0C. The authors also noticed that thermal degradation primarily occurs in the epoxy matrix using IR spectra data. In another study, Justo et al. [29] observed a decrease in fatigue life for certain configurations of CFRP perhaps due to increased thermal stresses as a result of higher testing frequencies. Naruse et al. [30] also observed a reduction in fatigue strength of CFRP rings with an increase in degradation temperature (at constant time) as well as degradation time (at constant temperature). The reliance of fatigue strength on temperature was also seen in another study by Nakada et al. [31] who, showed that the flexural fatigue strength (in the transverse direction) of unidirectional CFRP is dependent on the testing temperature, frequency and number of cycles.

Therefore, the findings of various literature discussed above indicate a dependence of mechanical performance with operating (testing) temperatures, further corroborating the need for thermal coating systems on CFRP substrates.

2.2 Conventional Thermal Barrier Coatings

This section explores the more common thermal barrier coatings used in the aerospace industry presently. It was thought that this part of the review would serve as a good starting point for the study and also assist in the identification of potential candidates from existing TBC materials that could be used to coat CFRP substrates. The use of thermal barrier coatings (TBCs) to increase the inlet temperature (and hence, its thermodynamic efficiency) of a gas turbine and other similar engines is seen as one of

its prime benefits; Figure 2 describes a cross sectional view of a turbine blade along with the structure of a typical Thermal Barrier Coating (TBC).

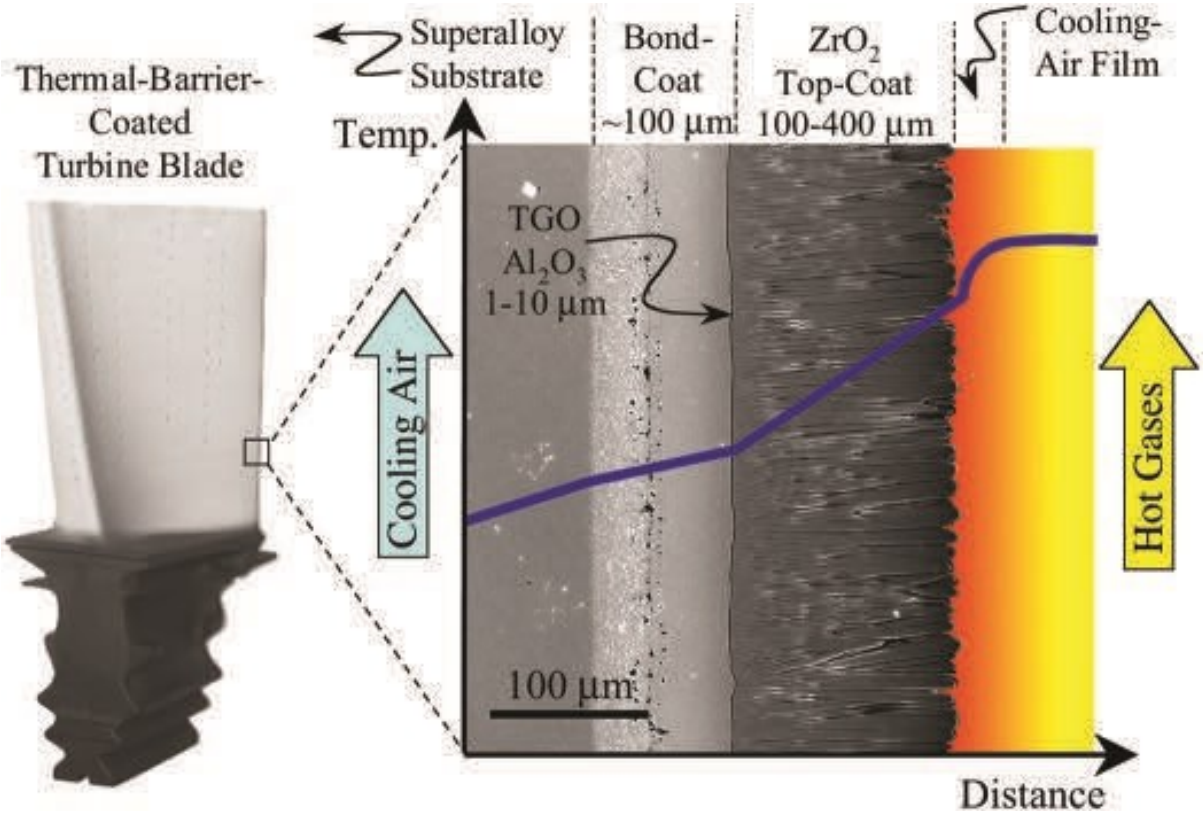

Figure 2 A Turbine Blade with the structure of a typical TBC, from [32]

In this section the existing and current literature surrounding TBCs are considered to investigate the possibility of their application onto the carbon fibre substrate. It must be noted that although mechanical properties such as Young's Modulus, hardness, fracture toughness, etc., are considered an integral part of any comprehensive study for TBC materials, it is believed that the thermal properties such as thermal conductivity, Coefficient of Thermal Expansion (CTE) and thermal cycling tests are more critical to the TBC performance. Hence this study limits itself to these parameters but where required, the other properties are also mentioned.

It is expected that materials with low thermal conductivity will have a low specific elastic modulus, loose bonding, high average atomic weight and, disordered structures [33] and according to Cao et al. [5], the oxides of materials who find application as

TBCs are usually found in IIIB, IVB, IIIA, IVA of the periodic table and groups IIA contain the stabilisers used for zirconia

2.2.1 Stabilised Zirconia

Zirconia has been stabilised with various materials such as ceria, ytrria, gadolinia etc., most of whom have shown promising results.

The addition of ceria into yttria stabilised zirconia (YSZ) can reduce the thermal conductivity, increase phase stability and the thermal cycling life of the coating [34][5](Brandon and Taylor, 1989 & 1991 in [35]). According to Schulz et al. [34], ceria stabilised zirconia shows a quasi-continuous weight loss during burner rig testing wherein, there was a layer-by-layer loss of the material; the authors remark that this could be a result of the change in the composition across the thickness of the coating. However, the large difference in the vapour pressures of ceria and zirconia as well as the sublimation of the former (in vacuum) could lead to potential problems during deposition [36].

Munawar et al. [37] investigated two other stabilising agents for zirconia- gadolinia (GdZ) and dysprosia (DySZ); it was seen that both the new materials showed similar or better lifetime than 7YSZ on a NiCoCrAlY bond coat, GdZ also exhibited a non-uniform sintering pattern with higher rates at the column tips compared to DySZ, 7YSZ and also the lower sections of same column. The study showed that GdZ withstood up to ≈2750 cycles, DySZ up to ~1750 cycles and 7YSZ up to ≈750 cycles under similar conditions and interestingly, the double layered coatings of the two materials (with 7YSZ) had lower cyclic lifetimes than their single layered counter parts. It must also be noted that these results were affected by the bond coat composition and the deposition technique used.

Another study considered La_2O_3 stabilised zirconia (LaSZ) and fully yttria stabilised zirconia (FYSZ) in which both showed rapid spallation and poor cyclic lifetimes [34], the same study also showed that 6.5 wt% partially stabilised zirconia (PYSZ) was extremely stable and had a higher lifetime compared to the former materials. This is because of the metastable tetragonal phase (t') which shows high crack propagation energy, excellent bending strength, good fracture toughness and a good thermoshock behaviour [34].

However, not all stabilising agents resulted in good performance and practicality: Stabilization with CaO and MgO resulted in performance lower than YSZ [38] and the high cost of the raw material in scandia stabilisation is a potential drawback [36].

2.2.1.1 YSZ

Since YSZ has been the standard TBC, the material has benefited from extended research on the coating process and bond coat chemistry optimisation for more than 20 years [38]. The addition of yttria (large defect concentration) changes the vibrational modes from well-defined wavevectors and polarizations to more randomised excitations, as a result they move more slowly and hence, lower conductivity [33]. These coatings are also almost transparent to oxygen diffusion because of their high concentration of oxygen ion vacancies, which in turn, helps the formation of the thermally grown oxide (TGO) layer [5]. However, the exact amount of stabilizer is critical since a higher amount would lower the toughness value and lower amounts would result in phase transformations at lower temperatures [39].

One study [40] explored the oxidation of 8wt% PYSZ and inferred that the oxidation rate follows the parabolic law and after a 500hrs at 1100°C, the coating experienced the effects of degradation which subsequently resulted in a partial spallation of zirconia after 1500hrs. Nevertheless, the addition of alumina to the YSZ results in a

coating with higher hardness and a better oxidation resistance [5]. It is seen that an additional Al_2O_3 layer on top of the YSZ layer (Al_2O_3/YSZ) reduces the rate of TGO growth resulting in a reduction of oxidised area from 32% for an YSZ coating to 19% for Al_2O_3/YSZ coating [41].

A major drawback of using YSZ coatings is that lifetime of the coatings reduces dramatically once the temperature reaches 1300°C due to a phase transformation from the metastable non-transformable tetragonal structure to an equilibrium cubic and tetragonal structure resulting in a further transformation of the latter into a monoclinic structure (10-19% content) on cooling (which is accompanied by a 3-4% volume expansion) [42]. The mechanisms and some of the factors affecting this phase transformation are discussed in more detail in [43][44][45].

Because of the limitations of YSZ coatings, there is a search for more efficient coating systems that could be used in higher operating conditions. One method to reduce the phase transformation of YSZ could be the use of thick coatings (1.5mm) as demonstrated by Guo et al. [46], who found only a small content of monoclinic phase even after 1770 cycles at 1238°C and 320 cycles at 1335°C for one of their coatings; these coatings also demonstrated comparable thermal conductivities and coefficient of thermal expansions (CTE) at 1.3 W/(m*K) to 1.75 W/(m*K) (depending on the coating microstructure) and 11.2 X 10^{-6} K^{-1} (the average CTE between room temperature and 1200°C) respectively. Other potential candidates include the application of binary and/or ternary oxides to zirconia; binary coatings such as La_2O_3/7 P-YSZ, Nd/Yb, Gd/Yb and Sm/Yb have been reported to be successfully tested; however ternary systems like Gd/Yb/Sc and Nb/Yb/Sc did not improve the existing thermal isolation properties [33]. But a coating made up of zirconiaand Y_2O_3, Yb_2O_3 and, Gd_2O_3 showed lower conductivities before and after sintering at 1316°C

for 20 hours; 1.20 W/(m*K) and 1.64 W/(m*K) compared to 7YSZ's 1.45 W/(m*K) and 2.20 W/(m*K) respectively [47]

2.2.2 Mullite

The crystal structure of mullite and its more simpler relative- sillimanite is reviewed in detail by Schneider et al. [48]. Mullite has a lower TEC/CTE and is more resistant to oxygen than YSZ, however it also has a higher thermal conductivity [5]. The TEC of mullite is between 3.9 X 10^{-6} K^{-1} and 4.5 X 10^{-6} K^{-1} (300°C - 1000°C) depending on the composition with value being lowered even further by doping the compound with Cr wherein a value of 3.1 X 10^{-6} K^{-1} has been observed ((Schneider & Eberhard and Schreuer et al. in [48]). Additionally, Mullite along with Al_2O_3 and SiC deposited on a carbon/carbon composite showed no major cracks when the sample was cycled nine times between room temperature and 1600°C and, the specimen also exhibited low weight loss in an oxidising atmosphere for up to 45 hours (weight loss was only 1.86%) [49]. According to Cao et al. [5] it is also a very promising TBC for SiC substrates because of their similar TECs

2.2.3 Perovskites

Two perovskite powders: $SrZrO_3$ and $BaZrO_3$, are widely considered due to their high melting points and good sintering resistance. However, Vassen et al. [50] found that the former undergoes a phase transformation at ≈730°C, which is subsequently accompanied by an increase in volume and a premature failure of the TBC and the latter has poor thermal stability due to BaO evaporation (due to BaO's high partial pressure) in the hot regions of the coating. However, other studies [51] [52] show that the phase transformations of $SrZrO_3$ produces no significant discontinuities in the unit cell and are almost continuous (with only transformation from orthorhombic to

pseudo-tetragonal producing a small volume change), therefore these are not viewed as a setback for their application as a TBC. One of the above-mentioned studies [51], considers a pure $SrZrO_3$ coating and shows certain promising properties for the material such as the CTE- which is 4.5% greater than YSZ between 200°C and 1200°C, the thermal conductivity- which at 1000°C (2.08 W/(mK)); is lower than 8YSZ, good sintering resistance (less than half of YSZ), low Young's Modulus (170 GPa) and similar fracture toughness to YSZ (1.5 $MPa.m^{1/2}$); however the $SrZrO_3$ fails at only 1514 cycles during thermal cycling indicating a poorer performance compared to YSZ.

More promising results have been obtained using a $SrZrO_3$/YSZ double layered coating; this material withstood 3256 cycles at similar surface temperatures (1231°C - 1251°C) [51]. Additionally, doping $SrZrO_3$ with either Yb_2O_3 or Gd_2O_3 also shows favourable results. The resulting materials $Sr(Zr_{0.9}Yb_{0.1})O_{2.95}$ and $Sr(Zr_{0.8}Gd_{0.2})O_{2.9}$ show a lower and a comparable thermal conductivity to $SrZrO_3$ between 200°C and 1200°C respectively, with the former showing ≈20% decrease compared to YSZ [52]. The same study also noted that the thermal cycling behaviours of a double layered coatings: $Sr(Zr_{0.9}Yb_{0.1})O_{2.95}$/YSZ and $Sr(Zr_{0.8}Gd_{0.2})O_{2.9}$/YSZ had a similar performance to a single layered YSZ at ≈1250°C; here too, $Sr(Zr_{0.9}Yb_{0.1})O_{2.95}$/YSZ has a superior performance compared to a single layer YSZ (at ≈1350°C).

Other studies considered the use hafnate perovskites as TBC materials. One such material was barium hafnate ($BaHfO_3$) which, although displayed a relatively good TEC of 6.93 X 10^{-6} K^{-1} (from 27°C to 1227°C), had a poor thermal conductivity value of 4.44 W/(m*K) at 803°C [53]. Yamanaka et al. [54] looked at two other perovskites- $SrHfO_3$ and $SrRuO_3$ which had average TECs of 1.13 X 10^{-5} K^{-1} and 1.03 X 10^{-5} K^{-1} (27°C to 827°C) respectively; in fact when considering numerous

strontium and barium based perovskites, $SrHfO_3$ had the highest average TEC and melting point [55]. But, like $BaHfO_3$, both the materials had high thermal conductivities which make them unsuitable for TBCs (5.20 W/(m*K) for $SrHfO_3$ and 5.97 W/(m*K) for $SrRuO_3$ at room temperature) [54].

Nevertheless, it is seen that the performance of $SrHfO_3$ can be improved by the addition of Y_2O_3 and Yb_2O_3 dopants too; the resulting coating which has a composition of $Sr(Hf_{0.9}Y_{0.05}Yb_{0.05})O_{2.95}$ has good phase stability, similar CTE (8.60 – 10.39 X 10^{-6} K^{-1} from 200°C to 1300°C), good compatibility with 8YSZ and/or Al_2O_3, and a thermal conductivity of ≈1.92 W/(m*K) at 1000°C- which is around 16% lower than standard a $SrHfO_3$ [56]. Another interesting candidate from the work of Yamanaka et al. [55] and Yamanaka et al. [57] was $BaCeO_3$ which had a thermal conductivity of around 1 W/(m*K), it must be noted that the study also mentions $BaUO_3$ as having similar thermal conductivity values to $BaCeO_3$, however the use of uranium as a TBC element is not recommended for use in the aerospace/automobile sector. The average TEC of $BaCeO_3$ between room temperature to 727°C is reported to be around 1.12 X 10^{-5} K^{-1} [58] which is higher than most perovskites.

Complex perovskites such as $Ba(Mg_{1/3}Ta_{2/3})O_3$ (BMT) and $La(Al_{1/4}Mg_{1/2})O_3$ (LAMT) were investigated by Jarligo et al. [59] wherein, it is seen that LAMT had a lower TEC and thermal conductivity compared to both BMT and YSZ between 0°C and 1200°C. Similar to a previous example, the double-layered coatings (with YSZ) showed superior thermal cycling properties compared to the single-layered complex perovskites and between the two, LAMT showed more promising results than BMT (although this could also relate to the different depositing techniques used for both coatings; Triplex I gun for BMT and Triplex II gun for LAMT) [59]. Double-layered LAMT/YSZ TBC systems could withstand up to 4824 cycles at 1390°C [60].

Although many perovskites are stable at high temperatures, their thermal conductivities are higher than zirconate pyrochlores (discussed in the subsequent section) [33]. Other limitations of using perovskites as TBCs include their lower toughness value compared to YSZ [61] and the partial evaporation of the constituents during deposition (plasma spraying) process [39]. However, it is believed that this difference in vapour pressures could be offset by the use of different evaporation sources [36].

Table 2 gives the thermal conductivities and CTEs of the perovskites considered in this study. It must be noted that only materials whose values are available in the considered literature are listed in the table.

Table 2 Thermal Conductivities and Coefficient of Thermal Expansions of Perovskites (References are in brackets)

Material	**Thermal Conductivity (W/(mK))**	**Coefficient of Thermal Expansion (K^{-1})**
$SrZrO_3$	2.08 [51]	4.5% greater than YSZ [51]
$Sr(Zr_{0.9}Yb_{0.1})O_{2.95}$	≈20% decrease compared to YSZ [52]	Data not available
$BaHfO_3$	4.44 [53]	6.93×10^{-6} [53]
$SrHfO_3$	5.20 [54]	1.13×10^{-5} [54]
$SrRuO_3$	5.97 [54]	1.03×10^{-5} [54]
$Sr(Hf_{0.9}Y_{0.05}Yb_{0.05})O_{2.95}$	≈1.92 [56].	$8.60 - 10.39 \times 10^{-6}$ [56]
$BaCeO_3$	1 [57]	1.12×10^{-5} [58]

2.2.4 **Pyrochlores**

Although Pyrochlores share a similar crystal structure to ZrO_2 (and hence, properties such as low thermal conductivity and high thermal expansion coefficients), they are formed with ordered oxygen vacancies (compared to a more randomised pattern in YSZ) therefore, these materials are expected to show better sintering resistance [62]. It is also seen that the pyrochlore crystals develops only for certain ionic radii of A and B compounds as illustrated in the work of Maloney [63].

Rare earth zirconates ($A_2Zr_2O_7$; where A is a rare-earth element) are among the more promising alternatives to YSZ TBCs. These materials offer encouraging properties like very low thermal conductivity, superior phase stability and good sintering resistance. The thermal conductivity of zirconate pyrochlores are amongst the lowest of any stable pyrochlores with exception of plumbate pyrochlores, however the latter can decompose easily and is not recommended for environmental reasons [33]. According to Vaßen et al. [61], $La_2Zr_2O_7$ (LZ) is a leading candidate for the next generation TBC due to its low conductivity (1.56 W/(m*K)), good stability up to 2000°C and a good sintering resistance compared to YSZ. The thermal conductivity of LZ compared to other zirconates is illustrated in Figure 3. These results are also corroborated by Maloney [63] who states that LZ shows a thermal conductivity reduction of about 50% compared to YSZ at typical TBC operating temperatures and that the former is stable right up to its melting point of 2300°C. The latter study also shows the similarity in the thermal expansion between both compounds. Another advantage of using LZ as a TBC is its higher resistance to oxygen diffusion, which can be put down to its lower ionic conductivity of $9.2 \pm 0.3 \times 10^{-4}\ \Omega^{-1}.cm^{-1}$ (in air at 1000°C) compared to YSZ's conductivity of $0.1\ \Omega^{-1}.cm^{-1}$ (in air at 1000°C) [64].

The thermal cycling tests of LZ showed that the coating had limited

damage/spallation after 1000 cycles at a surface temperature of ~1200°C with a 5 minute heating and 2 minute cooling phase [50][64].The relatively poor thermal cyclic life of LZ coating can be attributed to its low thermal expansion coefficient and poor fracture toughness [64]. Cao et al. [64] discuss certain remedies for LZ's poor thermal cyclic life; their suggestions include:

- Increasing the porosity of the coating to about 15%
- Using graded coatings with YSZ
- Doping additional elements into LZ to increase its thermal expansion coefficient

In terms of mechanical properties, LZ exhibited around a 15% decrease in the Young's modulus and hardness values when compared to YSZ (according to the authors, the low elastic/Young's modulus might help compensate for LZ's low CTE) and its fracture toughness of 1.1 $MPa.m^{1/2}$ is slightly lower than a typical YSZ. [50].

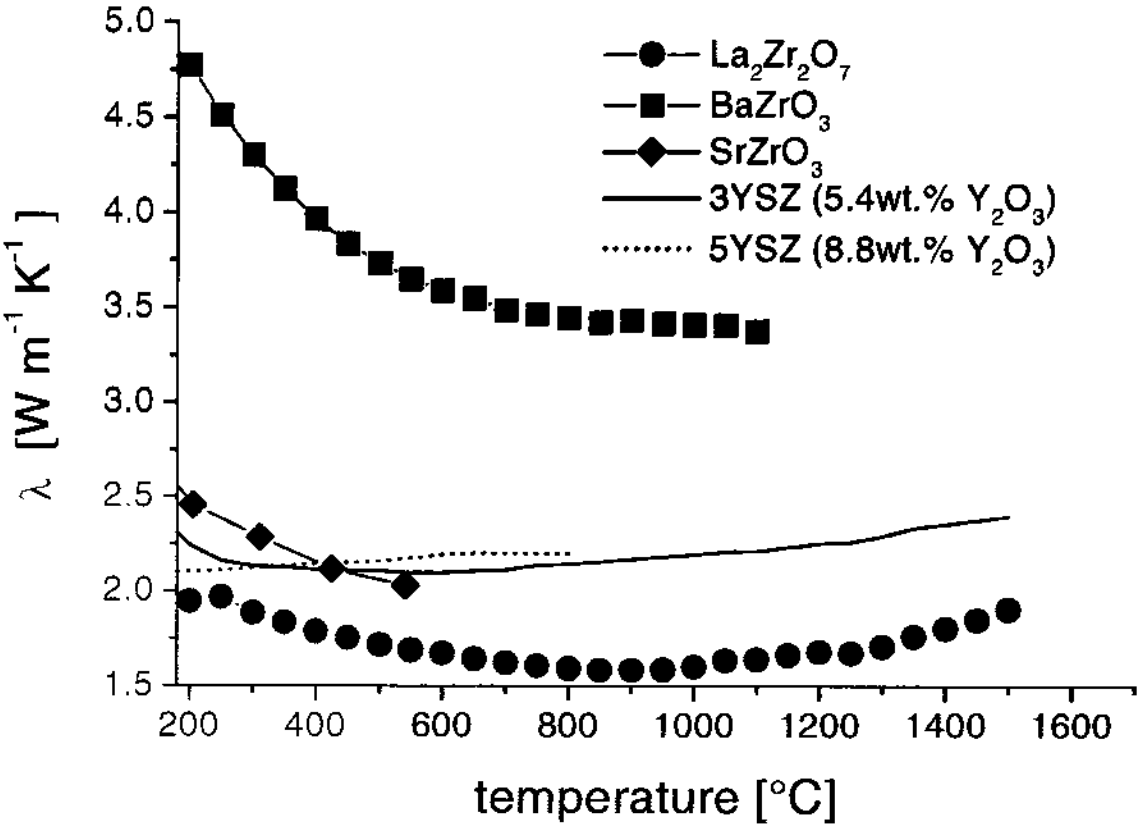

Figure 3 Thermal Conductivities of various Zirconates [50]

When comparing different rare-earth zirconate pyrochlores: LZ, $Nd_2Zr_2O_7$, $Eu_2Zr_2O_7$, $Gd_2Zr_2O_7$, $La_{1.4}Nd_{0.6}$ Zr_2O_7, $La_{1.4}Eu_{0.6}$ Zr_2O_7, $La_{1.4}Gd_{0.6}$ Zr_2O_7 and $La_{1.7}Dy_{0.3}$ Zr_2O_7, it was seen in [65] that the thermal conductivities of all the studied materials were lower than LZ for temperatures less than 1000°C with the partially substituted compounds showing lower thermal conductivities for the entire temperature range i.e., 0°C to 1400°C (for the other coatings the results were inconclusive due to the failure of the opaque graphite coating during the experiment) and the TEC was being higher (for fully substituted materials) or similar (for partially substituted compounds). Additionally, Subramanian [62] gives a list of pyrochlores that are stable up to ~1500°C and are resistant to sintering; one such example (given in their study) is a $Sm_zZr_2O_7$ (33 mole % Sm_2O_3) pyrochlore on top of another layer of 8YSZ which resisted heavy sintering at 1400°C for 500 hours. $Sm_zZr_2O_7$/YSZ also withstood 52

cycles of a thermal shock test at 1250°C and additionally, this material and another TBC coating consisting of $Sm_{2/3}Yb_{1/3}Zr_2O_7$/YSZ showed limited or no signs of a TGO layer after the thermal shock tests [66].

Other similar materials include $La_2Ce_2O_7$ (LC) (having a fluorite structure) which shows a thermal conductivity of ~0.51 W/(m*K) at 1000°C, good phase stability, a TEC of 12.3 X 10^{-6} K^{-1} (between 300°C and 1200°C) and a good thermal cycling life [5] [67]. However in another work [68], the thermal conductivity of LC was reported to be around 1.5 W/(m*K); this work also revealed that near stoichiometric LC coating was stable for up to 240 hours at 1400°C. The difference in the thermal conductivities of LC in both the studies could be either due to the processing route (the former was deposited using EB-PVD and the later was through APS; these are discussed in more detail later on), or a measuring error. Wu et al. [69] calculated the thermal conductivities of zirconate pyrochlores consisting of gadolinium, neodymium and samarium ($Gd_2Zr_2O_7$, $Gd_{2.58}Zr_{1.57}O_7$, $Nd_2Zr_2O_7$ and $Sm_2Zr_2O_7$ respectively) and found that their values are all between 1.5 and 1.6 W/(m*K) at 700°C (which are ~30% lower than 7YSZ). Another important inference from the study is that the thermal conductivities of both the pyrochlore and the fluorite structures (of $Gd_2Zr_2O_7$) show similar values, proving the negligible effect of the ordered pyrochlore structure on the phonon-scattering capabilities of the material.

Since doping improved the thermal conductivities of other TBC materials such as perovskites, its effects in pyrochlores were assessed by Bansal & Zhu [70] who doped pyrochlores with Gd_2O_3 and Yb_2O_3 (($La_{1.7}Gd_{0.3}Zr_2O_7$ and $La_{1.7}Yb_{0.3}Zr_2O_7$) which, resulted in materials with lower thermal conductivities than the undoped material ($La_2Zr_2O_7$); a material co-doped with both Gd and Yb ($La_{1.7}Gd_{0.15}Yb_{0.15}Zr_2O_7$) showed a decrease of almost 30% in thermal conductivity compared to an undoped

oxide. This decrease in thermal conductivity due to Gd and Yb is not dissimilar to the perovskites

For ease of future research work, CTE can also be calculated theoretically for pyrochlores using quasi-harmonic approximation (QHA) and density functional perturbation theory (DFPT). Details of this method are given in [71] wherein, there is a good consensus between the calculated and the experimental values, particularly at lower temperatures.

When considering the existing literature on the layered TBC, it was seen that pyrochlores layered with YSZ or other materials had better properties compared to single layered TBCs. It is seen from the work of Vaßen et al. [72] that $La_2Zr_2O_7$ (LZ)/YSZ double–layered coating (DCL) prepared with in-house powders withstood more than 1200 cycles at 1450°C increasing the maximum temperature by at least 100°C compared to YSZ coatings. The increased thermal cycling performance was also seen in a TBC made up of $La_2Ce_2O_7$/8YSZ; the DCL withstood 5386 cycles at a maximum temperature ~1250°C compared to 1191 and 61 cycles of a single layered 8YSZ coating and $La_2Ce_2O_7$ respectively [73]. However, when both the layers were doped with other elements, the cyclic performance was even better as shown by the work Zhao et al. [74] in which a coating of $La_2(Zr_{0.7}Ce_{0.3})_2O_7$/8YSZ:Eu showed a lifetime of 614 hours compared to 199, 416 and 449 hours for 8YSZ, LZ/8YSZ and LC/8YSZ coatings respectively at 1250°C.

In another study YSZ doped with Yb_2O_3 and Gd_2O_3 was alternated with layers of $Gd_2Zr_2O_7$ (GZO), the thermal conductivity of this TBC was 1.14 W/(m*K) (nanolayer) and 1.10 W/(mK) (thick layer); the values of which increased by ~7% after 20 hours at 1316°C confirming good sintering resistance [47]. Additionally, it was seen from the same study that the nanolayer (average thickness of an individual

layer was ≈200 nm) showed better erosion properties but higher interlayer diffusion rates compared to the thick layered coating with an individual layer thickness of ~30 μm (however, it must be noted that the interdiffusion did not decrease the lifetime of the coating significantly and its lifetime was better than its thicker counterpart). Therefore, it is believed that the size of the individual layer in a multi-layered TBC affects its lifetime performance.

Additionally, Cao et al. [75] studied the different combinations of LZ and $La_2Ce_2O_7$ (LC) from which, a double layered coating (DLC) consisting of $La_2(Zr_{0.7}Ce_{0.3})_2O_7$ (LZ7C3) and $La_2Ce_{3.25}O_{2.95}$ showed the best thermal cycling performance of 225 cycles at a maximum cycle temperature of 1250°C. Xu et al. [76] also considered the life of a LZ7C3/LC coating and showed that it can withstand 654 cycles at a maximum temperature of 1100°C. The authors say that the reason for LC based coatings' relatively poor performance can be explained by 1) LC's incompatibility with the thermally grown oxide (Al_2O_3) resulting in the formation of $LaAlO_3$, 2) sintering of LZ7C3, 3) diffusion of Zr and Ce between the layers and the 4) abnormal oxidation of the bond coat [76].

The cyclic performances of the double layered-pyrochlores are tabulated in Table 3; again, only materials whose values are available are listed in the table.

Table 3 Cyclic Performances of Double Layered-Pyrochlores

Material	**Cyclic Life**
$La_2Zr_2O_7$	1000 cycles at ≈1200°C [50][64]
$La_2Zr_2O_7$/YSZ	1200 cycles at 1450°C [72]
$La_2Ce_2O_7$/8YSZ	5386 cycles at ≈1250°C [73] and 449 hours at 1250°C [74]
$La_2(Zr_{0.7}Ce_{0.3})_2O_7$/8YSZ:Eu	614 hours at 1250°C [74]
$La_2(Zr_{0.7}Ce_{0.3})_2O_7/La_2Ce_{3.25}O_{2.95}$	225 cycles at 1250°C [75]
$La_2(Zr_{0.7}Ce_{0.3})_2O_7/La_2Ce_2O_7$	654 cycles at 1100°C [76]

Another evolution of the layered coatings is the functional graded coatings- where the different layers of the TBC ceramic are gradually changed from one material to another. As shown in Figure 4, TECs of the five materials used are gradually decreased from 10.97 X 10^{-6} K^{-1} for 8YSZ to 10.10 X 10^{-6} K^{-1} for LZ7C3 therefore; a graded structure is very efficient in reducing the TEC mismatch between the different materials, amongst other advantages [77].

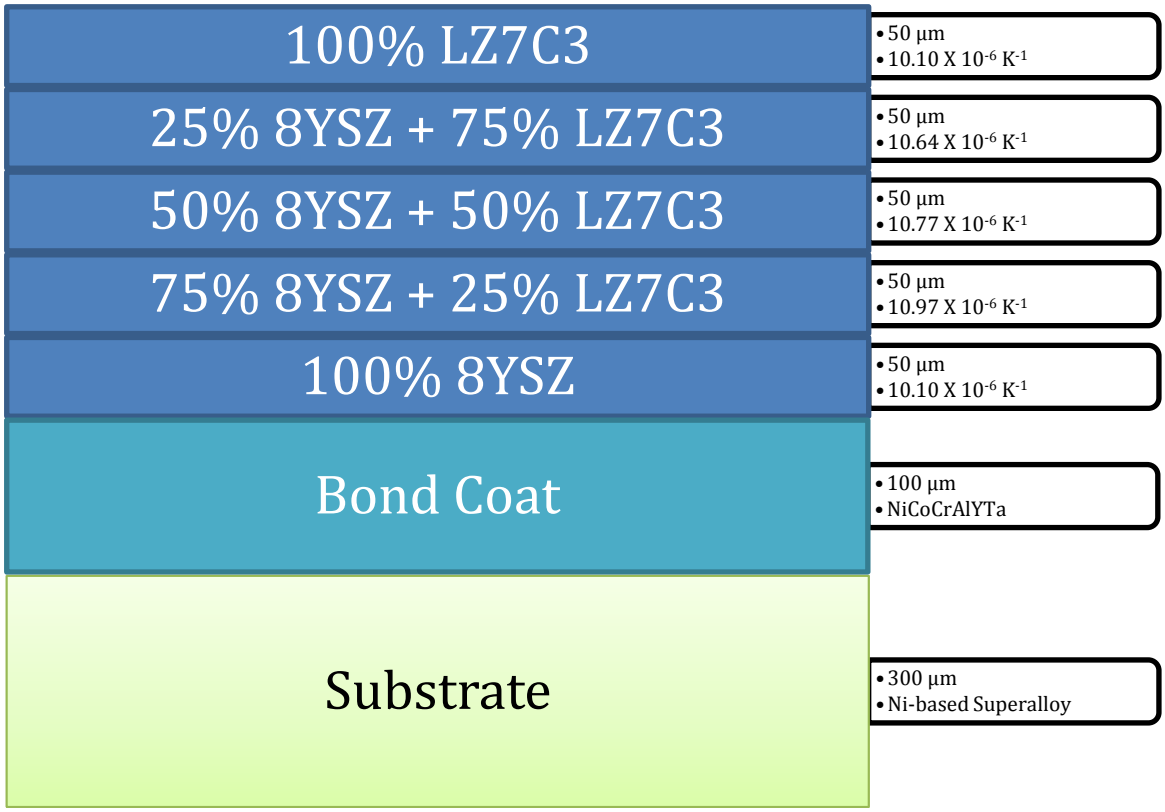

Figure 4 An example of a Functionally Graded TBC. Data taken from [77]

Pyrochlores are relatively easier to process and deposit compared to other TBC materials [61]. Nevertheless, some issues, such as the difference in vapour pressures between the components can result in deviations from the stoichiometric composition. For LZ coatings, the difference in vapour pressures between La_2O_3 (1.0 X 10^5 Pa at 4200°C) and ZrO_2 (1.5 X 10^5 Pa at 4200°C) resulted in a 14% loss of La_2O_3 during deposition [64]. This could negatively affect performance of the coating especially at

high temperatures because the higher rate of formation of $LaAlO_3$ (due to LZ's reaction with the bond coat) coupled with the deposition loss during spraying would culminate with the coating's decomposition [64].

Since, one of the main applications of TBCs is in gas turbine engines, hot corrosion properties of these materials play a significant role in determining the life; Marple et al. [78] studied the performance for both, LZ and YSZ attacked by vanadium (at 1000°C) and sulphur (900°C). Their work shows that LZ was quite resistant to attack by vanadium (V_2O_5) compared to YSZ (which suffered a severe degradation) and that it performed poorly when exposed to sulphur (unlike YSZ, which had minimal change).

2.2.5 **Hexaluminates**

Lanthanate hexaluminates are being considered as potential TBC materials due to their low thermal conductivity, high melting point, high CTE, excellent sintering resistance, low Young's modulus, structural stability up to 1800°C and high fracture toughness [61].

One such material: Lanathanum magnesium hexaluminate ($LaMgAl_{11}O_{19}$) has good stability upto its meting point and a slightly improved thermal conductivity (1.2-2.6 W/(mK)) compared to YSZ, with its CTE being 8.8-10.6 X 10^{-6} K^{-1} [38]. Similarly, properties of other hexaluminates with the general formula $LnMgAl_{11}O_{19}$ (Ln = La, Pr, Nd, Sm, Eu and Gd) where investigated by Haoran et al. [79] wherein it was seen that the thermal conductivity decreases with an increase in the rare-earth ionic radii with the lowest being $GdMgAl_{11}O_{19}$; which had a value between 1.79-2.05 W/(m*K) from room temperature to 1000°C. When considering the CTE, the same paper says that its value increases with the atomic number with $GdMgAl_{11}O_{19}$ showing the

minimum value of 10.63 X 10^{-6} K^{-1} (at 1000°C); the value of CTE for $LaMgAl_{11}O_{19}$ is 10.95 ± 0.03 X 10^{-6} K^{-1} (1000°C) in this study.

Therefore, it is believed that this class of materials do offer a promising alternative to YSZ. However, certain drawbacks such as their ability to recrystallize at elevated temperatures (especially for plasma spray techniques) [61] must be considered prior to their use.

In another work, a DLC comprising of a similar material (to hexaluminates)-lanthanum titanium aluminium oxide and YSZ; $LaTi_2Al_9O_{19}$ (LTA)/YSZ withstood more than 2000 cycles at 1300 ± 50°C, translating to a lifetime of more than 300 hours (compared to a lifetime of 147 hours for YSZ under similar conditions) with the appearance of a spot spallation after 3000 cycles (identical to a holding time of 500 hours)[80]

2.2.6 **Tantalum-Based Coatings**

Tantalum based coatings containing tantalum disilicade, borosilicate glass and molybdenum disilicade (optional) were shown to withstand high heat fluxes up to 1650°C with large thermal gradients [81]. According to the authors, this system results in weights that are 10 to 50 times lighter than the current hot structures used on the leading edges of space/re-entry vehicles. Additionally, Tantalum oxide (Ta_2O_5) was used as an outer layer to protect certain TBCs such as zirconia from adverse environmental effects such as CMAS attacks [82]. Therefore, the use of tantalum based materials for TBCs may open up new possibilities.

2.2.7 **Other Materials**

Materials such as metal-glass composites, nanocrystalline materials/layers have also been considered as potential TBC materials [33][38], although further work is needed to truly establish them as serious candidates. Other potential TBC materials include:

- Garnet ceramics ($Y_3Al_xFe_{5-x}O_{12}$; where x=0,0.7,1.4 and 5)- having low thermal conductivity, very good phase/thermal stability, good high-temperature mechanical properties and low TEC of 9.1 X 10^{-6} /K [5]
- Zircon ($ZrSiO_4$)- showing promising values of thermal conductivity below 1 W/(mK) (Rudajevova in [35]), however a low coefficient of thermal expansion may be crucial limitation for this material and;
- Haffnia with fully stabilised yttria coatings- having excellent phase stability and an increased sintering resistance [33] but a reduction in thermal cycling life with increasing stabilizer content [36]

Additionally, Tryon et al. [83] showed an almost 200%-800% spallation resistance and about 15%-44% oxidation resistance improvement during thermal cycling (up to ~1177°C) for a multi-layered bond coat separately consisting of an oxidation resistance layer and a spallation resistance layer. It must also be noted that certain materials, although promising in theory, face practical/processing difficulties, examples of this include: 1) doped ceria, which although is a promising materials in terms of thermal conductivity, is not suitable due to volatilization [33] and, 2) Lanthanum phosphate ($LaPO_4$) whose small changes in stoichiometry during deposition will change its solidus temperature quite dramatically, hence becoming very difficult to deposit using traditional plasma spray systems [5].

Cao et al. [5] summarise some of the advantages and disadvantages for a few common TBCs; this is given in Table 4.

Table 4 Advantages and Disadvantages of TBCs. Taken from [5]

Materials	Advantages	Disadvantages
7-8 YSZ	(1) high thermal expansion coefficient (2) low thermal conductivity (3) high thermal shock resistance	(1) sintering above 1473 K (2) phase transformation (1443 K) (3) corrosion (4) oxygen-transparent
Mullite	(1) high corrosion-resistance (2) low thermal conductivity (3) good thermal-shock resistance below 1273 K (4) not oxygen-transparent	(1) crystallization (1023-1273 K) (2) very low thermal expansion coefficient
Alumina	(1) high corrosion-resistance (2) high hardness (3) not oxygen-transparent	(1) phase transformation (1273 K) (2) high thermal conductivity (3) very low thermal expansion coefficient
YSZ + CeO2	(1) high thermal expansion coefficient (2) low thermal conductivity (3) high corrosion-resistance (4) less phase transformation between m and t than YSZ (5) high thermal-shock resistance	(1) increased sintering rate (2) CeO2 precipitation (> 1373 K) (3) CeO2-loss during spraying
La2Zr2O7	(1) very high thermal stability (2) low thermal conductivity (3) low sintering (4) not oxygen-transparent	(1) relatively low thermal expansion coefficient
Silicates	(1) Cheap, readily available (2) high corrosion-resistance	(1) decomposition into ZrO2 and SiO2 during thermal spraying (2) very low thermal expansion coefficient

2.3 Processing Techniques for TBCs

Figure 5 summarises the different processing techniques covered in this paper for both, the ceramic top coat and the bond coat. For the ceramic top coat, Plasma Spraying and Electron Beam Physical Vapour Deposition (EB-PVD) are the two most commonly used techniques for deposition. Both these methods give rise to unique microstructure that affects the properties of the TBC system.

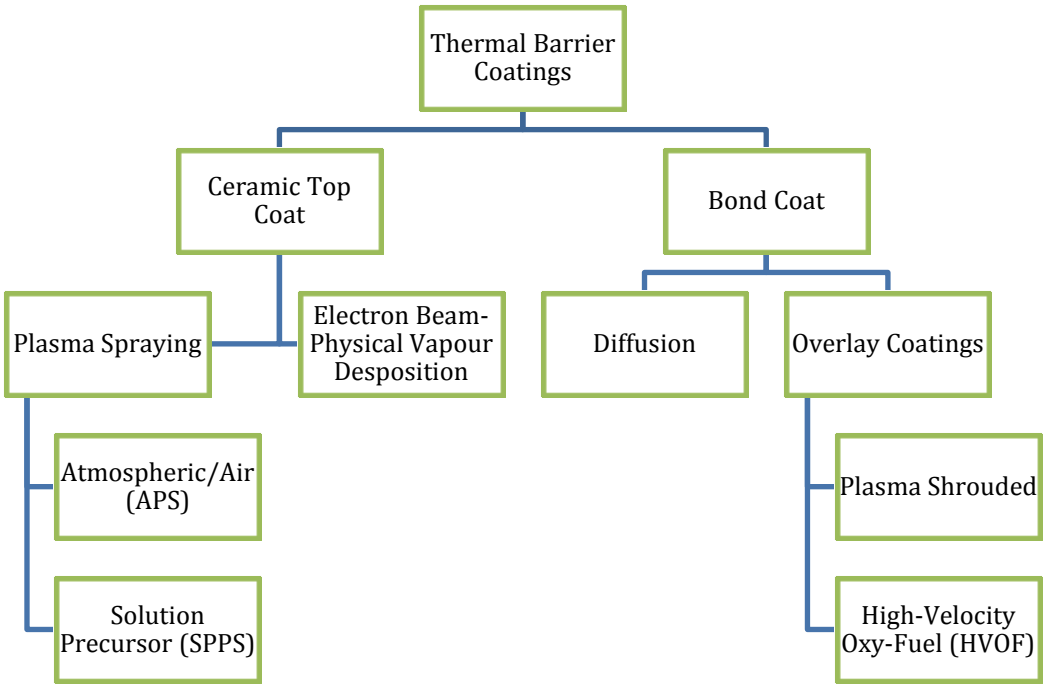

Figure 5 Different Coating Process used in a Typical TBC system

2.3.1 Air/Atmospheric Plasma Spraying

In this process, a plasma gun is used to create a plasma (jet) that melts and deposits the coating material fed using a carrier gas [84]. The main characteristic of the TBCs deposited by the Air/Atmospheric plasma spray (APS) method is the "splat" grain morphologies that are 1-5 μm thick and 200 – 400 μm in diameter, and cracks parallel to the surface of the surface/interface [32]. The orientation of these cracks reduces the thermal conductivity of the top coat; one study showed the value of the thermal conductivity of fully stabilized zirconia drop from 1.6 – 2.0 $Wm^{-1}K^{-1}$ (fully dense

material) to 0.3 – 0.4 $Wm^{-1}K^{-1}$ (plasma sprayed with 6.7% porosity) [85]. The splats are formed due to the impingement and interbonding of the feedstock particles, the subsequent (rapid) cooling and the poor adhesion between various interfaces in the coating creates interlaminar pores between the splats that are critical to the thermal conductivity [86].

The thermal conductivity also increases with aging; above 1100°C, it is seen that the thermal conductivity of normal fully stabilised zirconia is three to five times lower than a similar material aged at 1480°C [85]. Additionally, a plasma sprayed 7YSZ exhibits good strength between room temperature and 980°C (above this temperature the material creeps dramatically and as temperatures crosses 1100°C strength decreases rapidly) and its compressive strength is higher than its tensile strength [84].

It is also to be noted that certain materials tend to oxidise or undergo a phase transformation during the spaying process, such as Ni powder oxidising to form NiO or the transformation of Al_2O_3 from γ to α phase [87]. Hence, the selection of the spray parameters would depend on the coating material.

However, depending upon the powder injection point, Feuerstein et al. [88] say that the plasma sprayed coatings can have two morphologies:

- When the powder is injected externally after the exit nozzle, a "low density" coating with evenly spaced pores and horizontal microcracks between the splat layers is formed. This microstructure shows better thermal conductivity performance.
- If the powder is injected internally within the torch, or externally with more torch power, a denser, vertically segmented coating which has improved strain tolerance but lower thermal conductivity is attained

A further interesting development in plasma sprayed coatings is the use of liquid precursors as feedstock instead of the traditional powder. These Solution Precursor Plasma Sprayed (SPPS) coatings contain microstructural features such as evenly distributed porosity, lack of the large-scale splat boundaries (contributes to an increased strength) and through thickness/vertical cracks (increased strain tolerance) [89][90]. The thermal conductivity of these coatings is around 1.3 $Wm^{-1}K^{-1}$ which is about the same as the traditional plasma sprayed coatings (although another study reported a bond coat temperature reduction of 180°C [39]), but the thermal cycling life of these coatings are superior with the average thermal cycles to failure being between 400 and 500 (compared to between 300-400 cycles for traditional plasma coatings) [90]. A study [60] also showed that the thermal cycling lifetime of SPS coated LAMT was higher than its APS counterpart. To decrease the thermal conductivity of the SPPS coatings even further, a new method, which deposits alternate layers of low and high porosity (Layered-SPPS) has been developed resulting in a thermal conductivity between 0.7 – 0.8 $Wm^{-1}K^{-1}$ [89].

Plasma spraying is the most common method used for thermal barrier coatings due to its versatility and cost. However, the undulating metal/ceramic interface (which are needed for interlocking) produces out-of-plane stresses resulting in failure of the TBC's [32]. Additionally, lower strain tolerances and shorter thermal-cycling lives results in APS TBC's being used in less demanding applications such as combustors, stator vanes, shrouds, fuel vaporizers and afterburner flame holders [32][9]. Therefore, it is believed that future research could unlock more applications for the plasma sprayed TBC, for example, the European 'Toppcoat' project, which according to Mauer and Vaßen [86], shows the possibility of producing plasma sprayed coatings with high strain tolerance that can at least partly replace EB-PVD coatings.

2.3.2 **Electron Beam - Physical Vapour Depositing**

According to Bose [84], Electron Beam-Physical Vapour Deposition (EBPVD) coatings are deposited by creating a melt pool of the coating material using a focused high-energy electron beam; the vapour generated by the pool is then used to coat the substrate (which is held over the pool). The author states that the coating forms due to the deposition of molecules in the vapour, which is different to the deposition of molten particles seen in the plasma spray process. Because of the difference in technique, EB-PVD coatings result in a different microstructure compared to the plasma sprayed coatings. They primarily consist of vertical columnar structures with a thin region of equiaxed grains near the interface (metal or ceramic) and nano-scaled pores within each column [32]. The intra-column pores can be classified under two types [36]:

- Multi-layered, globular and elongated spheroids with orientations that are parallel to their respective column tips
- "Feather armed" pores that occur near on the surface of a column near the centre

Since the thermal conductivity of EB-PVD coatings are higher than their plasma sprayed counterparts (1.8-2.0 $Wm^{-1}K^{-1}$ for a 6-8% partially stabilized zirconia [36]), lowering it will greatly increase the coating's effectiveness. A change in the process parameters will reduce the thermal conductivity of the coating; it is seen that a decrease in the substrate temperature and an increase in the chamber pressure can result in a thermal conductivity reduction of 15% for YSZ coating [91] [92].

Alternatively, modification of the microstructure is also a viable option. The deposition of a "Herringbone" TBC with a Zigzag column structure shows promising results with a thermal conductivity reduction of up to 40% (Beele et al. in [36]). One

drawback with this type of microstructure is its lower erosion resistance and marginally reduced thermal cycling life [93]. Another route to reducing the thermal conductivity of EB-PVD is to take advantage of the smaller columns near the substrate since the increased number of interfaces decreases the thermal conductivity of the material. The technique involves deposition of the TBC in such a way that this microstructure of near the interface is maintained throughout the thickness of the coating. From the work of Schulz et al. [36], it is seen that this can be achieved through:

- Inserting and withdrawing the specimen sequentially and periodically
- Periodically shutting the vapor cloud
- Inserting a contaminant to act as a germination centre for the ceramic layers
- Switching on a strong BIAS voltage within the plasma at regular intervals

Increasing the coating's resistance to sintering can also lower its thermal conductivity wherein; the growth of "club" column structure shows promising results (an additional advantage of this microstructure is its extremely low Young's modulus) [36].

Bose [84] discusses the structural properties of EB-PVD coatings. From his study, it is seen that EB-PVD coatings show a higher compressive strength than plasma-sprayed coatings and because of their different microstructure (explained previously), the elastic deformation of the former is only 10% (same strain rate) of the latter. Finally, unlike plasma sprayed coatings, EB-PVD coatings show a general trend of consistency in both tension and compression. However, the higher cost of EB-PVD coatings limits its application to small components in harsh conditions such as the vanes and blades of aircraft turbine engines [92] [32].

Other interesting depositing process for TBCs include hollow cathode PVD process, thin-film/low-pressure plasma spraying [39].

2.4 Limitations of Conventional TBCs

In addition to the individual drawbacks of different TBC materials, the existing research on TBCs primarily considers a super alloy of nickel (or other similar metals) as the substrate and hence, properties such as the CTE of the coatings are tailored to match the CTE of the substrate. Therefore, current research (as identified in the previous section of this work) is focused in identifying and testing a TBC that has a similar CTE to a nickel super alloy- 11.5 * 10^{-6} K^{-1} between 20°C and 100°C for Inconel [94]. However if other materials such as carbon fibre composites have to be considered, properties such as the CTE (which is -0.4 * 10^{-6} K in the axial direction for a standard modulus PAN-based carbon fibre [20]) would differ substantially from their metallic counterparts; this difference in the CTE and also the poor wettability of the ceramic with a carbon substrate could adversely influence their selection [24][25]. For a successful implementation of TBC's for composite substrates, research has to consider a new class of materials that have a much lower CTE than the existing literature with low thermal conductivity.

Additionally, in epoxy based composites, the resin matrices usually soften, distort and collapse between 60°C and 150°C [95]. Therefore, it is believed that traditional processing techniques like the discussed plasma spraying and Electron Beam – Physical Vapour Deposition (EB-PVD) are not suitable since, the low thermal stability of the organic resins demands processing temperatures less than their glass transition (150°C-200°C) and/or decomposition temperature [96]. Hence, new thermal coating materials and process are required for application onto CFRP substrates.

2.5 Coatings for Carbon fibre composites

Because the current TBC may not be suitable for composite substrates, a study on alternative coating materials and methods was undertaken and presented in the current section.

When comparing intumescent and non-intumescent coatings on Glass-fibre epoxy (with an amine-based hardener) substrates, it was seen that the intumescent coated composites' reverse surface took the longest time to reach 150°C (at 25 kW/m^2 heat flux, the intumescent coating took 203 s and the non-intumescent coatings took 140 s and 125 s), this is mainly due to the consolidated char on the surface that slows down the heat conduction [95]. However, the same study also noted that this time reduced dramatically with an increasing heat flux. From the different types of intumescent coating matrices tested by Bourbigot et al. [97], it was seen that the latex-based (with glass woven fabrics) materials had the best performance in terms of thermal barrier effects. Further, non-intumescent don't rely on char but rather on their ability to trap free radicals during combustion and ending the chain reaction [95]. Use of char forming coatings as a form of thermal protection would require the protection of the char from being blown away, hence they may be unsuitable for certain applications such as the gas turbine and exhaust systems where there is a high air flow.

Although, ceramic coatings such as low melting silicate glass, zirconia (Zr) and aluminium titanate (Al_2TiO_5) coated on glass fibre epoxy laminate provided heat insulation (with Zr and Al_2TiO_5 showing better thermal performance than the silicate glass; the performance is affected by thermal conductivity values and the particle percentage of these powders in the coatings) they were still compromised by the flame retardant epoxy binder (used in the coatings) which ignited at higher heat fluxes (~50 kW/m^2) [98]. Therefore, to counter this, a follow up study using a flame

retardant phenolic resin binder wherein one batch had an additional particle layer on the surface (to reduce the exposure of the binder to direct heat) was conducted; additionally, two new ceramics: nanoclay and nanosilica were also investigated along with the glass flake, Al_2TiO_5 and Zr [96]. According to the authors, the ceramics act as effective thermal barriers even at 50 kW/m^2 with the additional surface layer and the phenolic binder improving the thermal insulation: the Al_2TiO_5 coating with the additional surface later had the lowest heat conduction (partly explained by its high coating thickness) with the back surface taking 89s (35 kW/m^2) and 65 s (50 kW/m^2) to reach 180°C.

Commercially, at least one company- Zircotec [99] offer ceramic coatings on composite substrates. According to a patent filed [100], it is believed that the coating system comprises of an inorganic bond coat consisting of at least one of TiO_2, Al_2O_3, titanate and aluminate and, another layer on top comprising of zirconia, titania and/or alumina. In another patent assigned to the company [101], the use of pockets/gaps of air in the coating layer(s) is used to increase the thermal performance of the coating system; as described in one of its embodiments, a carbon fibre reinforced plastic was coated with an aluminium bond coat which contained air pockets and a magnesium zirconate top coat. In a similar study, zirconia was deposited onto a quartz fibre reinforced polyimide matrix composite with an aluminium interlayer using a traditional plasma spray process [102]. While these coatings showed good bonding at the interface and, increased oxidation resistance and stability; they displayed a dramatic drop in thermal shock performance from 160 cycles at 350°C to 11 cycles at 450°C [102]. According to the authors, this drop in thermal shock performance could be attributed to the efforts of both- increased stress at the interface and the oxidation of the substrate.

Hao et al. [103] considered the use of ultra-short glass fibres (50-70 μm long) in epoxy coatings applied on a mild steel substrate because these fibres could be dispersed more easily in the coatings. According to the authors, the amount of glass fibres does have an effect on the final properties of the coating with epoxy containing 20% (volume fraction) glass fibres showing the best barrier effect; it was also seen that the increasing content of glass fibres (from 0 to 30%) decrease the TEC value (from 178.6 * 10^{-6} C^{-1} to 81.5 * 10^{-6} C^{-1}) and increase the glass transition temperature from 45°C for an epoxy with no glass fibres to ~50°C for coating containing 10, 20 and 30 % glass fibres. However it must be remembered the results were obtained from tests on a steel substrate and a different substrate would result in a variation of certain properties such as adhesion, thermal stresses, etc.

Other studies also considered the use of hollow glass microsphere (HGM) as a potential filler material. Vahtrus et al. [104] observed a decrease in thermal conductivity with the addition of HGM in an epoxy matrix. In another study, Yung et al. [105] state that the addition of these materials (HGM) in a brominated epoxy matrix managed to decrease the latter's CTE, thermal conductivity dielectric constant and dielectric loss by 54.3%, 13.3%, 28.6% and 44% respectively. Zhu et al. [106] also observed similar trends with their HGM/epoxy composites showing a maximum decrease of 56%, 51% and 54% for thermal conductivity, dielectric constant and loss respectively. They also concluded that the voids in the epoxy have an effect on the thermal conductivity of the final material. Similarly, the review by Rahaman et al. [107] also showed a decrease in dielectric constant and dissipation factor values with increasing HGM content as reported by the different studies in their work. However, their paper does not comment on any thermal properties instead, considering the

mechanical responses of these composites including the addition of nanoreinforcements.

The application of ultra-high temperature ceramics (UHTCs) such as borides and carbides of hafnia and zirconia for TBCs are also considered. CTEs of monolithic ZrB_2 and HfB_2 are 7.83 * 10^{-6} K^{-1} and 7.63 * 10^{-6} K^{-1}, respectively (which are lower than most materials considered here). HfB_2 based ceramics retaining their structure up to 15.2 MW/m^2 of heat flux [108] thereby showing their potential as a TBC. However, the very high intrinsic thermal conductivity (approaching copper at room temperature) [109] excludes their use in the top layer of the TBC. Nevertheless, it is believed that these materials might find use in the bond coat or one of the intermediate layers of the coating system. The carbides of hafnium or zirconium have a high elastic modulus [109] but both compounds oxidise at 400°C and 380°C respectively [110] which would change their compositions to HfO_2 and ZrO_2. According to Xie et al. [111] ZrO_2 strongly adheres to a C/C-ZrC-SiC composite thereby serving as a barrier to thermal and oxygen diffusion. But, the ZrO_2 in this study is molten and further work is needed on a solid phase zirconia and also, hafnia to establish the suitability of these carbides as a TBC for carbon composites.

Finally, the use of aerogels as a filler material is also a promising route for future thermal coatings. According to Koebel et al. [112], aerogels can be classified under the rare category of superinsulating materials along with vacuum insulation panels and vacuum glazing. However, vacuum insulation systems are very sensitive to gas permeability which would decrease their thermal performance in the long run [112]. Therefore, interest in aerogels has steadily grown over the last decade or so as evidenced by the number of scientific publications on the subject which, have increased from 335 (in 2005) to 1092 (in 2015) [113]. This has also been supported by

an annual market growth rate between 50-75 %, touting aerogels as the insulation material of the future [112]. Additionally, because of its superinsulating properties, aerogels also offer great potential for sustainable development [112].

2.6 Aerogels

Aerogels are materials with a gelatinous structure in which the liquid is replaced by a gas with minimal shrinkage [114]. This results in an open celled mesoporous structure producing an ultra-lightweight material [115] having low thermal conductivity (0.012 W/(m*K)), density (0.003-0.35 g/cm^3), dielectric constant (1.1-2.2), thermal expansion coefficient (2-4 *10^{-6}) and refractive index (1-1.08) along with a high specific surface area (500-1200 m^2/g) and porosity (>90%) [116][117][118][119]. The extremely low thermal conductivity of these materials is due to a combination of small pores and low density [112].

The different steps involved in the production of aerogel through the sol-gel route include gel preparation, gel aging and drying; these steps are further detailed in [112][120][121]. According to Du et al. [122], aerogels can be classified according to their method of preparation, microstructure, composition and appearance (as shown in Figure 6). Therefore, because of the properties identified, these materials find application in various industries such as thermal insulation for transport vehicles, pipes, cryogenics, portable coolers, space vehicles, casting moulds and building applications [112][123][121][124]. They also show promising application in specialised garments such as firefighter's protective clothing when combined with an organic phase change material (Eicosane) [125] and, in biomedicine such as drug delivery systems and regenerative medicine [113]. However, widespread use of aerogels has been limited because of their fragility, demand for supercritical drying, hydrophilicity and high production costs [120][126][127].

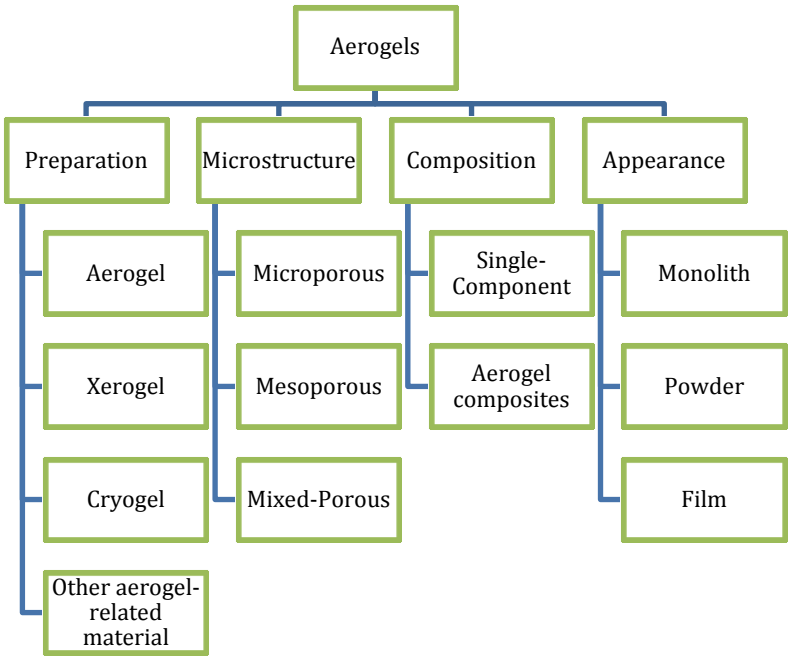

Figure 6 Classification of Aerogel. Data taken from [122]

To increase the aerogel's strength, combination of the aerogel with a polymer thereby taking advantage of the mechanical strength of the latter with the thermal stability of the former is suggested [126][127]. The process proposed by Schmidt & Schwertfeger [128] wherein, the polymers are used as the binding material (matrix) is thought to be promising due to its simplicity. According to the study, the binding systems can be divided into dry (such as thermoplastic polymers) and wet (such as thermoset polymers) systems.

2.6.1 **Thermoplastic Systems**

When considering thermoplastic binding matrices, Mielke and Dungen [129] mixed and moulded various combinations of aerogel with a binder containing an aqueous suspension of magnesium montmorillonite and a thermoplastic styrene/butyl acrylate aqueous polymer emulsion. The authors reported that, in all the cases the thermal conductivity of the composite did not exceed 0.020 W/(m K). Vo et al [130] reported a decrease in the thermal conductivity of an extruded thermoplastic foam when

cavities filled with aerogel were introduced in the parent material. According to their work, the thermal conductivity of the extruded thermoplastic foam dropped from 45 mW/(m K) to 30 mW/(m K) for cavities with 9 mm aerogel and to 27 mW/(m K) for cavities with 18 mm aerogel.

In another study, Schmidt and Schwertfeger [128] showed that the addition of aerogel to a polyvinylbutyrale (PVB) matrix results in a decrease in the thermal conductivity of the material wherein the addition of around 90 % (volume fraction) of aerogel resulted in a thermal conductivity close to 25 mW/(m K) (compared to 120 mW/(m K) for PVB). Kim and Hyun [118] also measured the thermal conductivity of Aerogel/PVB composites and discovered that the thermal conductivity decreased significantly when the volume fraction of the aerogel went above 70%. However, the authors noted that dry mixing of these two materials was challenging due to the differences in their materials densities. Although the work also considered wet mixing and dual mixing methods to ensure uniformity, the resultant composites had higher thermal conductivity (for the former) and lower modulus of rupture (for both). Williams et al [131] considered MXD6 polyamide in their work and showed that the thermal conductivity of the aerogel/polyamide composite was around 40% lower than a neat MXD6 sample ; however, they also report a breakage of the aerogel particles inside the twin screw extruder which could affect the thermal performance of the material.

2.6.2 **Thermoset system**

When considering thermoset binders, Basri et al. [132] obtained good water absorption test results for silica aerogel/epoxy nanocomposites by reducing the stirring speed and increasing the stirring time when mixing the aerogel with the pure

resin and, by increasing the stirring speed and shortening the time when mixing the previous mixture with a hardener.

According to Zhao et al. [133], aerogel/epoxy composites have thermal conductivities as low as 0.105-0.175 W/(m*K) and the relationship between the property and the weight fraction of the aerogel is not linear. Additionally, their study also showed that bigger aerogel particles (0.2-2 mm) provided better thermal properties than smaller particles (<0.2 mm). In another work, Gupta and Ricci [115] demonstrated better mixing of the aerogel particles by reducing the viscosity of the resin using higher temperatures. Nevertheless the authors of both research ([133] and [115]) comment on the possible infiltration of the resin into the pores of the aerogel. This effect was further noted in the work by Vahtrus et al. [104] wherein the authors observed an increase in the thermal conductivity of aerogel/epoxy composites due to the filling of the resin into the pores of the aerogel. Achar & Procopio [134] also showed that aerogel had a higher values of thermal conductivity compared to glass microspheres (in acrylic polymers) which according to the authors, could be due to the polymer intrusion into the pores of the aerogel. The infiltration of the epoxy resin in the pores of the aerogel is also discussed in [135].

Kim et al [136], however, demonstrated lower thermal conductivity values for samples manufactured using ethanol evaporation to preserve the pores; these samples showed better thermal performance when compared to as-received and plasma treated aerogels across different volume fractions. In another work, Maghsoudi & Motahari [137] characterised the thermal, physical and hydrophobic properties of aerogel/epoxy composites and showed that the thermal conductivity of the composite samples reduced as the mass fraction of the aerogel increased; the lowest value reported in the study was 0.074 W/(m*K) for 3% aerogel (compared to 0.195 W/m*K for the pure

resin sample). Further, Ge et al. [138] incorporated the aerogel into a solid epoxy powder, thereby limiting the resin infiltration.

Finally, although the true thermal conductivity of the composites can only be determined experimentally, models such as the core-shell based formulation illustrated by Kiil [139] to determine the thermal conductivity of such composites, would enable a realistic simulation of the material's performance and potentially accelerate further research in the area.

Additionally, epoxy based systems mixed with glass micro balloons have also been used as a base coat/primer for carbon fibre reinforced epoxy substrates resulting in an improved thermal protection [140]. Similarly, the same study also reports uses of epoxy-based coating as a primer/base coat for other aerospace applications involving composites [140].

2.6.2.1 Cure Kinetics

The study of cure kinetics and the relationship between the degree of cure and the properties are essential parameters needed to identify optimum cure conditions [141] [142]. When considering the cure kinetics of epoxy resins, Gonis et al. [143] noted that the amount of heat released during cure was indirectly proportional to the number of ethylene oxide units in the epoxy resin. Roşu et al. [144] calculated the activation energy of two different epoxy resins, diglycidyl ether of bisphenol A (DGEBA) and diglycidyl ether of hydroquinone (DGEHQ) using the isoconversional method and found the activation energy remains independent of the working conditions and almost constant between conversion intervals of 0.3 and 0.6. The curing of epoxy resins is a complex multistep process that could include numerous chemical reactions or a reaction that could have complex effects like vitrification and viscous relaxation [145]. These effects, according to Yoo et al. [146], play a role in decreasing the

activation energy towards the end of the cure. The work of El-Taher et al. [147] compared the activation energies and frequency factors for DGEBA resins cured with hydrolysed materials from salt solution and curing agents without salt and found the values for the former to be higher than the latter. However, the activation energies calculated for the curing agent without the salt solution was similar for the three methods used in the paper (Kissinger, isoconversional and autocatalytic methods) but varied when the material from the salt solution was used.

Montserrat and Malek [142] compared the results of non-isothermal and isothermal data and stated that both methods produce similar results when the curing is primarily controlled by the chemical reaction. However at lower temperature, the authors argue that the problem is more challenging due to effects such as vitrification. When considering the different non-isothermal methods, Hong and Lee [148] calculated the activation energy of silicone rubber using the Kissinger, Ozawa, Flynn-Wall-Ozawa and Friedman methods wherein the methods showed similar results with Friedman method having the lowest value. El-Thaher et al. [147], state that the Kissinger method is more accurate than the Ozawa method for n^{th} order reactions.

2.7 Thermal modelling of composites using finite element methods

Zhai et al. [149] detail several different theoretical and simulation models used to determine the effective thermal conductivity of particle filled composites. According to the authors, finite element method (FEM) is an effective numerical simulation technique and one of the more well-known methods used to model composites at macroscopic scales. Therefore, since the present work considers simulations at this scale, FEM was chosen as the methodology to be used subsequently.

FEM was used by Bakker [150] to calculate the 2D thermal conductivity of a matrix with a dispersed phase which was then subsequently converted into its 3D counterpart

using an equation. The work states that the determined 2D value acts as a useful lower limit of the actual thermal conductivity of the material and takes into account the orientation, distribution and the shape of the dispersed particles. In another study [151], three different modelling techniques- finite element, Mori-Tanaka and strong contrast were compared for two-phase random composites and shown that results were close to each other for spherical inclusions. However, there was some difference in the results for particulates with different aspect ratio. The work also showed that a higher level of reinforcement in both, elastic modulus and thermal conductivity can be achieved through the use of platelet fillers. Nevertheless, the present work recognises that a choice in shape of the fillers may not always be possible or viable. In another study, Tsekmes et al. [152] developed a FE model to simulate the heat transfer through a polymer composite by considering the effect of particle shape, size, interconnectivity, agglomerations and interfaces. The authors managed to obtain a good fit with the experimental data for the three types (Al_2O_3, MgO and SiO_2) of epoxy composites simulated by assuming an interfacial layer or the first two and without the said layer for the unmodified silica particles.

The heat transfer behaviour of powder silica hollow spheres were simulated by Liao et al. [153] and compared with experimental and calculated data. Their study shows the influence of the internal diameter and density (of the spheres) on its thermal conductivity value. Although the thermal conductivity results from their FE model had the highest value amongst the calculated and experimental data; it still showed the possibility of using this technique to model the heat transfer process through the spheres. Liang and Li [154] simulated the heat transfer through a polypropylene/hollow-glass-bead composite using finite element methods (FEM) and show that the effective thermal conductivity calculated using the model is close to the

experimental data with its value decreasing with an increase in the diameter of the beads.

Both studies ([153]&[154]) comment on the nature of heat transfer by stating that the majority of the heat flows along the particle walls with a small part going through the sphere and an even smaller amount through its walls. Hence, because the route along the wall is longer and more complicated, heat transfer properties of the composites are reduced. Finally, Vahtrus et al. [104] also used FEM and obtained a good fit with the experimental values for HGM/epoxy composites. Their results also show the superb insulating potential of aerogel/epoxy composites under ideal scenarios (for example when matrix infiltration is not considered).

2.8 Gap in Literature

The literature surrounding conventional TBC's is primarily focused towards a superalloy substrate and hence, there is a possibility of property mismatch like CTE difference (as identified in section 2.4) which would decrease the performance of said materials on a CFRP substrate. However it is believed that for static thermal loadings these differences could be negligible and hence exploratory studies on these coatings, particularly YSZ, could be worthwhile.

As discussed in section 2.5, there is at least one product offered by Zircotec [99] available commercially; however it is believed that these systems use an intermediate bond coat [100][102] to help achieve their objectives. According to [101], the use of a bonding material with a lower melting point than the thermal (top layer) would allow the coating of the latter without destruction and damage to the organic substrate. But the addition of another layer would only increase the number of interfaces and thereby, the thermal stresses which, is thought would decrease the long term

performance of the material, particularly under thermal cyclic loads as demonstrated by the dramatic drop in thermal shock performance for the materials in [102].

Therefore, research into the possibility of applying YSZ (or other similar thermal barrier ceramics) directly onto the substrate using lower processing temperatures is suggested since this would simplify the process by removing the need for a middle layer(s). Additionally, the direct coating method using low processing temperatures could also offer a more economical, accessible and potentially safer alternative to plasma sprayed coatings. Therefore, information on low temperature coating systems/techniques for these materials would be invaluable. Further, to justify its progress from a laboratory model to an industrial scale production, these coatings would also have to be characterised and compared with their high temperature counterparts and, other competitive coatings.

In addition to YSZ the existing research on aerogels is a promising direction for thermal insulation materials and coatings. Although, some of the initial drawbacks of using this fragile material can be overcome by using a polymer binder, further research on these materials is required. It must be noted that the use of polymer binders to strengthen aerogel-based materials is in itself not a novel idea as shown by the studies discussed in sections 2.6.1 and 2.6.2. However, further research on specific aspects (as discussed subsequently) is needed for more effective application. One particular area of interest is the long-term fatigue and/or aging performance of these coatings; although multiple studies report on properties such as the thermal conductivity of these coatings, data linking these values to prolonged/accelerated exposure to actual service environments would allow for a more comprehensive understanding.

When considering the literature on thermoplastic binders, one of the limitations, as noted by Kim and Hyun [118], could be the difference in densities between the material which, may result in an inhomogeneous dry mix. It is believed that the use of a twin-screw extruder may counter this drawback. These types of extruders have, amongst other advantages, good mixing abilities, heat transfer, melting and control over a range of temperatures [155]. Additionally, it would be ideal for medium-to-large scale manufacturing as extrusion is a continuous process. But Williams et al [131] showed that the extrusion process described in their study damaged the aerogel structure. However the patent utilised extrusion speeds of around 50 rpm for the polyamide binders. Therefore, it is thought that less harsh processing conditions by using lower extrusion speeds may offer further protection to the aerogel particles in the composite. To provide evidence for this claim, characterisation and experimental data between samples extruded at different speeds is needed to compare and contrast the properties and performance.

From the reviewed literature, the impregnation of aerogel particles in a thermoset resin such as epoxy was seen as another route worth exploring. Apart from it being incorporated in the substrate, the widespread use of a liquid epoxy resin system in composite materials, adhesives and moulding compounds [156][141][157] would offer, amongst others, increased economic advantages in commercial use. However resin infiltration into the aerogel pores should still be considered and limited; one way of limiting liquid resin infiltration is through the usage of solvents like ethanol [136] which are highly flammable and potentially explosive [158][159]. Also, incorporation of aerogel by decreasing the viscosity of the resin through higher temperatures has also been studied in [137] and [115] to improve the mixing. But it is believed that a more viscous resin would further decrease resin infiltration into the aerogel pores

compared to its less viscous counterpart and hence, research into using this phenomenon should be undertaken. Additionally, successful application of this technique could potentially reduce the requirement for other auxiliary/more-hazardous methods/material. Once again, research has to be undertaken in successfully producing such a method and experimentally generating data for characterising the resultant material.

Finally although there are multiple research undertakings on the production of aerogel/polymer composites, very few (if any) have considered these materials as coatings and their subsequent effect on the thermal degradation of the substrates. This would be an interesting venture and may require further iterations on the production and/or application techniques

2.9 Aim and Objectives

From the review of different materials (such as YSZ, HGM and ceramic based coatings) carried out in the previous sections, it is believed that the use of aerogel based composites would offer the most promise as thermal insulation coatings for carbon fibre composites.

Therefore, the aim of this research is to **create, characterise and model** an efficient **thermal insulation** coating based on **aerogel/polymer composites** for carbon fibre reinforced plastic substrates that could also be adopted or **large scale production**.

Keeping this mind, the objectives of the present work include:

- The identification of **suitable thermal coatings** for carbon composites
- The development of **optimal processing conditions** for the incorporation of aerogel in polymers
- The characterisation and quantification of the **aerogel/polymer properties and performance** through experiments

- The utilisation of data from the experiments to **design and build a finite element model** that predicts the coating's performance under different thermal loadings

In order to satisfy the third objective, the study will also look to determine the long-term performance of the coating through aging and fatigue tests.

3 Methodology

The following chapter details the different materials, methods, experimental and modelling methodologies used in the present work. A general flow of work through the different materials and coatings in the present work is shown chronologically in Figure 7.

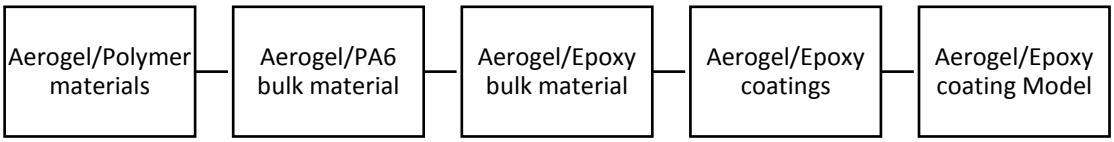

Figure 7 Flow of work

3.1 Materials and Methods

This section discusses the various materials and experimental apparatus used to process and characterize the composites in the present study. Initially, the processing parameters for the insulation bulk materials and coatings are described, followed by the experimental techniques.

3.1.1 Materials

3.1.1.1 Aerogel/Nylon 6

Aerogel particles were chosen as potential insulators due to the material's low thermal conductivity and density values (section 2.6). In the present study, Cabot Enova Aerogel IC3110 (particle size 100-700 μm) and Lanxess Durethan B30 polyamide 6 (PA-6) were used as base materials for the samples. Two different collections of such particles imaged under a scanning electron microscope and an optical microscope are shown in Figure 8 and Figure 9 respectively; the details of the instruments used are discussed subsequently in section 3.2.1.

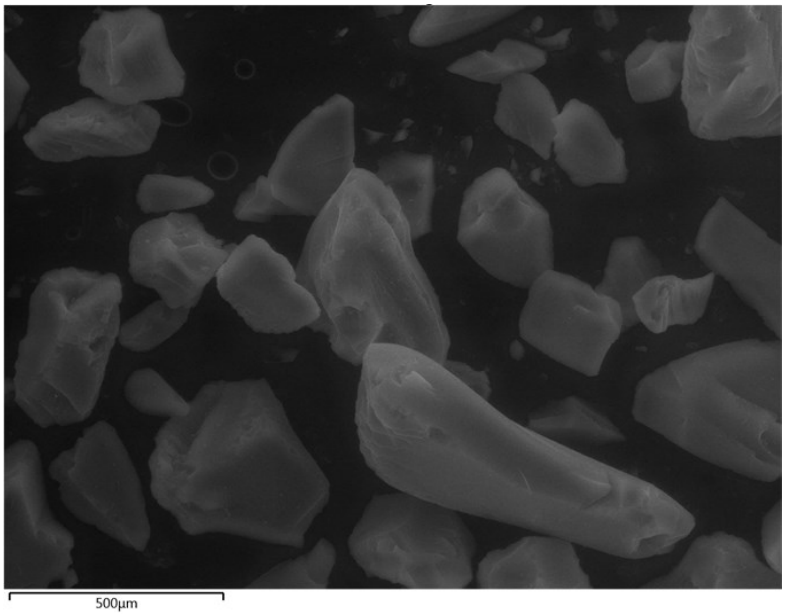

Figure 8 Scanning electron microscope image of aerogel particles used in the present study. The particles were imaged after sprinkling the aerogel onto a carbon adhesive disc

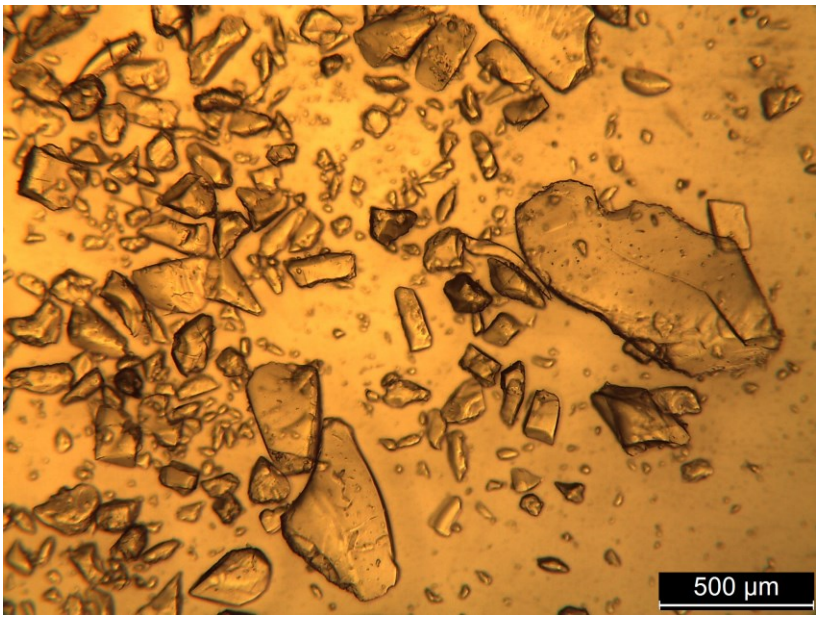

Figure 9 An optical of image of aerogel particles at 5X magnification. For this image, the aerogel was sprinkled onto a glass slide prior to imaging

The Nylon was initially heated in an oven to 80^{0}C for 180 minutes to remove moisture. Next, in order to prepare the composites, 0.04 mass fraction of aerogel was manually added and mixed into each batch of PA-6 before extrusion and poured into

the feeder as one material. Three different batches were extruded and compression pressed into plaques. The details of the three batches are:

- Pure PA-6; run through the extruder twice at 65 rpm (Sample A)
- PA-6 with 0.04 (mass fraction) aerogel; run through the extruder twice at 65 rpm (Sample B)
- PA-6 with 0.04 (mass fraction) aerogel; run through the extruder once at 5 rpm (Sample C)

A Rondol Twin Screw extruder with the processing temperatures as set in Table 5 was used to extrude the composite which, was then cut into smaller pieces using a pelletizer.

Table 5 Extrusion Parameters

Zone 1	Zone 2	Zone 3	Zone 4	Die
225°C	230°C	235°C	230°C	225°C

The extruded material (samples A, B and C) was heated to 110°C for 270 mins to remove any moisture. Then, each individual sample was poured into a mould that was then placed inside a preheated compression press (230°C). Initially, both the moulding plates were brought into contact with the mould containing the sample material to facilitate heat conduction into the sample for 11 mins. After this, the pressure was increased to 2.76 MPa for a further 5 mins. The sample was allowed to cool inside the press for 65 mins (maintaining a pressure of 2.76 MPa). Finally, the mould was removed from the press and left to cool to room temperature outside. For samples B and C, the hold time was increased from 11 mins to 13 mins to account for the insulating presence of the silica aerogel.

3.1.1.2 Aerogel/Epoxy

The preparation of aerogel/epoxy was divided into three steps. The first part was to determine an optimum mass fraction of the former to be added into the resin. Subsequently, the cure kinetics of the resin and the composite was studied to ascertain any effect on the cure kinetics and finally, the ideal time to introduce the aerogel into the matrix system was identified.

Once again, Cabot Enova Aerogel IC3110 was used as the aerogel. RS-M135 by PRF composites was used as the epoxy resin for the matrix and the hardener was a custom blend of RS-MH137 and RS-MH134 in a 2:1 ratio. This particular system was chosen due to its low viscosity; according to the product data sheet [160], the viscosity of the resin at 25^0C is ~2650 mPa s (cps) and its mixed viscosity is between 500-1000 mPa s (cps). The reason for selecting a low viscosity system was to increase the wettability of the aerogel with the resin and to improve the mixing of the aerogel. Gupta and Ricci [115], in their study, showed the engulfment of the aerogel particles by reducing the viscosity of the system. A low viscosity system also has the advantage of moulding into complex geometries and a more homogenous distribution of the matrix. However, as discussed previously, one potential drawback of using a low viscosity system is the infiltration of the resin into the aerogel pores, which could negatively affect the performance of the material. Therefore, the requirement for a balance between mouldabilty/engulfment and resin infiltration is used as the primary driver for the methodology adopted.

To prepare the samples for identification of the ideal mass fraction of aerogel, the resin was heated to 40^0C and an appropriate mass fraction of the aerogel was stirred into the resin. The material was left for 5 mins to stabilise. After which it was degassed using a vacuum pump for 15 mins to remove the air from the material. The

solution was reheated to 40^{0}C and the hardener was added; the resin to hardener ratio used was 10:3. The material was degassed again for 15 mins and poured into a glass mould. Finally, the samples were cured at 60^{0}C for 18 hrs. The reason for using an elevated curing temperature was to decrease the gel time of the resin.

The samples produced contained 0.01, 0.02 and 0.03 mass fraction of aerogel. Additionally, a batch of pure epoxy (with hardener) was also produced as a control. For the control samples, both of the resin and the hardener were mixed in a pot at around 40^{0}C, degassed and allowed to cure in the glass moulds at room temperature. These samples were then post cured at 64^{0}C for 4.5 hours to achieve uniformity in their properties. Different curing cycles between the aerogel/epoxy and the control samples were believed to be justified because the aim was to study the resin infiltration into the aerogel. Therefore, the requirement was to attain a solid sample and although further curing may have been required to attain the best mechanical properties, it is thought that this would have a negligible effect on the infiltration of the resin. All the samples were then cut to the required dimensions using a mechanical saw. The pure epoxy samples are labelled P followed by the sample number. The composites have the mass fraction of the aerogel prefixed to P; therefore materials containing 0.01 mass fraction of aerogel are called 1P, materials containing 0.02 mass fraction of aerogel are referred to as 2P and samples with 0.03 aerogel mass fraction are named 3P.

Next, the cure kinetics of the aerogel/epoxy composites was measured. Here, a wetting agent- BYK-P 9920 (BYK-Chemie, Germany) as recommended by the company was used to prepare one of the batches to increase the aforementioned engulfment between the resin and the aerogel. The first batch of these samples was made from pure epoxy resin and hardener wherein the resin and the hardener were

mixed in the required ratio and then tested. For the second batch, the resin and the hardener were mixed together as previously discussed and then 0.03 (mass fraction) of aerogel was added, mixed and the samples tested. Finally, to prepare the third batch, after the resin was weighed, 3% (by weight) wetting agent was added to the solution. The hardener was then introduced and the solution was mixed together before 0.03 (mass fraction) of aerogel was added and the samples tested. It must be noted that the mixing for all the samples were carried out manually.

Finally, the addition of aerogel at the right time of cure to achieve the balance between infiltration and mouldability was considered and the samples manufactured accordingly. The samples for morphological and spectrophotometry analysis were made by mixing the resin and the hardener using the given ratios (10:3) and then degassing the mixture in a vacuum oven at room temperature for 10 mins. The contents were then removed and stored in closed containers. When the sample was ready for analysis, 0.03 mass fraction of aerogel was added into the resin and stirred before being placed inside the apparatus. The times of addition and hence, the analysis were 0.5, 1 and 1.5 hours after the hardener was mixed in. Hence, each batch was further divided into 3 samples depending on the time of aerogel addition- 0.5, 1, 1.5 (reflecting the time of addition).

Batch A was used as a control and was made using the resin and the hardener only. Batch B was a composite of the resin, hardener and the aerogel particles. Batch C was similar to batch B with the exception of a wetting agent which was added into the resin before the hardener. As recommended by the company, 3% (of the total weight of the solution) of BYK-P 9920 (BYK-Chemie, Germany) was stirred in as the wetting agent. A summary of the batches and samples used in the present study is shown in Table 6.

Table 6 Batches and samples used in the present study

Batch	Sample
A (Pure resin)	0.5A
	1A
	1.5A
B (Resin + Aerogel)	0.5B
	1B
	1.5B
C (Resin + Wetting agent + Aerogel)	0.5C
	1C
	1.5C

For spectrophotometry and morphological analysis, a solution containing 10g of deionised water and 0.05g of methylene blue powder (C.I. 52015) supplied by Merck (Germany) was mixed and a few drops of the solution was added into each of the spectrophotometry (and microscope) samples during its processing to colour it. Once the materials were prepared, they were then manually spread onto a glass slide prior to the analysis. After the spectrophotometry test runs, the samples in the glass slide were left to fully cure (minimum of 5 days) at room temperature before being observed under the microscopes.

For the samples used for thermal conductivity testing, the resin was left inside the vacuum oven for the whole duration i.e., 1 hour, before the addition of aerogel. After which, they were transferred to a glass mould and allowed to cure. The pure resin sample was cured at 60^0C for 24 hours and the composite sample- 1C was cured at room temperature for 48 hours. Once cured, the required sample sizes (30*30*4 (mm)) were cut from all the batches and tested. The aerogel-epoxy sample was cured

at room temperature because a higher cure temperature would decrease the viscosity of the resin and hence, increase its rate of infiltration into the aerogel.

Once an effective process for production was identified, the aerogel epoxy samples were also coated on a carbon fibre reinforced plastic (CFRP) plate (discussed in the subsequent section). The first batch was a plain resin coating without the aerogel particles wherein the resin and hardener were mixed in the ratio described previously and the mixture was degassed in a vacuum oven for around 30 mins. After degassing, the CFRP substrates were dipped into the resin to form a coating around it (dip coating) and the new coated composite was left to cure at room temperature for a minimum of 48 hours.

The aerogel/epoxy coating (second batch) contained 3% (of the total weight of the coating) wetting agent which was stirred into the resin before the addition of the hardener and the resulting solution was degassed in a vacuum for 1 hour. After which**,** 3% (by weight of the resin system) of the aerogel was added and stirred into the solution before dip coating the CFRP substrates (as described previously) and curing, again for a minimum of 48 hours. The preparation of the final batch of the coating was identical to the second batch with the only exception being the time of addition of the aerogel particles. Here, the resin solution (with the wetting agent) was left in the vacuum for 1.5 hours before the addition of the aerogel. The coating process and the cure time were similar to the previous batches.

It must be noted that the coated samples were further trimmed to 30*30 (mm^2) sizes to remove the excess coating aggregated on the sides of the samples. The pure CFRP samples will henceforth be referred to as S(x) with (x) denoting the sample number. Similarly the samples coated with the pure resin are named P(x) and samples with the aerogel/epoxy coating follow the same naming convention as the bulk materials

(aerogel addition samples). The coated fatigue and tensile samples were also prepared using a similar method, wherein the aerogel particles were added after degassing the resin for 1 hour and the CFRP substrate was dip coated.

For the sake of clarity, the different sample names used in the designation of various aerogel/epoxy composite are listed in Table 7.

Table 7 Sample summary and description for aerogel/epoxy composites

Main property	Sample name	Description
Mass fraction	**P(x)**; where x is the sample number	Resin and hardener
	1P(x); where x is the sample number	0.01 Mass fraction of aerogel
	2P(x); where x is the sample number	0.02 Mass fraction of aerogel
	3P(x); where x is the sample number	0.03 Mass fraction of aerogel
Cure Kinetics	**Batch 1**	Resin and hardener
	Batch 2	Resin, hardener and aerogel
	Batch 3	Resin, wetting agent, hardener and aerogel
Aerogel addition	**(x)A**; where x is the time of aerogel addition	Resin and Hardener
	(x)B; where x is the time of aerogel addition	Resin, hardener and aerogel
	(x)C; where x is the time of aerogel addition	Resin, wetting agent, hardener and aerogel

3.1.1.3 Carbon fibre reinforced plastic (CFRP)

The carbon fibre substrates were prepared using a multiaxial ACG (Advanced Composites Group Ltd, UK) MTM46/CF6657- 38%RW-DC prepreg cut and

assembled on a flat mould to a thickness of ~5mm. These samples were initially cured at 80^0C for 1 hour using resin film infusion (RFI) by ramping up the temperature from 20^0C to 80^0C at 3^0C/min. However consolidation problems and the use of aged material resulted in bleed issues during the process. Hence, the samples were subsequently cured in an autoclave at 120^0C for 1 hour using 50 psi (80^0C to 120^0C at 3^0C/min). The top surface of the composite was then cleaned using a 400 grit paper, washed and dried.

The composite plate was cut into samples of 40*40 (mm) using a rotating blade for the resin coating and thermal conductivity testing. The surfaces of samples used as substrates for the coating were roughened using an old 120 grit sand paper. All the samples were then subsequently washed with water and dried before coating them.

To prepare the tensile and fatigue specimens, the composite samples were cut to 150*25 (mm) and tabbed at both ends using aluminium tabs.

3.2 Experimental Apparatus

This section describes the various experimental apparatus and techniques used in the present study to characterise the different materials. Since the majority of characterization and testing was carried out on aerogel/polymer samples, a flowchart describing the type of testing carried out as well as the properties identified for each material is given in Figure 10.

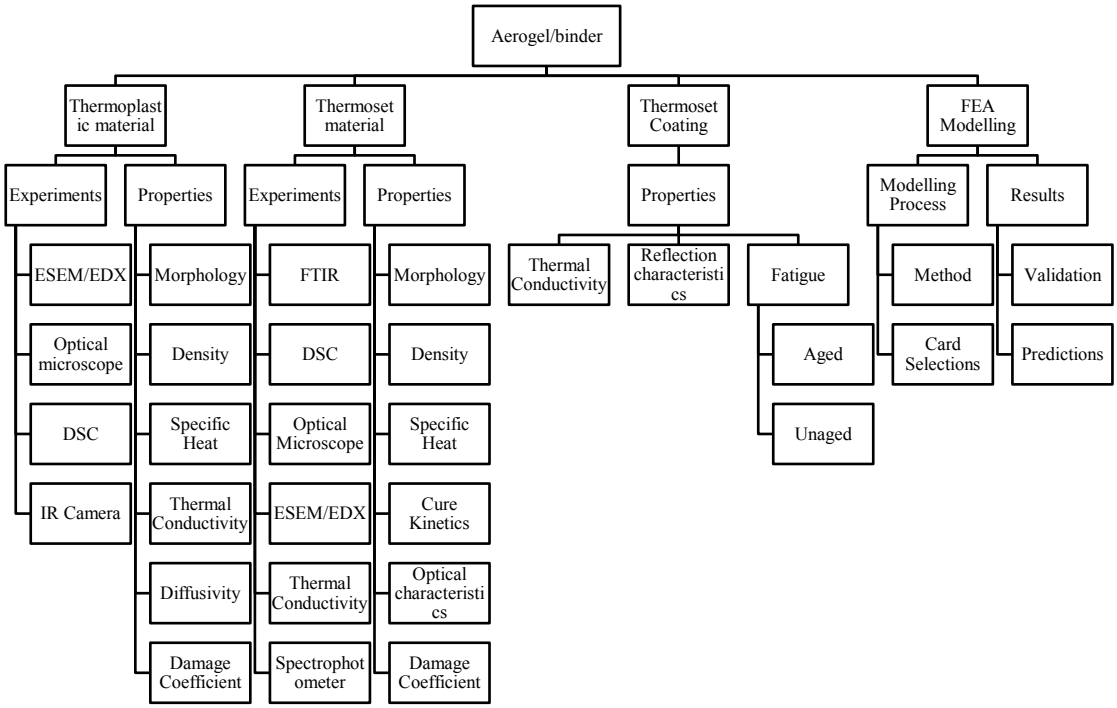

Figure 10 Experimental methods for aerogel/polymer composites

3.2.1 **Material morphology**

The various samples in the study were studied using a Nikon Optiphot image acquisition system equipped with Leica Application suite for optical imaging and a Phillips XL30ESEM environmental scanning electron microscope (ESEM) equipped with an energy dispersive X-ray spectroscope (EDX). The optical imaging was performed under 5X and 40X magnifications.

ESEM/EDX was used to study the aerogel/PA-6 samples before they were compression pressed into their final shape and the pressed plaque was subsequently imaged optically. However, both imaging techniques were used on the same aerogel/epoxy samples to determine their morphology.

3.2.2 **Density**

The density of each individual sample was determined by the equation used to calculate the density of a solid, uniform body as shown in Equation 1 [161].

$$D = \frac{m}{V}$$

Equation 1

Where: D = Density in g/cm^3; m = Mass in g; V = Volume in cm^3

The mass of the samples was measured using a weight balance and the volume was calculated by measuring the dimension of the specimen using a line gauge.

3.2.3 **Differential Scanning Calorimetry (DSC)**

A differential scanning calorimeter was used to calculate the specific heat capacity of the aerogel/polymer composite. Additionally, the apparatus was also used in the determination of non-isothermal cure kinetics of the resin and the aerogel/epoxy composite in the current study.

3.2.3.1 Specific heat

The materials, whose specific heat had to be calculated, were subjected to a DSC run in a TA 2920 MDSC instrument. The samples were heated to 400 ^{0}C (for the PA-6 matrix) and 200^{0}C (for the epoxy matrix) at 5 ^{0}C/min (under a nitrogen gas flow). The recorded graphs were then used in the calculation of the specific heat for each individual sample.

The specific heat capacity of the material was calculated using the DSC and the method outlined by O'Neill [162]. In this method, the ordinate deflections of the sample are compared against a known reference material (sapphire) and the specific heat of the sample was calculated according to Equation 2.

$$\frac{C_p}{C_p{}^r} = \frac{m^r y}{m y^r}$$

Equation 2

Where the superscript *r* stands for the reference material and C_p = specific heat capacity; *m* = mass; *y* = ordinate deflection.

3.2.3.2 Cure kinetics

The cure kinetics of the aerogel/epoxy samples were determined using a Q200 DSC (TA instruments) under a 50 mL/min nitrogen purge coupled to a TA Refrigerated Cooling System 90 (RCS 90). The obtained peaks were then analysed using the TA Universal Analysis 2000 (version 4.5A) software.

Each batch was subjected to four dynamic runs at constant heat rates- 5^0C/min, 10^0C/min, 15^0C/min and 20^0C/min from 40^0C to 300^0C. The materials were put in Tzero Aluminium pans wherein, the lids were pressed onto the pans using a sample encapsulation press. It must be noted that efforts were made to maintain the mass of the material in the Tzero pans between 13-16 mg. The cure kinetics parameters for the three batches were calculated using three different methods and the results compared.

3.2.4 **Thermal diffusivity**

The thermal diffusivity of aerogel/Pa6 composites were measured using a Thermal Wave Imaging Thermoscope II pulsed thermographic inspection system [163] equipped with a FLIR SC7000 Infrared camera. The experimental parameters are listed in Table 8.

Table 8 Thermoscope Parameters

Parameter	Value
Window	640*512 pixels (Full Frame)
Flash Pulse Length	10ms
Acquisition Frequency	25Hz
Acquisition Time	50s

3.2.5 Optical Characteristics

The optical transmission of the aerogel/epoxy samples were measured using an UV-visible-NIR spectrophotometer, Jasco V-670 at normal incidence wherein the surrounding air medium in the sample chamber was used as reference for spectral calibration. The 3 batches of samples were measured in the wavelength range of 300nm to 1500nm at a scan speed of 400nm/min. As discussed previously, each batch had three different test samples into which the aerogel was added at 0.5 hours, 1 hour and 1.5 hours (for batches B and C) respectively. With respect to batch A- the pure resin; the samples were measured without any mixing of the aerogel and the wetting agent after required time period- this batch was used as a control. It should be noted that the curing of the resin on the glass slide was carried out during the measurement period itself.

As shown in Figure 11, the glass substrate was placed vertically in the sample chamber of the spectrophotometer. Six consecutive scans at 5 minute intervals for each test sample were undertaken to evaluate the transmittance characteristics of the curing sample. The film thickness and uniformity would not remain same for the 6 runs during the process due to the resin flow and the sample's change of phase from liquid to solid which may introduce an uncertainty in comparing the transmittance

spectra (e.g. change in intensity) of various test samples. However, the measurement error is expected to be minimum since the film is quite thick (few mm) in nature.

In addition, total reflectance of the cured sample in the range of 200-1500 nm, e.g., both diffuse and specular, was measured using an integrating sphere of 60mm diameter and fluro-polymer based spectralon as a calibration standard. This gives the nature of light scattering due to the presence of aerogel and/or other particulates in the samples.

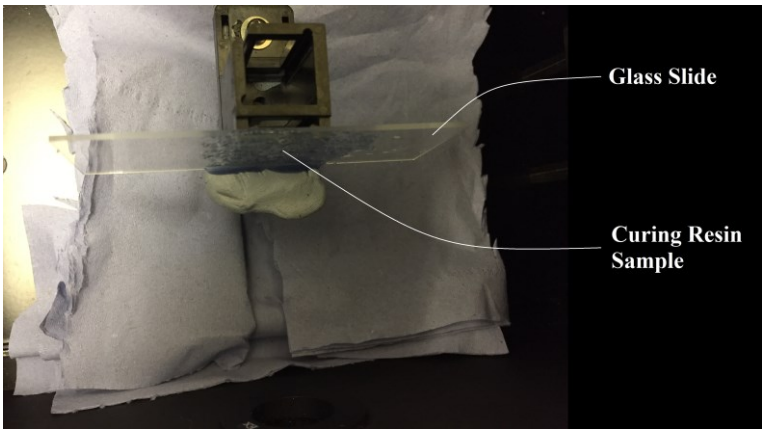

Figure 11 Test sample placed in the chamber of the spectrophotometer during curing process

3.2.6 **Thermal conductivity**

The present research employs three different methods to determine the thermal conductivity of various samples due to the unavailability of equipment/technicians and the cost of external testing. However, different specimens from a single batch were subjected to the same type of testing thereby ensuring the possibility of cross comparison.

3.2.6.1 Diffusivity

This method was used to determine the thermal conductivity of aerogel/PA6 samples. To calculate the thermal conductivity, the formula in Equation 3 was used.

$$k = (\alpha * \rho * c)$$

Equation 3

Where k = Thermal conductivity in W/(m K); α = Thermal diffusivity in m^2/s, ρ = Density in g/m^3; and c = Specific heat in J/(g K)

The thermal diffusivity value was determined using the IR camera, density was calculated using mass and volume and, specific heat was calculated using a DSC.

3.2.6.2 Pyroheater

This technique was employed to characterise the aerogel/epoxy coatings described previously. To calculate the thermal conductivity, Equation 4 was made use of which describes the one dimensional heat conduction through a plane wall under steady state conditions as given in [164, p. 378].

$$k = \frac{Q/A}{\Delta T/L}$$

Equation 4

Wherein k is the thermal conductivity of the sample; Q is the rate of heat flow (conduction) across the sample; A is the cross sectional area; ΔT is the temperature difference across the sample and L is the thickness.

The cross sectional area (A) and the thickness (L) of the samples were measured using a line gauge. The temperature difference across the sample (ΔT) was measured at three temperatures- 50^0C, 75^0C and 100^0C. The heat was provided by a Pyro Heater connected to a Eurotherm 2216e (Schneider Electric, United Kingdom) controller. For each temperature, the system was allowed to stabilise for 1 hour (to attain steady state) before the temperatures at the top and the bottom of the sample were recorded using cement on polyimide thin film thermocouples by TC Direct (United Kingdom).

A schematic diagram and a pictorial description of the setup is shown in Figure 12 (a) and (b) respectively.

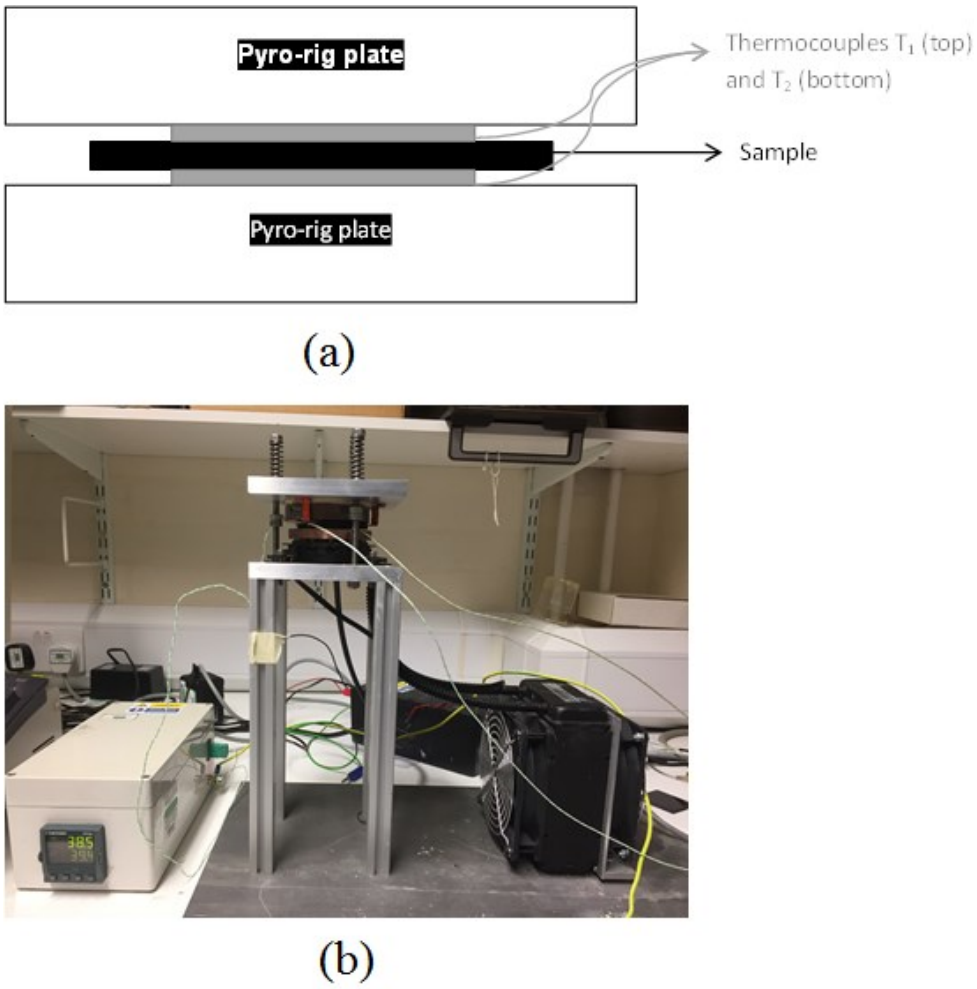

Figure 12 (a) labelled diagram of the heating setup; (b) Image of the pyro heater setup along with the controller

To calculate the heat flow across the sample (Q), a material of known thermal conductivity value- a standard was used. Since the thermal conductivity was known, Q could be calculated at different temperatures using Equation 4. Three different runs at the above-mentioned temperatures were conducted and the average Q value for each temperature was used for subsequent thermal conductivity calculations. The standard used was a lead zirconate titanium (PZT) disc (PC 8) by Morgan Matroc (United Kingdom).

To calculate the thermal conductivity of the coated materials, 5 specimens for each sample were utilised wherein the cross sectional area for each of the 5 samples was calculated using the average of three separate length and breadth measurements. Similarly the thickness used was also the average of three measurements. Using these average values, the thermal conductivity for each sample was determined at the three temperatures using the pyro rig. Finally for each temperature, the average of the 5 specimens was used as the thermal conductivity of that particular material.

3.2.6.3 Direct

The thermal conductivity of the aerogel/epoxy bulk materials were measured directly using the TCi Thermal conductivity analyser (C-Therm**)**. As the samples were stiff, three drops of distilled water was used as contact agent and added onto the sensor before the samples were placed in position. For each sample, 10 measurements were taken and the average value was used as the thermal conductivity of that sample.

3.2.7 **Tensile Testing**

The CFRP samples produced for fatigue testing were initially subjected to a uniaxial tensile load to determine their ultimate tensile load. The test machine used was an INSTRON 5500R with a crosshead speed of 1 mm/min speed. The test was run until the material failed and the load at failure was recorded. 5 specimens for each batch were tested and the average was used as the ultimate tensile load.

The aged specimens for both the tensile and fatigue tests were isothermally heated to 70^0C in an environmental chamber for the specified duration.

3.2.8 **Fatigue**

Fatigue testing for the aged, unaged and coated samples was conducted on a 20kN Denison Mayes Group (DMG) hydraulic fatigue frame coupled to Rubicon Control

Interface software. Testing was carried out with a Tensile-Tensile (0) loading criteria with an R value of 0.1. A Sinewave form with a 5Hz frequency was chosen with the end point being the fracture of the material. The specimens used for both tensile and fatigue tests were tabbed at both ends and cut to 150*25mm sizes.

To plot the S-N curve of the materials four different load levels were fatigued to failure at 50%, 55%, 65% and 80% of the ultimate tensile load determined by the tensile test. For each load level, three different specimens were tested and noted. Loads lower than 40% were not considered since they exceed the run-off time of 1,000,000 cycles for the unaged CFRP specimen.

3.3 Finite Element Model

A finite element (FE) model of the aerogel/epoxy coated substrate was built using LS-PrePost- 4.3dp and solved through the LS-DYNA solver to try and predict the behaviour of the coating under different loading environments.

The geometry of the substrate was a rectangular plate of 0.03*0.03*0.005 (m) which was similar to the experimental samples used for pyroheater testing. The coating was also modelled as rectangular layer with dimensions of 0.03*0.03*0.0007 (m) above and below the CFRP substrate. The thickness of the coating was taken to be the average value of the dip-coated experimental samples.

3.3.1 Material Card

Since the model was subjected to thermal analysis, only the thermal material cards were defined. The substrate's properties were defined using the MAT_THERMAL_ORTHOTROPIC card. The coating was modelled using the MAT_THERMAL_ISOTROPIC card because of the homogenous distribution of aerogel particles within the resin. The properties of the substrate and coating used are

presented in Table 9. The coating's thermal conductivity was the experimental value of the bulk material determined previously. The other properties of the coating were calculated using the rule of mixtures and individual properties of aerogel and the resin system. The volume fraction of aerogel used in the rule of mixture was 0.21 determined from the densities of the resin and aerogel in Table 9.

Table 9 Material Card Properties. The sources of the values are given in the brackets next to their respective values.

Property	**Substrate**	**Coating**	
Density (kg/m^3)	1460 [165]	Aerogel	135 [166]
		Resin	1190 [167]
		Coating	**968.45**
Heat Capacity (J/(kg*K)	1170 [165]	Aerogel	2100 [168]
		Resin	1890 [165]
		Coating	**1934.1**
Thermal Conductivity (Axial) (W/(m*K))	14.57 [165]	Experimental Determined	
Thermal Conductivity (Transverse) (W/(m*K))	0.75 [165]		

3.3.2 Elements and Meshing

The work of Shapiro [169] suggests the use of 8 node brick elements as one of the element types that could be used in thermal analysis. Hence, the substrate and the coating were modelled using fully integrated quadratic 8 node solid elements with nodal rotations (ELFORM = 3). This element formulation gives accurate results in small strain conditions [170]

3.3.3 **Loading and Simulation**

The temperature was applied on the nodes at the top of specimen through the BOUNDARY_TEMPERATURE_SET card using DEFINE_CURVE. The initial temperature for all the nodes were set to 23^0C using the INITIAL_TEMPERATURE card. Because the material properties for the substrate and coating are assumed to be constant with respect to time and temperature, a linear transient analysis using a diagonal scaled conjugate gradient iterative solver (SOLVER = 3) was performed. An iterative solver was used due to its higher efficiency compared to a direct solver (LS-DYNA user manual [171]). The models also used a fully implicit time integration parameter to calculate the thermal timestep.

The coated models additionally made use of the CONTACT_AUTOMATIC_SURFACE_TO_SURFACE_SMOOTH card with the THERMAL option for both surfaces. Here, the heat transfer conductance was 100- an arbitrarily chosen high value with the minimum and maximum lengths to be 0.0002 and 1 respectively.

4 Results

4.1 Thermoplastic Binder

The observations and data from the experiments conducted on aerogel/PA-6 samples are given in this section. Initially, the microstructures of the extruded material (all three samples) were analysed under a scanning electron microscope (ESEM) and an optical microscope. Then, the density, thermal diffusivity and the specific heat capacity of the materials were measured using the methodology identified in the previous section. The following results and their inferences are published by the author [172] and are as follows.

4.1.1 Density

The density measurements were carried out on compression-moulded plates for the three samples- A, B and C. The mean density (shown in Table 10) was calculated by averaging the density of three different specimens per sample.

Table 10 Average density measurements

Sample	A	B	C
Mean Density (g/m^3)	1.02x10^6	9.8x10^5	9.2x10^5

The results show that the density of pure PA-6 is 1.02x10^6 g/m^3 which agrees well with the manufacture's number of 1.14x10^6 g/m^3 [173]. The difference in the values could be due to the reduced accuracy of the measurement techniques used in the current work; the dimensions of the samples were measured using a line gauge, which has a least count of 1 mm. However, the samples with the aerogel (B and C) show slightly decreased densities of 9.8 x10^5 g/m^3 and 9.2 x10^5 g/m^3 respectively. As predicted, samples C showed the lowest density, which could be due to their improved ability to retain the aerogel structure.

4.1.2 **Morphology**

4.1.2.1 Environmental scanning electron microscope

SEM-EDX results of the extruded samples before being compression pressed are shown in Figure 13,

Figure 14 and Figure 15 for samples A, B and C respectively. From the EDX results, it is inferred that silica was detected in samples B and C. However, further analysis on sample B (Figure 16) showed an almost-continuous presence of silicon and oxygen across an extruded piece, thereby providing evidence for uniform dispersion of silica. Additionally, the visual image of the SEM showed homogeneity across the cross section. Therefore it can be suggested that although Sample B had silica along with PA-6, the structure of the aerogel had collapsed (almost completely) and only particles of silica have been dispersed uniformly in the PA-6 matrix.

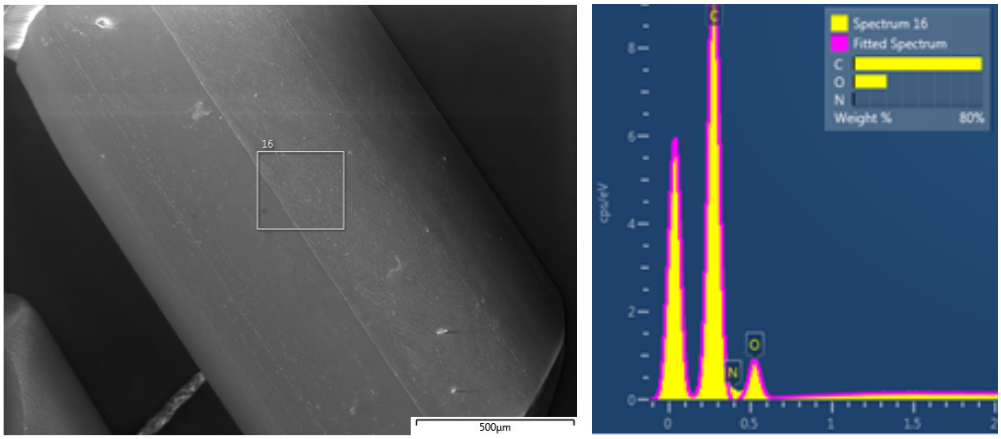

Figure 13 ESEM and EDX results of extruded PA-6 (Sample A). The image on the left is the ESEM image of the sample and the spectra on the right corresponds to the EDX spectra of the selected area in the microscopic image. X-axis in KeV.

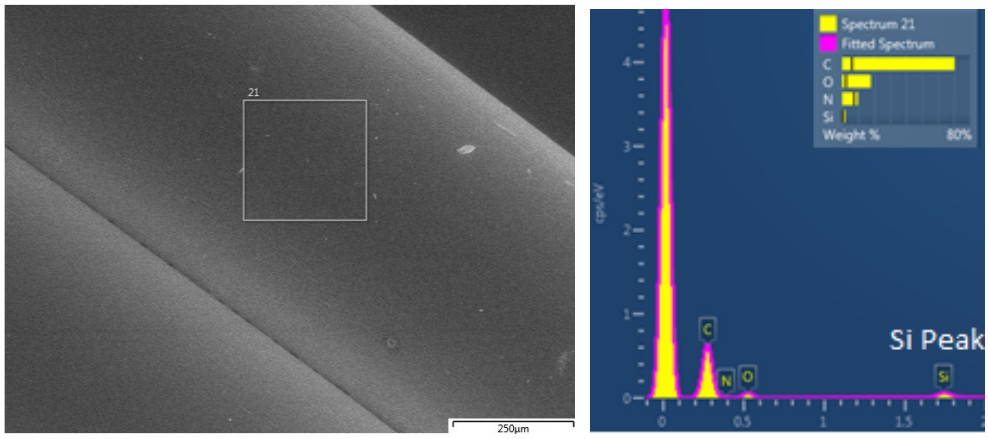

Figure 14 ESEM and EDX results of extruded PA-6 with SiO2 (Sample B). The image on the left is the ESEM image of the sample and the spectra on the right corresponds to the EDX spectra of the selected area in the microscopic image. X-axis in KeV.

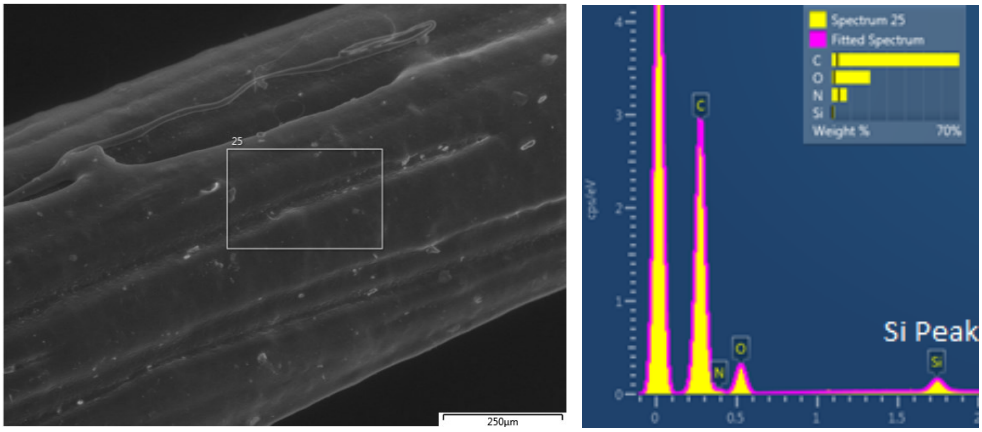

Figure 15 ESEM and EDX results of extruded PA-6 with SiO2 (Sample C). The image on the left is the ESEM image of the sample and the spectra on the right corresponds to the EDX spectra of the selected area in the microscopic image. X-axis in KeV

The SEM image (Figure 15) of Sample C showed a more coarse structure when compared to the previous samples. Although some extruded pieces of sample B did show some roughness, sample C had significantly more roughness which can be seen from the SEM scans. In addition, the sample was also scattered with small particle-like structures. When one of the structures was analysed (Figure 17), the EDX revealed a higher amount of silicon and oxygen compared to the matrix and previous samples. This was also confirmed by the weight percentages of the various elements

(in sample C) shown in Table 11. When compared to an area in Figure 15 (represented as Spectrum 25), it was noticed that the particle (represented as Spectrum 29) has a higher silicon content (increased from 1% to 11.73%) and oxygen content (increased from 20.95% to 33.07%). It is believed that this could either be a result of agglomeration of the silica particles during processing or the retention of the aerogel structure wherein, these particles are the unmodified silica aerogel.

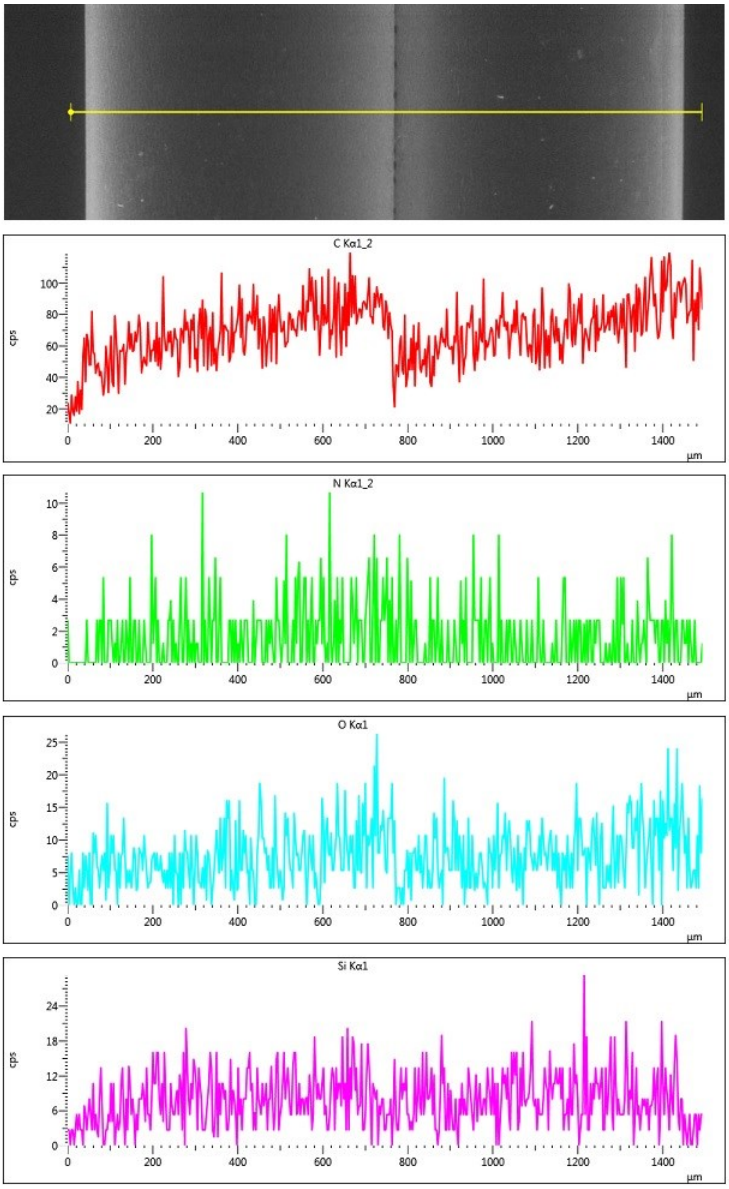

Figure 16 Line scan of a single extruded particle via SEM-EDX of Sample B for (top to bottom) Carbon (red), Nitrogen (green), Oxygen (blue) and Silicon (purple). The vertical centre line in the sample is due to the application of a twin head die on the extruder and the subsequent joining of the two threads

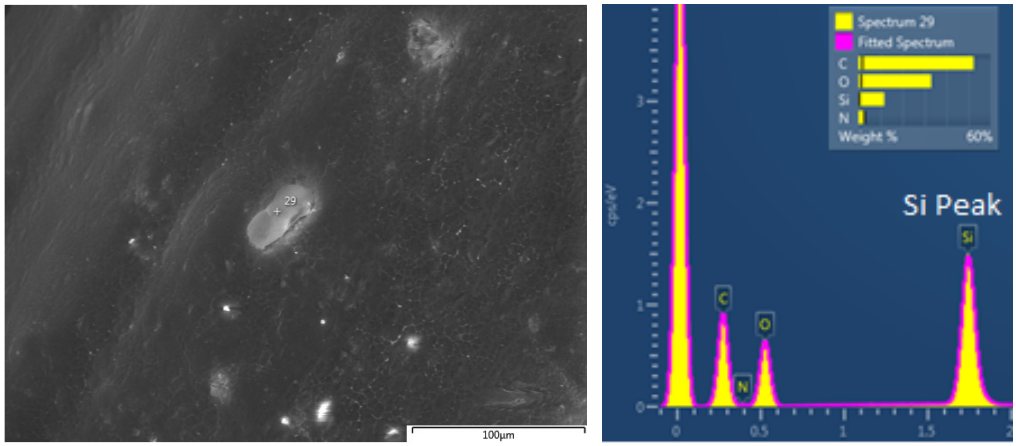

Figure 17 ESEM and EDX of a particle present in Sample C. The image on the left is the ESEM image of the sample and the spectra on the right corresponds to the EDX spectra of the selected spot in the microscopic image. X-axis in KeV.

Table 11 Weight percentages of the EDX Spectrums of Sample C

Spectrum Label	C	N	O	Si	Total %
Spectrum 25	69.92	8.12	20.95	1	99.99
Spectrum 29	52.35	2.85	33.07	11.73	100

4.1.2.2 Optical Microscope

The optical microscope showed a similar structure between samples A and B, however the ESEM and EDX results (discussed in the previous section) confirmed the presence of silica in Sample B, thereby suggesting that the aerogel structure completely collapsed in sample B. Further, Figure 18 indicates certain particle-like structures (circled in white) in sample B. It is believed that these are the silica particles that resulted from the destruction of the aerogel structure.

Sample C on the other hand, showed a different morphology compared to samples A and B. Additionally, there were certain regions within the sample that were darker and larger (Figure 19) than the individual particles seen in sample B, hence these were thought to indicate the presence of aerogel within the sample. It can also be inferred from the results that the aerogel structure was not completely destroyed as the silica

particles stayed together. However, the pores within the aerogel could have been filled with the PA-6 matrix during extrusion and compression pressing. Thus, the single run at 5 RPM showed an improvement compared to the previous attempts.

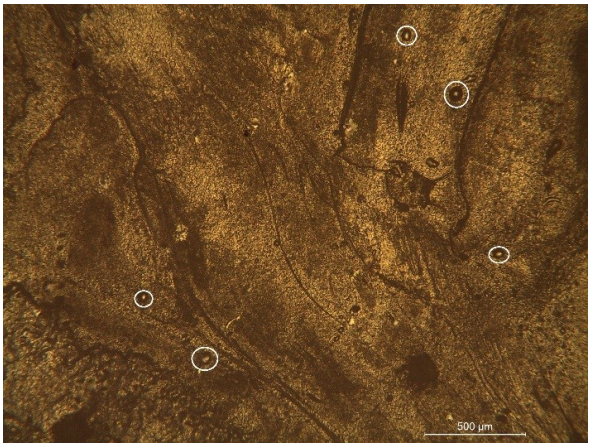

Figure 18 Sample B with possible Si particles (circled in white)

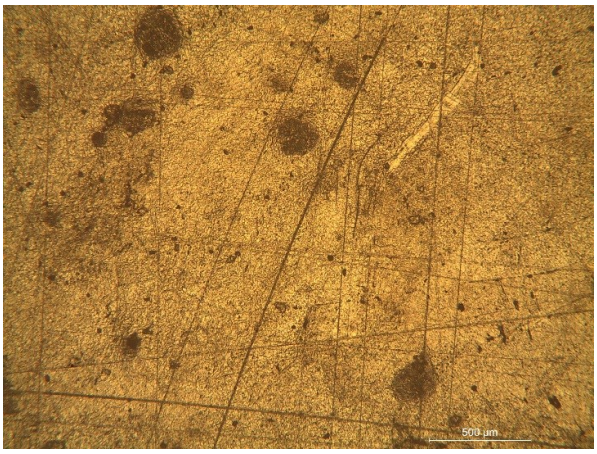

Figure 19 Sample C

4.1.3 **Thermal Diffusivity**

Three samples were tested for thermal diffusivity, the average value for each type of sample was calculated [174] from the results obtained; one such set of diffusion maps is given in Figure 20 and Table 12 lists the average mean diffusivity and standard deviation for the samples. The average values were calculated using the mean diffusivity and the standard deviation measurements across three different specimens for each sample.

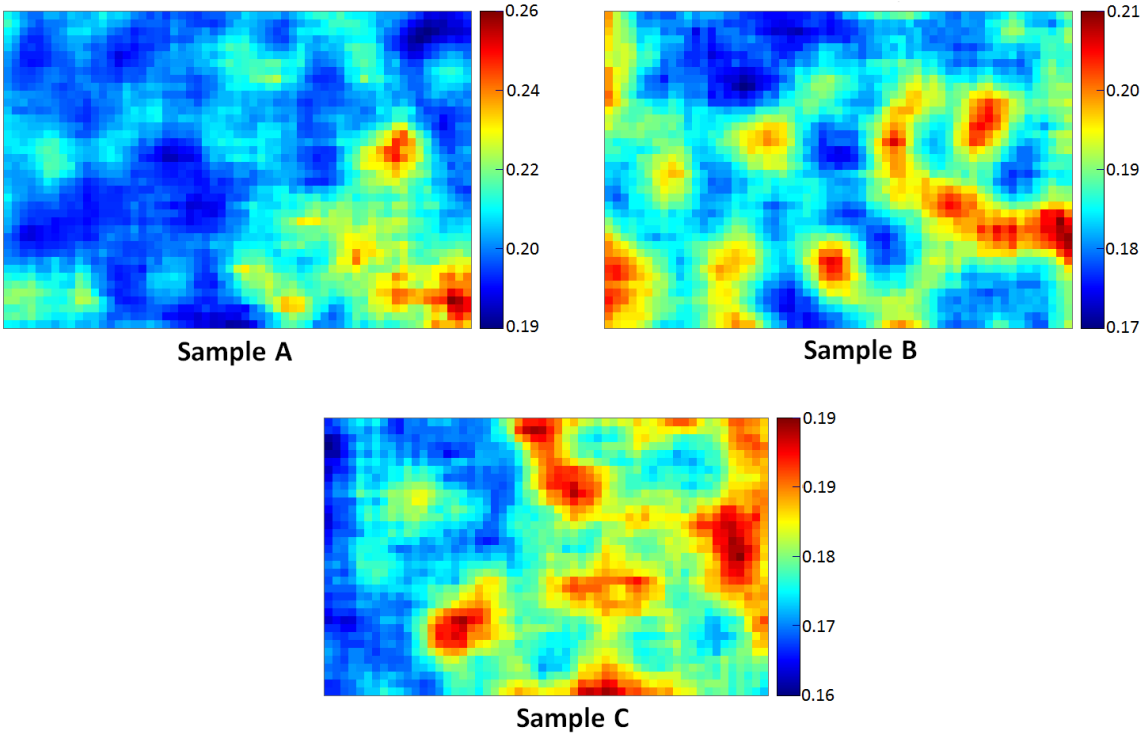

Figure 20 Thermal diffusivity maps of Samples A, B, C where the diffusivity is indicated by the colour bar

Table 12 Average diffusivity and standard deviation values

Sample	Average Values	
	Mean Diffusivity (m^2/s)	**Standard Deviation (mm^2/s)**
A	$2.34x10^{-7}$	0.0340
B	$1.875x10^{-7}$	0.0125
C	$1.7710x10^{-7}$	0.0084

From the measurement results in Table 12, it was observed that the PA-6/Aerogel composites showed lower diffusivity values compared to the pure PA-6 sample thereby, pointing to greater thermal insulation. Additionally, Sample C showed the lowest mean diffusivity value- $1.7710x10^{-7}$ m^2/s confirming that the softer conditions during extrusion and pressing contributed to an improved thermal performance by

retaining more aerogel (and its structure) within the composite. It is also seen that sample C had the lowest average standard deviation suggesting that it had conducted heat more uniformly across a given cross section, thereby providing a potentially stronger thermal fatigue performance.

4.1.4 **Specific Heat Capacity**

The DSC profiles together with the baseline and sapphire standard calibration (both of which are needed for the specific heat calculation) for Samples A, B and C are given in Figure 21. From the graphs, it is observed that there is an endothermic peak close to 225^0C for all the samples which is believed to be due to the melting of PA-6, since the manufacture's data [175] states the same to be at 222^0C. Furthermore, sample C also showed an endothermic peak at around 395^0C unlike the other two samples which, is thought to be due to the thermal degradation of nylon. Although the peak is only seen in sample C, a similar trend is observed in the DSC plots for samples A and B. Hence, it is predicted that they too will show an endothermic speak (at higher temperatures). The reason for sample C's premature peak could be due to the destabilizing effect of the aerogel as described by Levchik et al [176]. The authors studied the thermal decomposition of nylon 6 along with various fire retardants and concluded that the destabilization of nylon 6 could reduce the thermal decomposition temperature by as much as 70^0C (as in the case of ammonium polyphosphate).

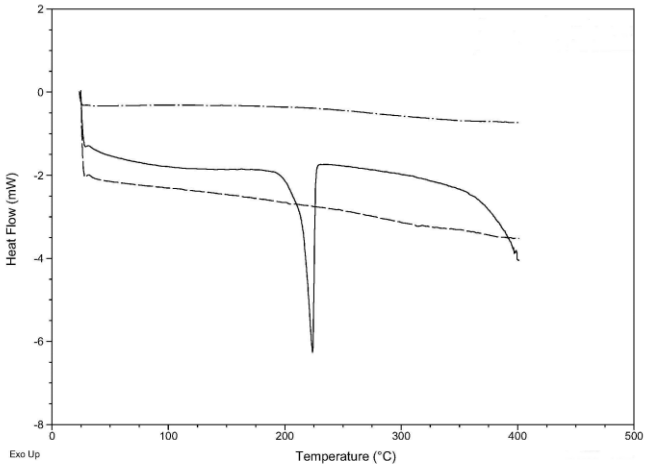

Sample A

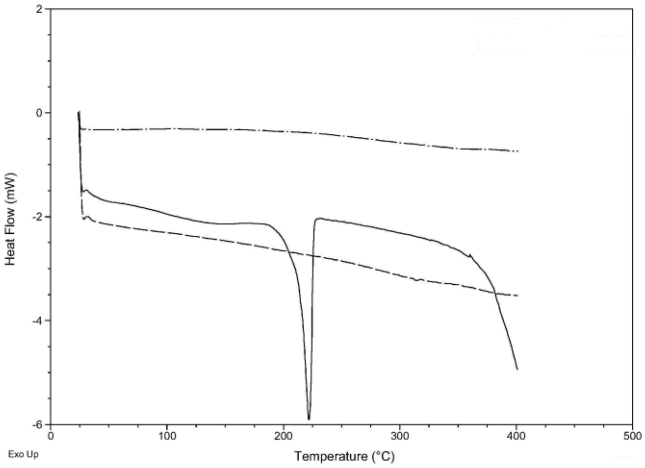

Sample B

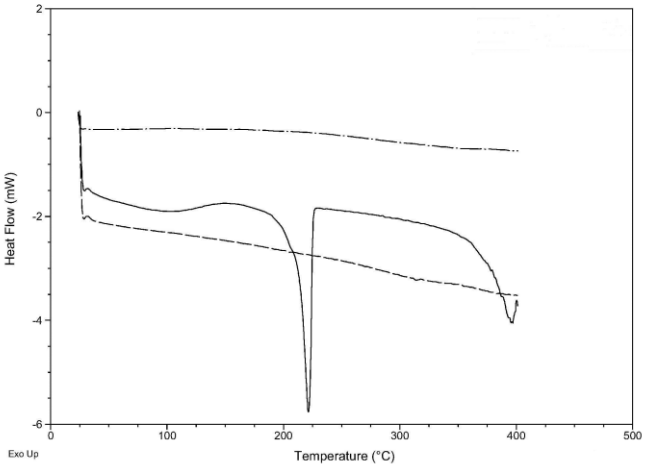

Sample C

Figure 21 DSC maps of Samples A, B and C (solid line) with the baseline (dashed and dotted line) and sapphire standard (dashed line) curves imposed on them. The heat flow (in mW) is on the y-axis and the temperature (in ^{0}C is on the x-axis)

The specific heat capacity of the samples was calculated using the DSC curves in Figure 21. The values of the specific heat capacity of the sapphire standard was taken from Ditmars et al [177] and the mass of the reference sample was measured to be 0.02626 g. Because the specific heat capacity of the standard sapphire was given for every 10K, the closest value corresponding to the required temperature was considered. Therefore for example, if the specific heat capacity at 50^0C (323K) was required, then the corresponding value at 320K for the standard sapphire was chosen from [177]. The calculated specific heat capacity for the samples A, B and C are listed in Table 13 and graphically plotted in Figure 22. From the results, it is seen that sample A has lower values of specific heat across the whole temperature regime due to the addition of aerogel in the composite samples. Additionally, the specific heats of all three samples are also seen to increase with temperature.

Table 13 Specific Heat Capacity Calculation

Sample	**Mass (g)**	**Temperature (^{0}C)**	**Specific Heat Capacity (J/(g ^{0}C))**
A	$7.47x10^{-3}$	200	2.64
		150	2.45
		100	2.37
		50	1.84
B	$7.01x10^{-3}$	200	3.39
		150	3.07
		100	2.78
		50	2.30
C	$6.44x10^{-3}$	200	3.24
		150	2.64
		100	2.93
		50	2.41

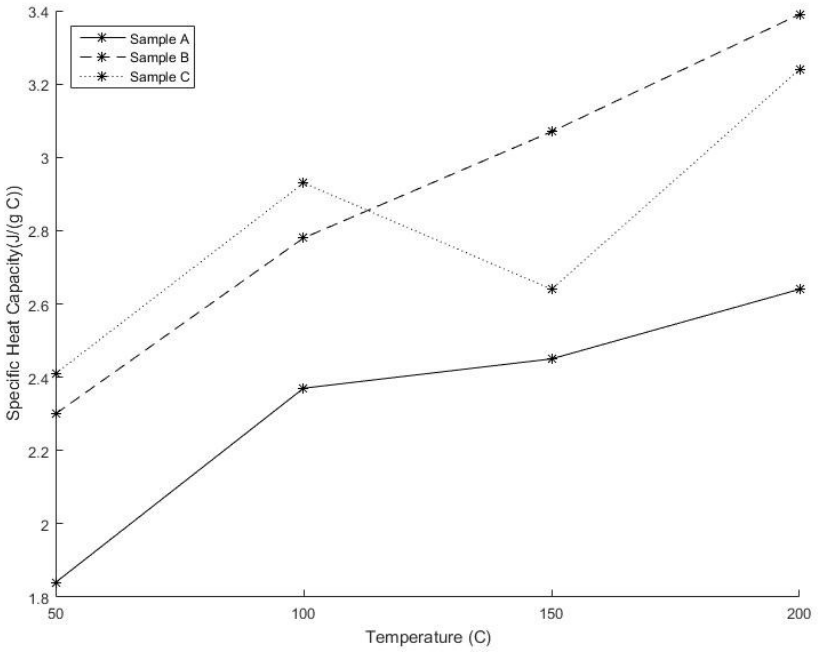

Figure 22 Specific heat capacities of PA-6/Aerogel Composites

4.1.5 **Thermal Conductivity**

The data for the density, thermal diffusivity and specific heat were taken from Table 10, Table 12 and Table 13 respectively. For thermal diffusivity and density, the average values were considered and for the specific heat; the value at 50^0C for each of the sample was used since this was the closest to room temperature. The thermal conductivity values are presented in Table 14.

Table 14 Thermal conductivity calculation

Sample	A	B	C
Thermal Conductivity (W/(m K))	0.44	0.42	0.39

The results show the value of sample A to be the highest and sample C to be the lowest. Thereby, further confirming the belief that sample C did manage to retain some of the aerogel within the matrix. Additionally, the thermal conductivity of

sample B is seen to be higher than sample C indicating a greater destruction of the aerogel in the former compared to the latter.

4.1.6 **Damage Coefficient**

In this section, the damage of the aerogel structure in a polymer matrix is quantified by placing the calculated thermal conductivity of the samples in relation to the theoretical upper and lower thermal conductivities. The derived term, referred to as damage coefficient, would allow an approximate mathematical measure of the destruction of the aerogel structure within a matrix.

The thermal conductivity values for the PA-6/Aerogel composite was theoretically calculated using the model described by Hamilton and Crosser [178] and shown in Equation 5. This model enabled the calculation of the thermal conductivity for two-component heterogeneous mixtures. The values calculated analytically provide the upper and lower bounds for the composite in this study. The thermal conductivity of the composite determined using the thermal conductivity of the silica aerogel provides the lower bound whilst the value calculated using the thermal conductivity of normal silica (simulating the complete destruction of the aerogel structure) defines the upper bound.

$$k = k_1 \left[\frac{k_2 + (n-1)k_1 - (n-1)v_2(k_1 - k_2)}{k_2 + (n-1)k_1 + v_2(k_1 - k_2)} \right]$$

Equation 5

Where k = thermal conductivity of the composite; k_1 = thermal conductivity of the matrix; k_2 = thermal conductivity of the filler; n = shape parameter which is assumed to be 3 since the thermal conductivity of the filler is a lot smaller than that of the matrix [178]; v_2 = volume fraction of the filler.

For the purpose of data analysis a thermal conductivity value (k_b) of 0.44 W/(mK) (from Table 14) was adopted for PA-6. For k_a, a value of 0.012 W/(mK) [179] (for the aerogel) was chosen together with a value of 1.4 W/(mK) [180] for pure silica. The volume fraction was calculated to be 0.327 (from a mass fraction of 0.04). The values of the theoretical thermal conductivity at the lower and upper bounds were calculated at 0.261 W/(m K) and 0.651 W/(m K) respectively.

Since, the theoretical bounds for the thermal conductivity of the composite have now been calculated; a damage coefficient is defined to assist the analysis. The damage coefficient (for the purpose of this study) is as given in Equation 6.

$$D_c = \frac{(k_s - k_l)}{(k_u - k_l)}$$

Equation 6

Where k_s = Thermal conductivity of the sample; k_l = Lower bound thermal conductivity and k_u = Upper bound thermal conductivity.

Using Equation 6, it is seen that the value of the damage coefficient (D_c) at the lower and upper bounds are 0 and 1 respectively. This agrees with the previous assumption that when the aerogel structure is unaffected, then there is no damage; hence the damage coefficient (D_c) is 0. However, when there is complete destruction of the aerogel such that only silica particles (without the aerogel structure) are present then the value of D_c becomes 1.

The results from Table 14 were used to determine the damage coefficient for samples B and C using Equation 6 and the calculated values are 0.41 and 0.33 respectively.

4.2 Thermoset Binder

Due to the difficulties in using a thermoplastic binder (as identified in the previous section), the aerogel particles were subsequently mixed in a thermoset (epoxy)

binding system. The results from this composite are reported here. Initially, a suitable mass fraction of aerogel to be added into the material was identified. Then, the research moved on to try and identify the effects of the aerogel filler on the curing of the resin through a cure kinetic study. And finally, the most efficient time of aerogel addition during the cure process was estimated using experimental data. Throughout the process, the suitability of using a wetting agent to improve the interface between the filler and the binder material was also investigated.

4.2.1 Mass fraction estimation

The initial part of the aerogel/epoxy composite investigation was to use experimental data and identify the ideal mass fraction of aerogel to be added into the epoxy binder. Three different mass fractions- 0.01, 0.02 and 0.03 (1P, 2P and 3P respectively) were studied by measuring their density, specific heat capacity and FTIR spectra.

4.2.1.1 Density

The density measurements of the aerogel/epoxy samples are listed in Table 15 along with the average density and standard deviation measurements for each batch. The densities of the pure epoxy samples agree well with the density given by the manufacturer (in the product data sheet) of the resin which is between 1.14-1.18 g/cm^3 [160]. Since a custom hardener was used, the exact density of the hardener is not known however, the hardeners described in the resin product data sheet all show a density between 0.93-1.00 g/cm^3. Therefore if we consider these values and that of the pure resin, the measurements in this work fit the data in the literature.

However, the density values and the averages between the batches do not show any significant differences. This could be due to the mass fraction of the aerogel which may not have been large enough to significantly affect the density of the material.

Another explanation could be the destruction of the aerogel; according to [180], the minimum density of silica is 2.17 Mg/m^3 (g/cm^3) which is higher than the density of the resin and the aerogel, therefore the resultant formation of the denser silica particles (due to the partial destruction of the aerogel structure) could have balanced the loss in density due to the aerogel.

Table 15 Density measurements of epoxy samples

Sample	Volume (cm^3)	Mass (g)	Density (g/cm^3)
P1	22.56	26.32	1.17
P2	22.28	25.59	1.15
P3	22.28	25.90	1.16
P4	21.65	25.04	1.16
Average			**1.16**
Standard Deviation			**0.008**
1P1	21.80	25.08	1.15
1P2	21.80	25.41	1.17
1P3	21.80	25.34	1.16
1P4	21.65	25.18	1.16
Average			**1.16**
Standard Deviation			**0.008**
2P1	22.12	26.50	1.20
2P2	21.80	26.32	1.21
2P3	21.80	25.62	1.18
2P4	21.80	25.47	1.17
Average			**1.19**
Standard Deviation			**0.018**
3P1	22.28	25.56	1.15
3P2	22.28	25.66	1.15
3P3	22.28	25.35	1.14
3P4	22.28	25.82	1.16
Average			**1.15**
Standard Deviation			**0.008**

4.2.1.2 Specific Heat

The DSC plots of the aerogel/epoxy samples are shown in Figure 23, Figure 24, Figure 25 and Figure 26. The most visible peak in the curve of the pure epoxy and the composite samples is the endothermic peak at ~75°C. According to the resin product data sheet [160], the glass transition temperature for the resin cured at room temperature for 24 hrs and then between 60-65°C for 15 hrs is 70-75°C. Therefore, because the processing parameters in this work have a room temperature and post curing cycle at ~64°C for the pure epoxy samples and an accelerated curing at ~60°C for the composite samples, the endothermic peak is believed to be due to the glass transition of the resin.

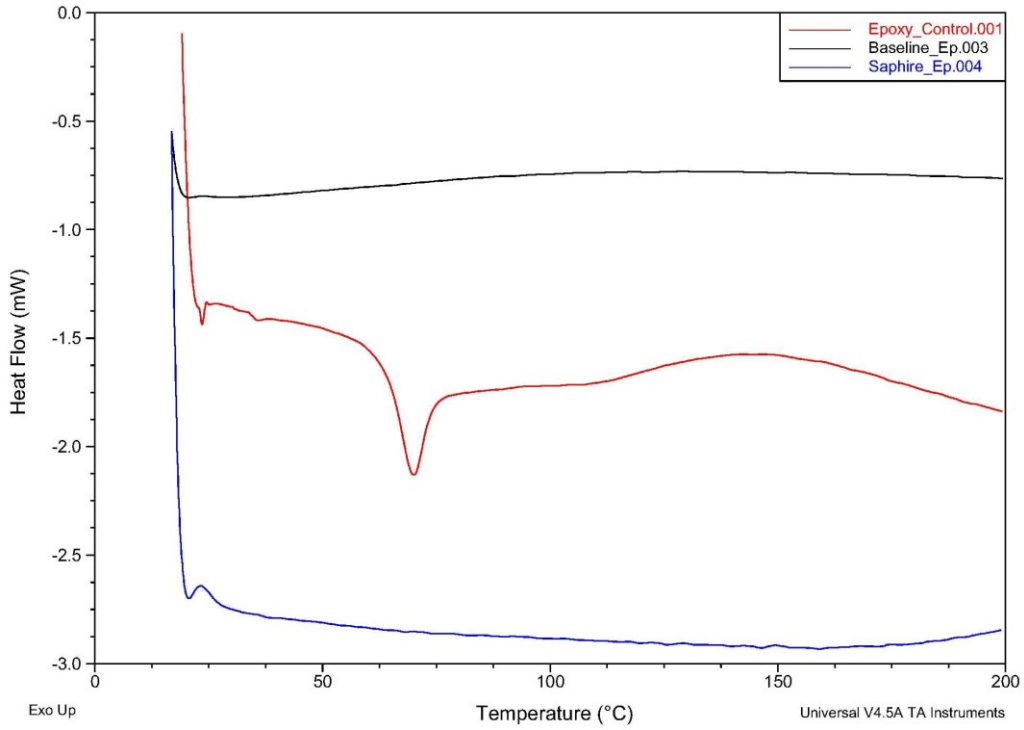

Figure 23 Pure Epoxy (P)

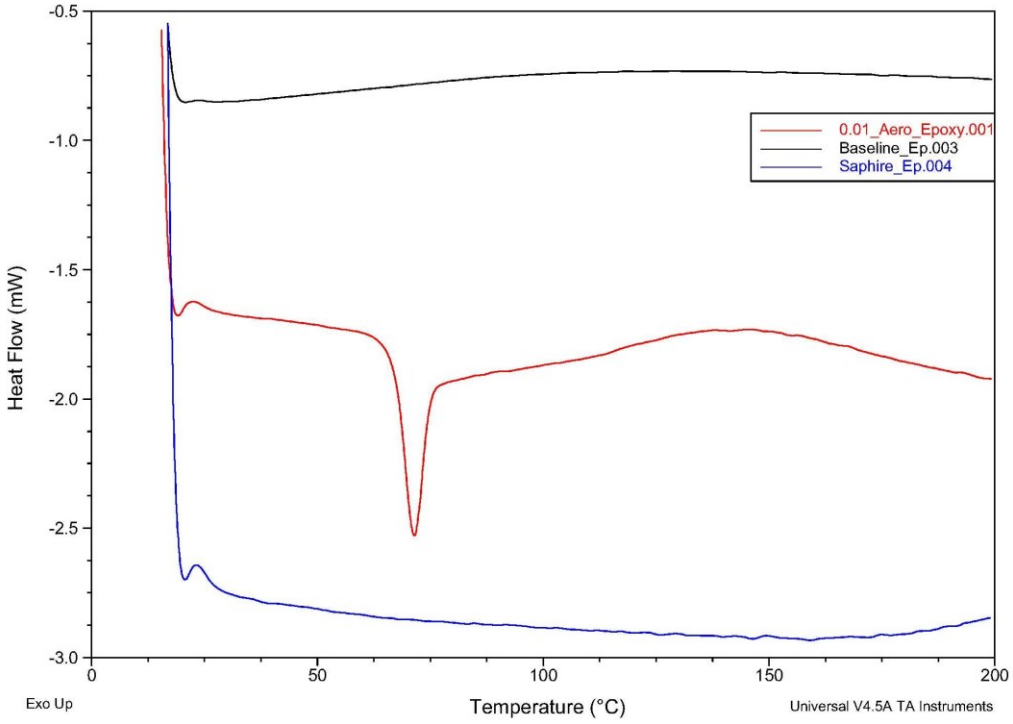

Figure 24 0.01 Aerogel/Epoxy (1P)

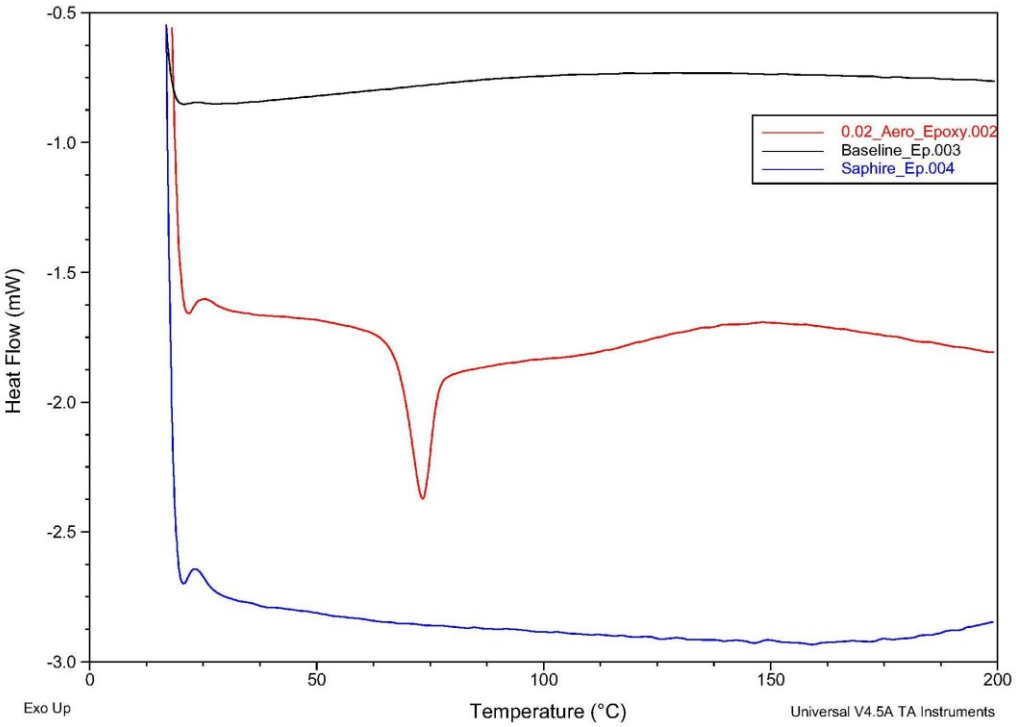

Figure 25 0.02 Aerogel/Epoxy (2P)

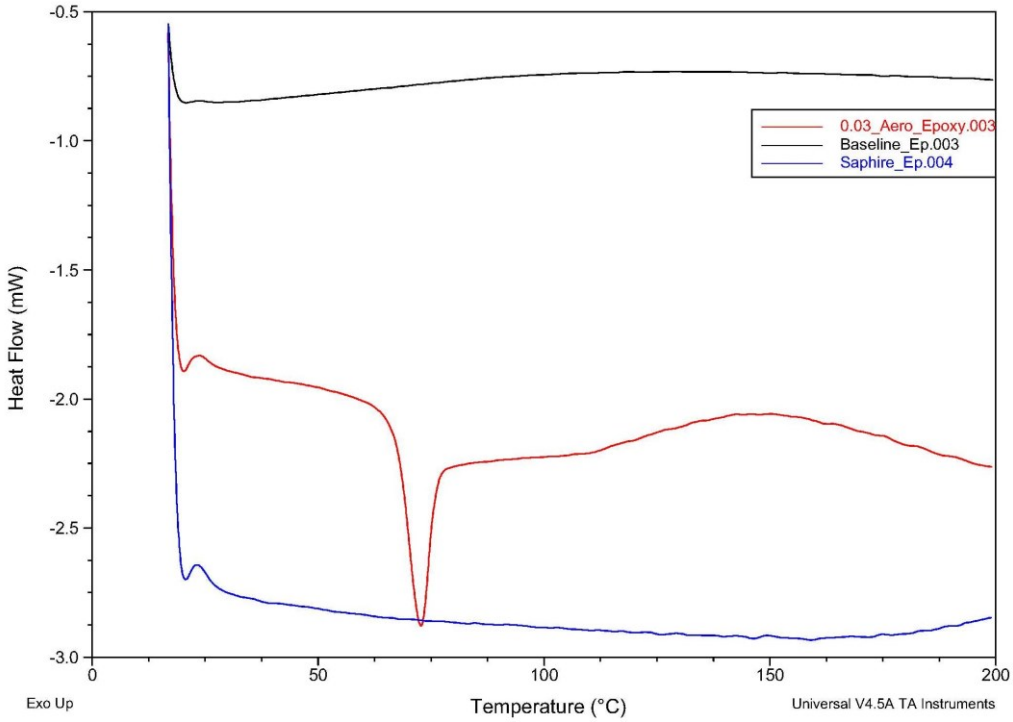

Figure 26 0.03 Aerogel/Epoxy (3P)

The reference values and the procedure used for calculating the specific heat are similar to the method used in the previous section- 4.1.4; the mass of the reference sample was 0.02626 g and the specific heat values of the standard sapphire was taken from [177]. The specific heat capacities of the various batches of the aerogel/epoxy samples at different temperatures are listed in Table 16. It is seen that the specific heats of the composites are greater than that of pure epoxy throughout the whole temperature range. Additionally sample 3P has the highest values throughout the measured range. Finally, all the batches show an increase in specific heat values between 50°C and 100°C due to the glass transition temperature.

Therefore, a mass fraction of 0.03 was adopted for all subsequent samples since the composites did not show any appreciably differences between them during the measurements and a higher mass fraction would theoretically have the lowest thermal conductivity. Additionally, 3 wt% of aerogel in an epoxy changed the resin from a

hydrophilic to a (relatively) hydrophobic material [137]. To try and limit the resin infiltration, a room temperature curing cycle with higher viscosities was also used.

Table 16 Specific heat capacity of epoxy/aerogel samples

Sample	**Mass (g)**	**Temperature (^{0}C)**	**Specific Heat Capacity (J/(g^{0}C))**
P	0.00832	175	1.36
		150	1.18
		100	1.29
		50	0.81
		25	0.67
1P	0.00634	175	2.07
		150	1.84
		100	1.85
		50	1.52
		25	1.38
2P	0.00679	175	1.78
		150	1.64
		100	1.77
		50	1.36
		25	1.31
3P	0.00788	175	2.13
		150	1.96
		100	2.08
		50	1.55
		25	1.43

4.2.2 **Cure Kinetics**

The effects of using the aerogel and the wetting agent on the cure kinetics of the resin system used in the present study are discussed here. The results, along with its inference and discussion, are further published in a journal article by the author [181]. Figure 27 shows the dynamic DSC graphs for the samples in the present study. The samples show an exothermic reaction between ~50^{0}C and ~250^{0}C across all the heating rates studied due to the cure of the resin. Although, individual samples show varying peak heights for different heating rates, the difference between them is small enough to be neglected. Hence, it is believed that the three samples studied have identical behaviour within the heating rates considered.

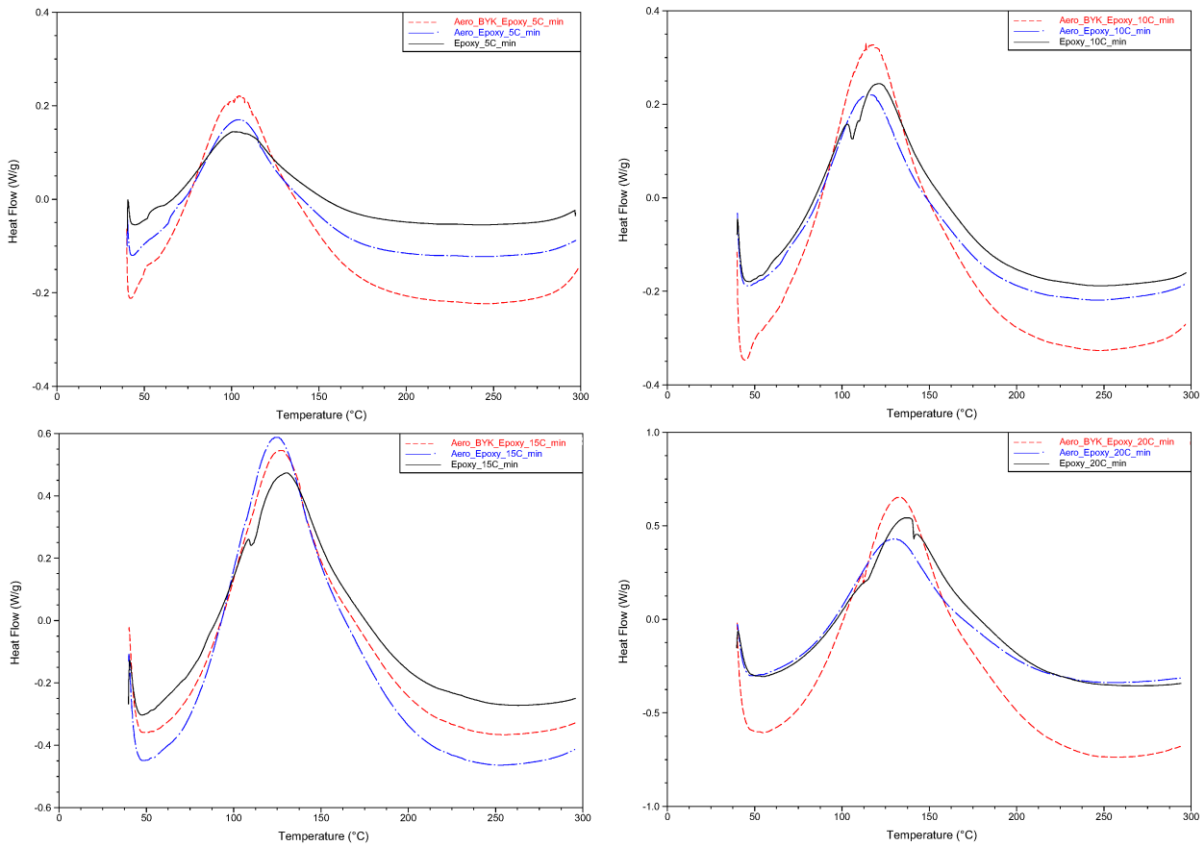

Figure 27 Dynamic runs of the samples in the present study at different heating rates; (Clockwise from the top) 5^{0}C/min, 10^{0}C/min, 20^{0}C/min and 15^{0}C/min

4.2.2.1 Kissinger Energy

This method, described by Kissinger [182], calculates the activation energy and the frequency factor using the peak temperatures (T_p) using Equation 7. The determination of activation energies and frequency factors would allow insight into the effect of aerogel particles on the curing of the epoxy resin.

$$\frac{E_{ak}}{R} = \frac{d\left(ln\frac{\emptyset}{T_p^{\,2}}\right)}{d\left(\frac{1}{T_p}\right)}$$

Equation 7

Where E is the activation energy, R is the universal gas constant, $ø$ is the heating rate and T_p is the temperature at the peak.

The activation energies and the frequency factors for the three batches are calculated using Equation 8 and Equation 9 respectively which are described in the work of Nordeng [183]. The slope and intercept values are obtained from the Kissinger plots (as shown in Figure 28 for batch 3) for the three batches. The curve was fitted using a linear function ('poly1' model name in MATLAB R2015b) and the r^2 values for the three batches are shown in Table 17 wherein, all the values are >0.95.

$$E_{ak} = -(\text{Slope} \times R)$$

Equation 8

$$A = ((e^{\text{Intercept}} \times E_{ak})/R)$$

Equation 9

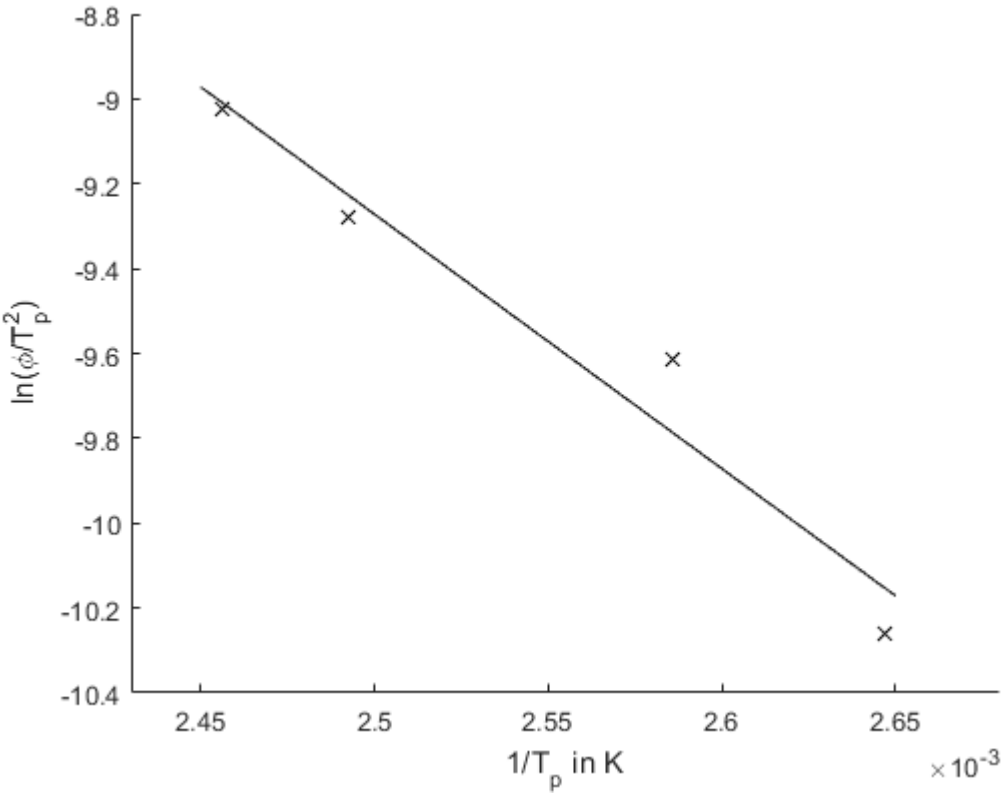

Figure 28 Kissinger plot for Batch

Table 17 Peak model parameters

Batch	Rate	Peak Temperature (^{0}C)	Kissinger Parameters		
			r^2	Activation Energy (E_{ak}) (kJ/mol)	$\ln(A_k)$
Pure Resin (Batch 1)	5	100.95	0.9921	41.49	11.59
	10	121.08			
	15	130.41			
	20	137.57			
Resin + Aerogel (Batch 2)	5	104.19	0.9997	60.03	17.77
	10	116.98			
	15	125.08			
	20	130.42			
Resin + Wetting Agent + Aerogel (Batch 3)	5	104.65	0.9542	51.05	14.82
	10	113.76			
	15	127.67			
	20	134.44			

4.2.2.2 Isoconversional Method

Although the Kissinger method results in a simple calculation of the activation energy and frequency factor using the peak temperatures, it doesn't give further information on the reaction progress. The isoconversional method, on the other hand, allows the calculation of the frequency factors and activation energies at different conversion rates, thereby providing additional information on the reaction kinetics [147].

The degree of conversion/cure (α) is calculated according to the formula in [145] whose simplified version is shown in Equation 10.

$$\alpha = \frac{Q(t)}{Q_T}$$

Equation 10

Where Q_T is the total enthalpy (heat) of the reaction and $Q(t)$ is the cumulative heat of the reaction. Q_T was calculated using the Integrate Peak function and Q(t) was calculated using the Running Integral function, both using the TA Universal Analysis software. It must also be noted that both the values had identical starting and ending points (as shown in Figure 29). The degree of cure (α) as a function of temperature with different heating rates for batch 3 is shown in Figure 30 wherein the temperature at a certain degree of cure increases with the heating rate.

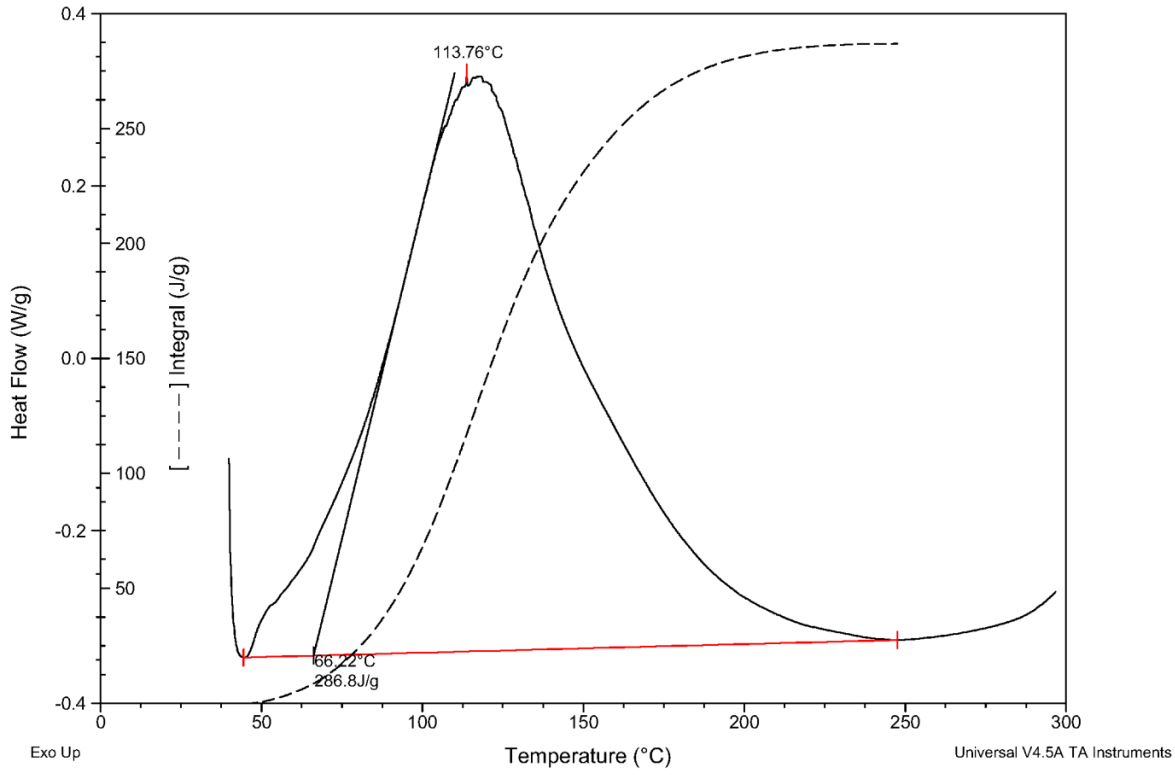

Figure 29 Peak and Running Integral for Batch 3 at 10°C/min

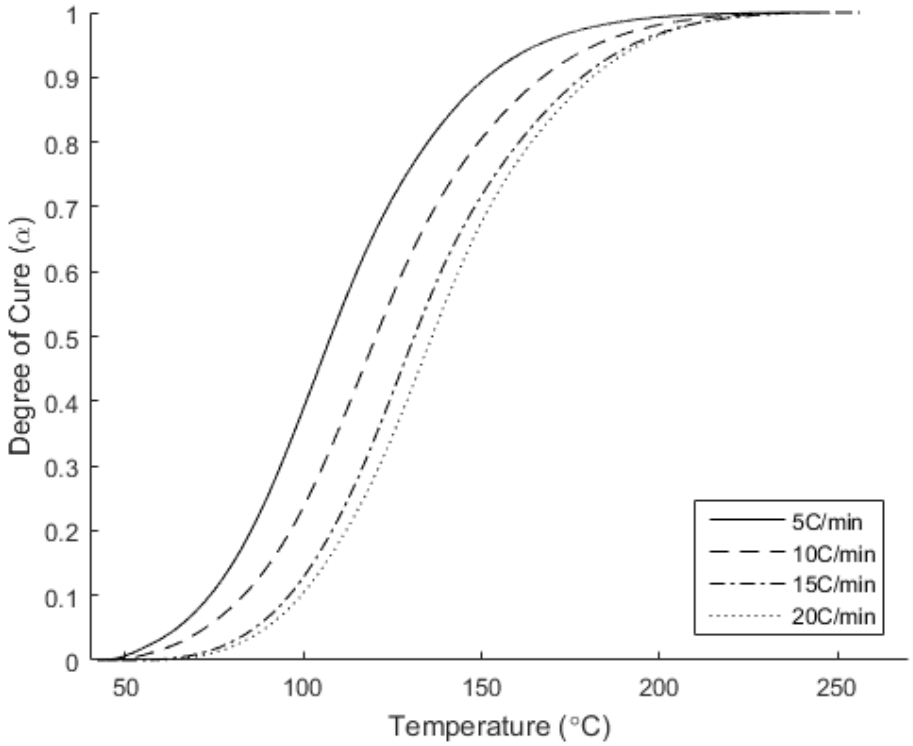

Figure 30 Degree of cure with respect to temperature for different heating rates (Batch 3)

To calculate the activation energy and the frequency factor using the isoconversion method, Equation 11 is followed [145].

$$\frac{d\left(ln\frac{d\alpha}{dt}\right)}{dT^{-1}} = -\frac{E_{ai}}{R}$$

Equation 11

The values of dα/dt were calculated from α and t and, smoothened using the moving average filter in MATLAB before postprocessing. An example of such a signal before and after smoothening is shown in Figure 31 for the 10°C/min run of batch 3.

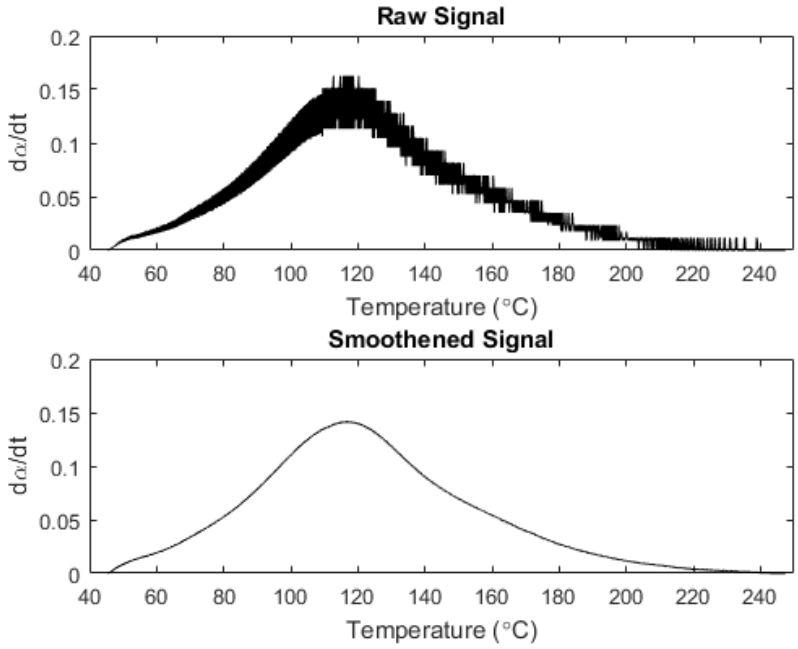

Figure 31 Raw and smoothened signal of dα/dt for batch 3 10^0C/min

Using the smoothened signal plots for Equation 11 were generated; an example of such a plot is shown in Figure 32 for batch 3. The activation energy and the frequency factors are once again calculated using Equation 8 and Equation 9 respectively. The activation energies calculated at various α values for the three batches are tabulated in Table 18. The frequency factors are also similarly shown in Table 19. For both quantities, the values between $0.3>\alpha>0.7$ are shown thereby eliminating the inaccuracies due to peak tails which lead to higher error magnitudes [142]. It must be noted that the r^2 values for all the fits were above 0.98.

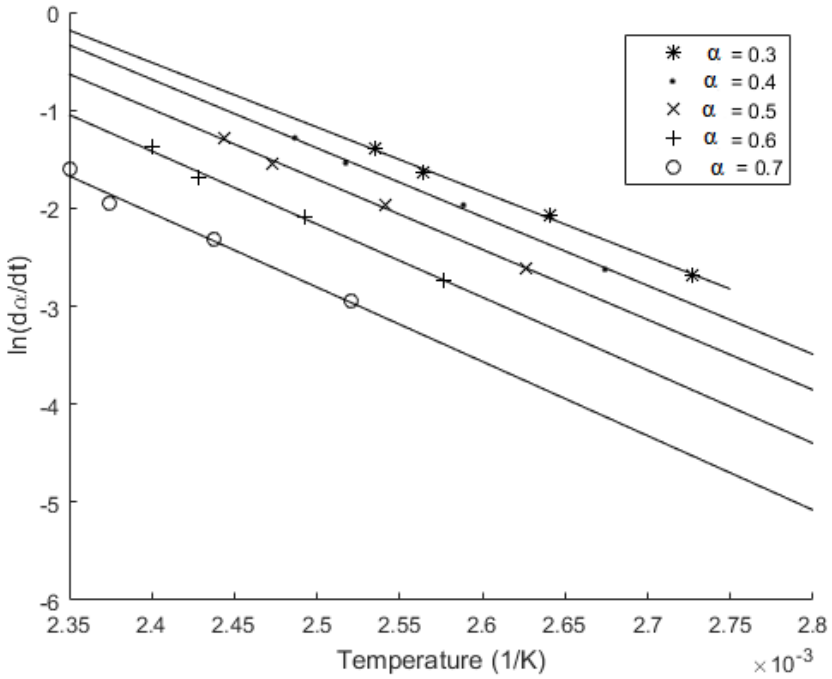

Figure 32 Arrhenius plots for constant degrees of cure (Batch 3)

Table 18 Isoconversion activation energies at various values of α

Conversion	**Activation Energies (E_{ai}) (kJ/mol)**		
	Batch 1	**Batch 2**	**Batch 3**
0.3	50.33	58.67	54.93
0.4	52.65	58.90	58.32
0.5	54.07	58.28	59.56
0.6	53.25	58.65	61.97
0.7	54.08	61.27	62.99
Mean	**52.87**	**59.15**	**59.55**

Table 19 Isoconversion frequency factors at various values of α

Conversion	Frequency factors ($\ln(A_i)$)		
	Batch 1	**Batch 2**	**Batch 3**
0.3	22.48	25.45	24.14
0.4	23.06	25.28	25.01
0.5	23.23	24.76	25.08
0.6	22.56	24.43	25.39
0.7	22.27	24.63	25.06
Mean	**22.72**	**24.91**	**24.93**

4.2.2.3 Autocatalytic Method

Epoxy resins are usually described by either reaction order kinetics or autocatalytic cure [144][145]. However, the curing of epoxy always converts the oxygen in the epoxy ring into a hydroxyl group, which in turn, is also a curing group for the epoxy; thereby showing evidence for an autocatalytic model [147]. Therefore, the two parameter Sestak-Berggren equation (representing an autocatalytic model) was chosen to model the cure kinetics of the three batches in the present study. The equation, introduced by Sestak & Berggren [184], is shown in Equation 12

$$\frac{d\alpha}{dt} = k\alpha^m(1-\alpha)^n$$

Equation 12

To identify *n* and *m* for the different heating rates for each batch, the method outlined in [147], [185] and [186] was utilised wherein, the Generalized Reduced Gradient (GRG) Nonlinear solver in Microsoft Excel 2010 was used to maximise the correlation of the plot between $\ln((d\alpha/dt))/((\alpha^m)*((1-\alpha)^n))$ vs 1000/T by changing the values of *n* and *m*. The values for the 4 heating rates and conversion factors between $0.3 \leq \alpha \leq 0.7$ for an individual batch were populated in a single plot to deduce the

coefficients (as shown in Figure 33). The slope was used to calculate the activation energy (Equation 8) and $\ln(A_{sb})$ was the y-intercept. The values of n, m, activation energies and pre –exponential factors are shown in Table 20. The absolute value of r^2 (Pearson's correlation coefficient) in the table is the value of the maximising objective function whose maximum value was set to 1.

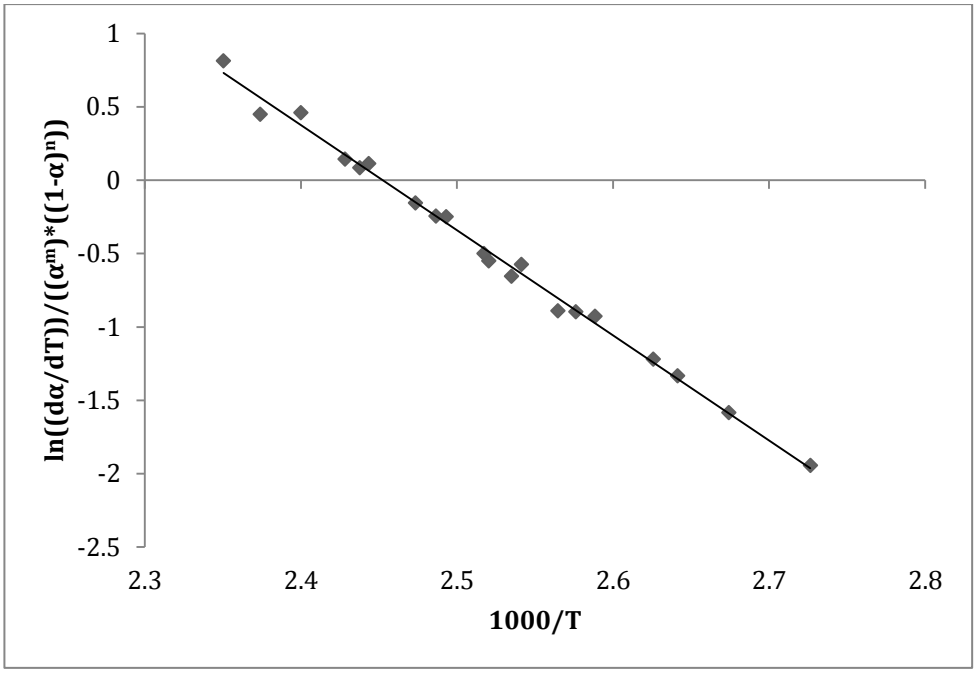

Figure 33 n and m value calculation for batch 3

Table 20 Model parameters

Batch	**n**	**m**	**E_{asb} (kJ/mol)**	**$\ln(A_{sb})$ (min^{-1})**	**R^2**
1	1.86	0.16	53.04	15.51	0.997
2	1.98	0.03	59.45	17.61	0.997
3	1.99	0.03	59.54	17.56	0.997

The model was simulated using Equation 13 wherein the values for A_{sb}, E_{asb}, m and n are obtained from Table 20 for each batch.

$$\frac{d\alpha}{dt} = A_{sb}\{e^{-E_{asb}/RT} * \alpha^m[(1-\alpha)^n]\}$$

Equation 13

The results are shown and compared with the experimental data for batches 1, 2 and 3 in Figure 34, Figure 35 and Figure 36 respectively to determine the accuracy of the chosen model and its parameter (an example of the comparison code is given in APPENDIX II). For the sake of clarity, the smoothened dα/dt values were used as the experimental data. Although a good fit between the model and the experiment is observed, there is some deviation at higher temperatures which in turn, represent higher α values. This is due to the selection of α between 0.3 and 0.7 for the model parameterisation as discussed in the previous section. Nevertheless, it is believed that the truncated Sestak-Berggren model [184] using the parameters identified in Table 20 can adequately model the cure kinetics of the materials in the present study especially, in the mid cure range.

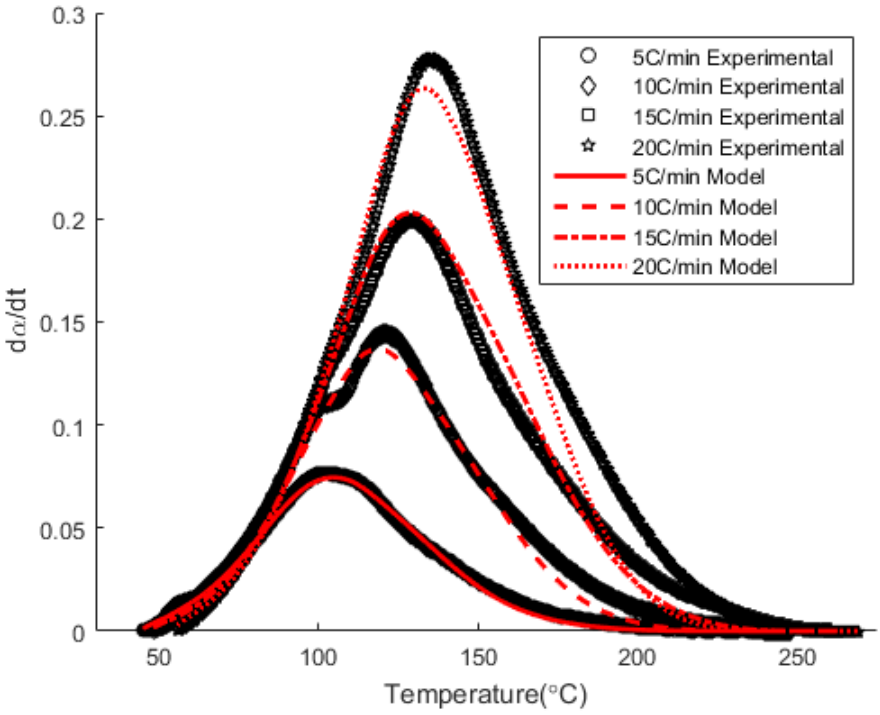

Figure 34 Comparison of model and experimental data for Batch 1

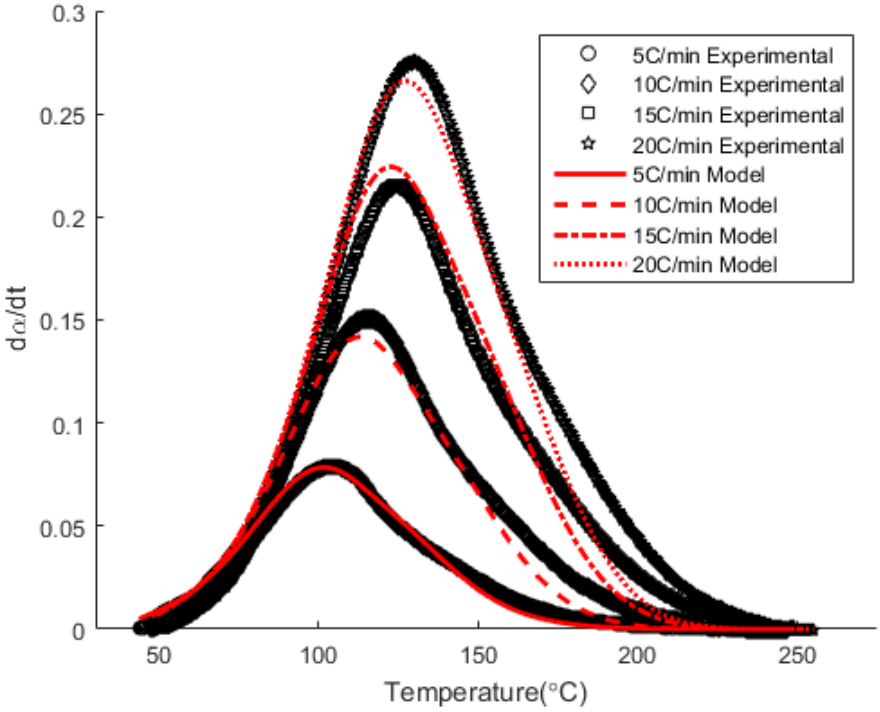

Figure 35 Comparison of model and experimental data for Batch 2

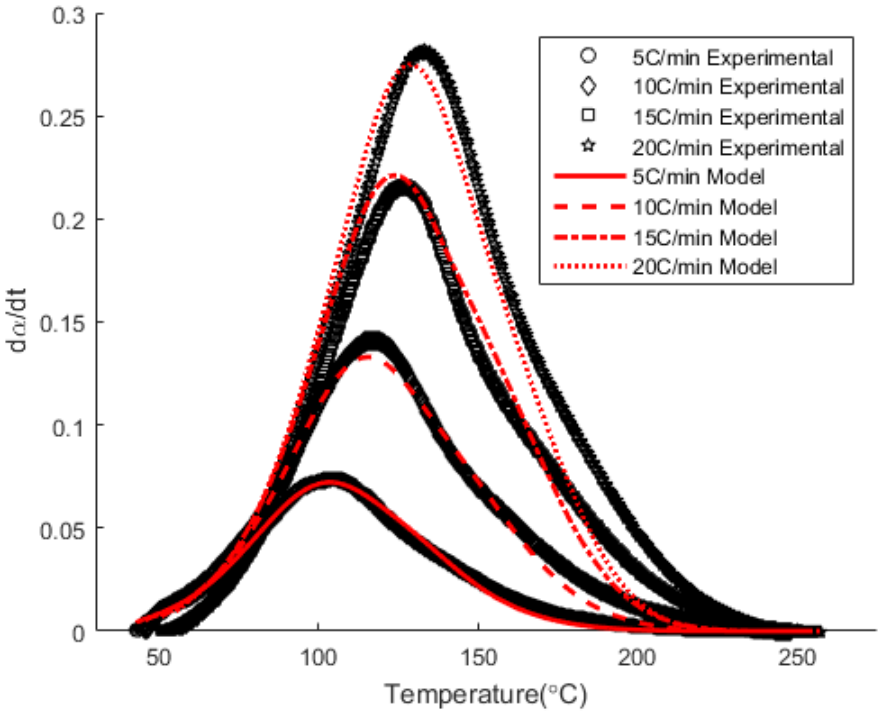

Figure 36 Comparison of model and experimental data for Batch 3

4.2.2.4 Comparison of the methods

Table 21 shows the activation energies and the frequency/pre-exponential factors determined by the various methods used in the present study. It must be noted that the value used for the isoconversional method for each batch was the average in the interval $0.3 \leq \alpha \leq 0.7$ and the frequency factors for the Sestak-Berggren model were calculated using Equation 9. When comparing the individual results for each method, it is seen that the activation energy of batch 1 (pure resin) is consistently lower than batches 2 and 3 which contain aerogel. This could be explained by the lower viscosity of the pure resin (due to the absence of aerogel particles) which has a lower activation energy [147]. When comparing the results of batch 2 with batch 3, the activation energy determined by the isoconversional method and the Sestak-Berggren model are similar. The Kissinger method, on the other hand, shows a much greater difference particularly for batches 1 and 3. However, the results from the former methods are preferred since they consider more of the cure reaction as compared to only peak

parameters in the Kissinger method and hence, more accurate. Finally because the addition of a wetting agent into the aerogel/epoxy composite has a minimal effect on the cure kinetics of the resin, its use is recommended due to its influence on the interface of the aerogel and the resin. It is thought that the wetting agent would increase the strength at the boundary and hence, positively influence the mechanical properties of the composite.

Table 21 Comparison of the parameters from the different methods used in the study; 1-Kissinger Method, 2-Isoconversion method, 3- Sestak-Berggren model

Parameter	**Batch 1**			**Batch 2**			**Batch 3**		
	1	**2**	**3**	**1**	**2**	**3**	**1**	**2**	**3**
Activation Energy (E_a) (kJ/mol)	41.49	52.87	53.04	60.03	59.15	59.45	51.05	59.55	59.54
Frequency Factor (lnA)	11.59	22.72	24.27	17.77	24.91	26.48	14.82	24.93	26.44

4.2.3 **Characterisation**

This section presents the final set of experimental results for the aerogel/epoxy composites building on the data and knowledge gained from the previous sections. Here, the processing parameters for the composites such as the time of aerogel addition are finalised through the use of microscopes and a spectrophotometer. Then, the thermal conductivity of the final material is measured to quantify the gain in thermal insulation performance.

As discussed in the previous chapter, the three batches (A- pure resin, B- aerogel/epoxy and C- aerogel/epoxy/wetting agent) are each divided based on the

time of aerogel addition- 0.5, 1 and 1.5 hours. Once again, these results and their inference are also published by the author in [187].

4.2.3.1 Optical Microscope

The optical image of sample 0.5B in Figure 37 shows particles that are around 500 μm in size and almost spherical in nature. These are believed to be the aerogel particles in the resin since the aerogel powder used in the present study are between 100-700 μm in size [179]. However owing to the resin surrounding the particles, the ability to see within the structure and to predict the amount of infiltration is not possible with the current method. Nevertheless, the results do show the distribution of aggregated silica/aerogel particles which could potentially signify the presence of aerogel with limited infiltration. Additionally, Figure 37c shows smaller circular features, which are thought to be the air pores, formed during the processing of the composite material.

When comparing the results of the different batches, it was seen that similar aerogel-like structures were also found in samples 1B and 1.5B as shown in Figure 38 and Figure 39 respectively, indicating the possible existence of aerogel particles in all samples. However, when considering sample 1.5B the existence of pronounced darker and lighter areas were seen (Figure 39c) which could be due to the lower flow rate of the resin which is more cured at this stage. High viscosity is expected to adversely affect the final composite material because of loss in mouldability and the application of more force needed to mix, which could destroy the fragile aerogel. This destruction is potentially seen in Figure 39b where the aerogel structures do not have smooth and clear boundaries. Although sample 1B also shows similar breakage of the aerogel, the boundaries are better defined compared to sample 1.5B as seen in Figure 38a and c.

Therefore, while sample 0.5B showed a much better retention of the overall structure of the aerogel, the lower viscosity of the resin during the aerogel addition could potentially result in a higher infiltration of the former into the latter. On the other hand, sample 1.5B showed much higher viscosity which would result in greater difficulties whilst moulding complex shapes and could break the aerogel during the mixing process. Hence, the addition of the aerogel at around the 1 hour mark is recommended; wherein sample 1B shows limited breakage as compared to sample 1.5B and the higher viscosity would result in a lower infiltration of the resin compared to sample 0.5B.

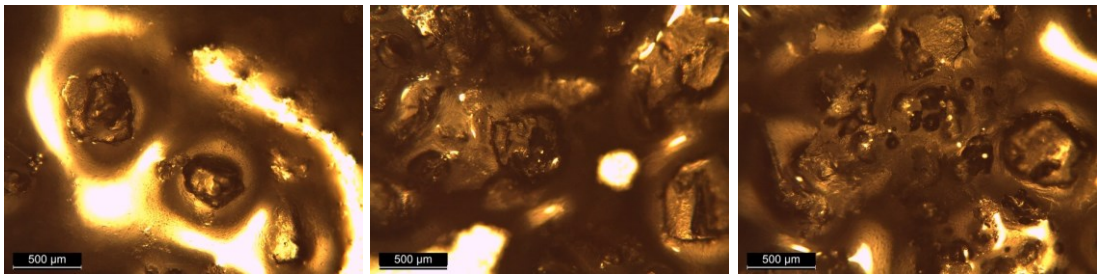

a b c

Figure 37 Optical images of sample 0.5B. The presence of aerogel particles is seen in these images particularly in image (a). However as discussed in the text, it is not possible to see within the structure to accurately predict the amount of infiltration.

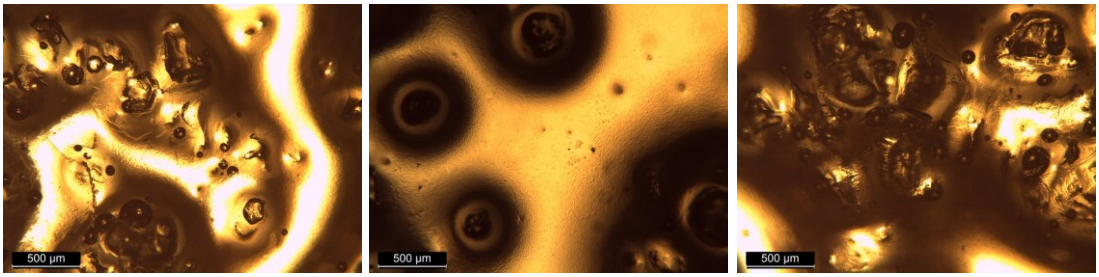

a b c

Figure 38 Optical images of sample 1B. Although the images for this sample show some breakage of the aerogel particles, their general shape and boundaries are still observed.

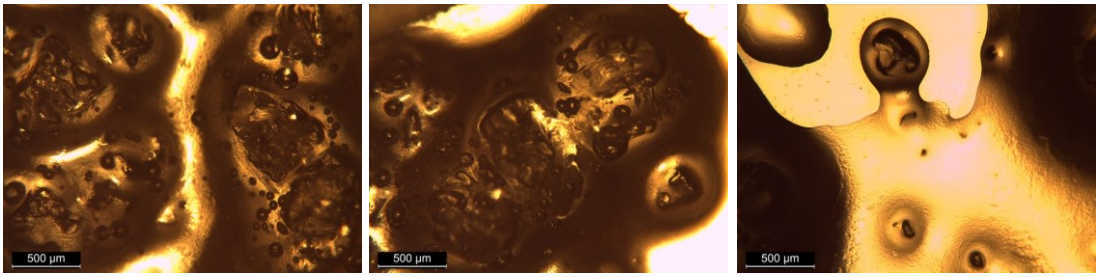

a b c

Figure 39 Optical images of sample 1.5B. The destruction of the aerogel particles can be potentially seen in these figures. This is thought to be due to the increased viscosity of the curing resin at this stage.

Microscopic images obtained for batch C are shown in Figure 40, Figure 41 and Figure 42 for 0.5C, 1C and 1.5C respectively. Similar to batch B, sample 0.5C shows a more holistic aerogel structure compared to sample 1.5C whose destruction can be seen, especially in Figure 42b. But the lower viscosity of the resin in the 0.5C sample would result in higher rates of infiltration. Hence, it is once again suggested that the aerogel/epoxy composites must balance the ability to mould complex shapes and potential mechanical destruction of the aerogel with the infiltration of the resin. Therefore, the addition of the former must be in-between the two extremes at around the 1 hour mark as the images for sample 1C (Figure 41) do not show similar levels of destruction as compared to sample 1.5C and the higher viscosity of the curing resin at

this stage would ensure a lower level of resin infiltration into the aerogel compared to sample 0.5C.

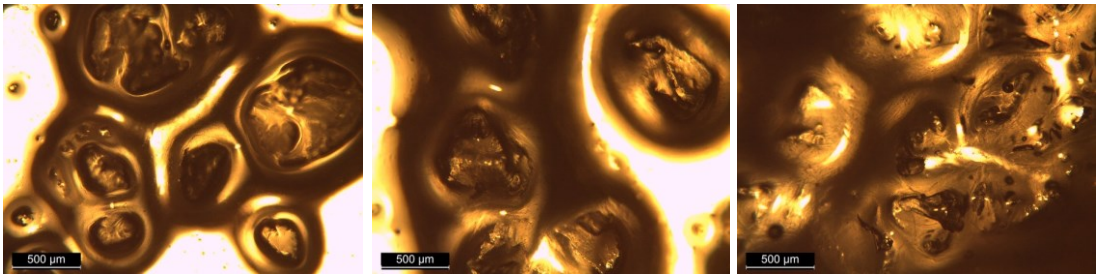

a b c

Figure 40 Optical images of sample 0.5C. Similar to batch B, the aerogel particles can be observed in these samples. But the lower viscosity of the curing resin would suggest higher infiltration rates into the aerogel particles.

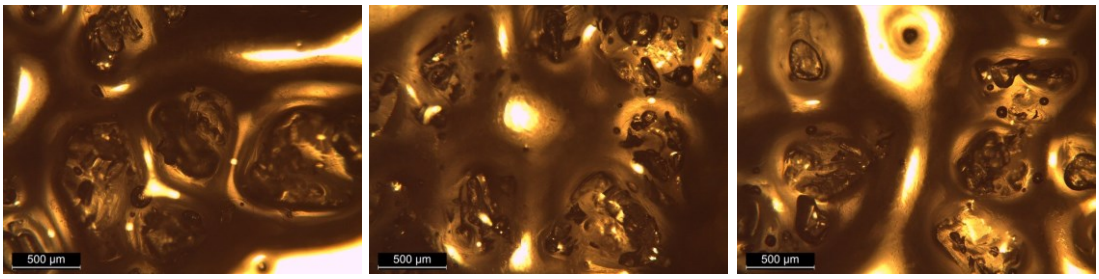

a b c

Figure 41 Optical images of sample 1C. The material is similar to sample 0.5C however the resin infiltration into the aerogel structure is excepted to be lower due to the higher viscosity of the resin at this stage of the cure.

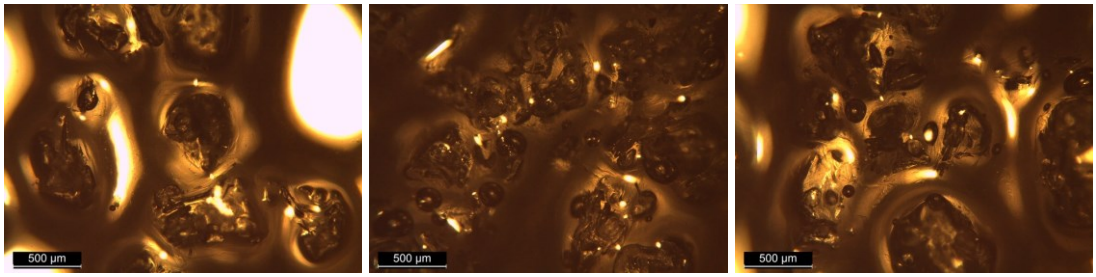

a b c

Figure 42 Optical images of sample 1.5C. As noticed in its counterpart of batch B, this samples also shows the destruction of the aerogel particles. Because of the resin's high viscosity at this stage, moulding and shaping complex designs would be more difficult for this material.

4.2.3.2 Scanning Electron Microscope

EDX linescans showing the elemental composition across a line drawn through an ESEM image for batch B are illustrated in Figure 43. It must be noted that only the information (EDX) for carbon (C) and silicon (Si) are shown and compared for simplicity's sake.

Figure 43a shows the linescan across an aerogel particle in sample 0.5B. The EDX analysis indicates the presence of silica in the particle thereby confirming the existence of aerogel. The graph pertaining to carbon (C) shows its presence in the particle as well suggesting the infiltration of resin into the aerogel. Figure 44 also shows that the aerogel particles (spectrum 7 and 8) have a higher weight percentage of Si compared to the matrix (spectrum 9). However, all three spectrums show high levels of C providing further evidence for resin infiltration into the aerogel particles.

Additionally, Figure 44 shows regions of high Si content (spectrum 6 and 10) which are lighter in colour compared to the surrounding areas. These areas are believed to be regions of low resin content as reflected by the weigh percentage of C. The spectrums here could be that of the glass slide since these regions also show a higher presence of sodium (Na), magnesium (Mg), potassium (K) and calcium (Ca). One explanation for

this could be due to the sample being held vertically in the spectrophotometer wherein, the downward movement of the resin could have left certain areas with lower amounts of the material and hence, the EDX would have picked up the composition of the glass substrate instead. A similar area is also observed on the right side of Figure 43a (~1600 μm) with higher Si content.

Figure 43b shows the linescan of an aerogel particle in sample 1B. The distribution of silicon (Si) is similar to sample 0.5B (Figure 43a). Whilst analysing the distribution of carbon (C), it was observed that there is a decrease in its content (circled in the image) through the particle for sample 1B. However, this 'well-type' distribution is not clearly visible in sample 0.5B thereby suggesting a lower level of resin infusion for sample 1B. Additionally, a spectrum map of sample 1B shown in Figure 45 depicts increased levels of Si accompanied by lower levels of C for the aerogel particles.

The linescan for sample 1.5B is presented in Figure 43c in which coalesced particles are observed. As evidence from the image, these particles contain Si thereby providing evidence to the claim that these are broken aerogel/silica particles. These are thought to be due to the mechanical destruction of the aerogel during mixing (as discussed in the previous section) because of the particles' smaller size when compared to an undamaged aerogel particle.

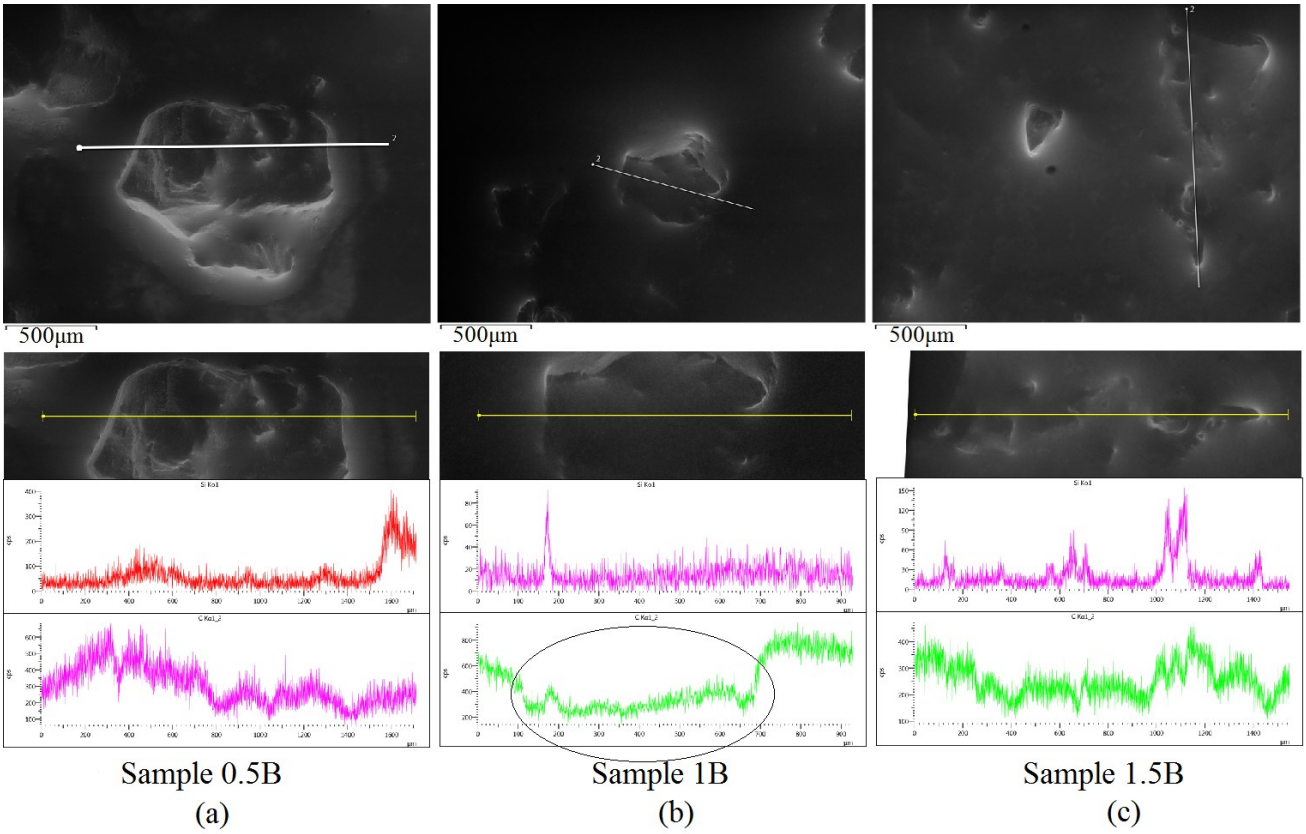

Figure 43 Line scans of samples in batch B with the well-like distribution of sample 1B circled in the graph; the top spectrum represents silicon (Si) and the bottom spectrum represents carbon (C)

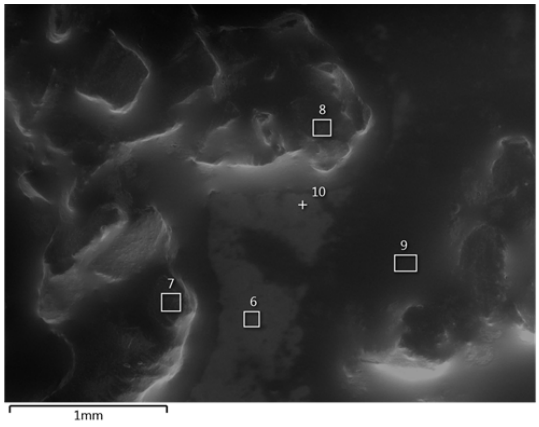

	Glass	Aerogel Particles		Matrix	Glass
Spectrum Label	Spectrum 6	Spectrum 7	Spectrum 8	Spectrum 9	Spectrum 10
C	31.1	70.48	74.99	75.11	54.92
O	34.58	21.85	20.2	22.39	25.23
Na	6.14	0.89	0.45	0.39	2.64
Mg	1.59				0.8
Al	0.42				
Si	22.33	5.79	3.28	1.27	11.45
Cl	0.16	0.58	0.82	0.69	0.45
K	0.52				0.58
Ca	3.17	0.42	0.25	0.16	3.94
Total	100	100	100	100	100

Figure 44 EDX analysis of Sample 0.5B (the elemental composition in the spectra are given in terms of weight percent)

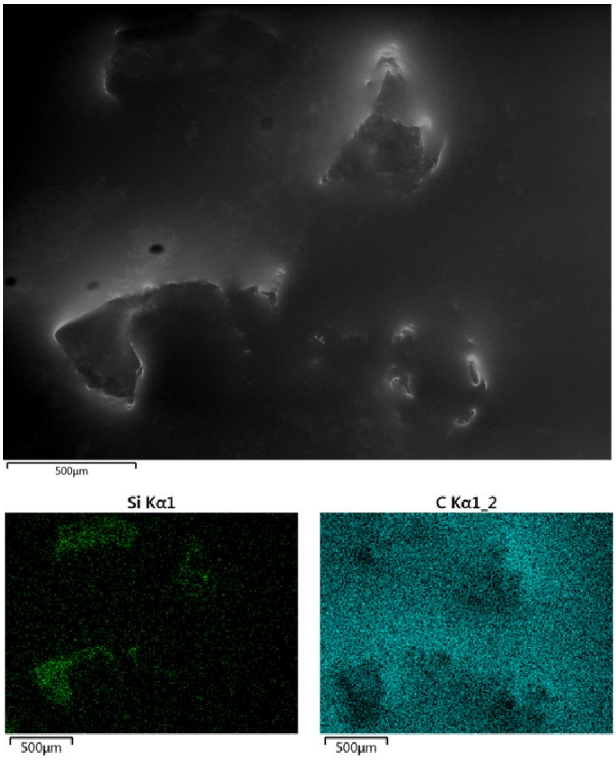

Figure 45 Spectrum map of sample 1B

Figure 46a shows the EDX linescan of an aerogel particle in sample 0.5C wherein, silicon (representing silica) is detected. However, similar to sample 0.5B, the scan representing carbon shows small variances across the scanned range, suggesting an infiltration of the resin into the aerogel. This is further proven by Figure 47 wherein, spectrums 1, 4 and 5 within the particle not only show the existence Si, but the percentage of C does not decrease when compared to the matrix (spectrums 2 and 3).

When considering the EDX results of sample 1B (Figure 46b) it is observed that the linescan across an aerogel particle shows a decrease in carbon (C) along with an increase in silicon (Si). Once again, a well-like distribution of carbon (circled in the figure) is observed across the aerogel particle suggesting the presence of aerogel particles with decreased resin infiltration as compared to sample 0.5C. To further illustrate, an EDX spectrum map of sample 1C is presented in Figure 48. It is seen that, similar to Figure 45 for sample 1B, the position of the aerogel particles is

represented by lower carbon and higher silicon content compared to the neighbouring matrix.

Finally, the results of sample 1.5C also show a decrease in the level of carbon (C) within the aerogel particle (Figure 46c) similar to sample 1C with a well-like distribution. However, as illustrated in Figure 49, the particles in the sample show signs of mechanical destruction i.e. the aerogel has not been able to retain its integrity perhaps due to the increased viscosity of the resin.

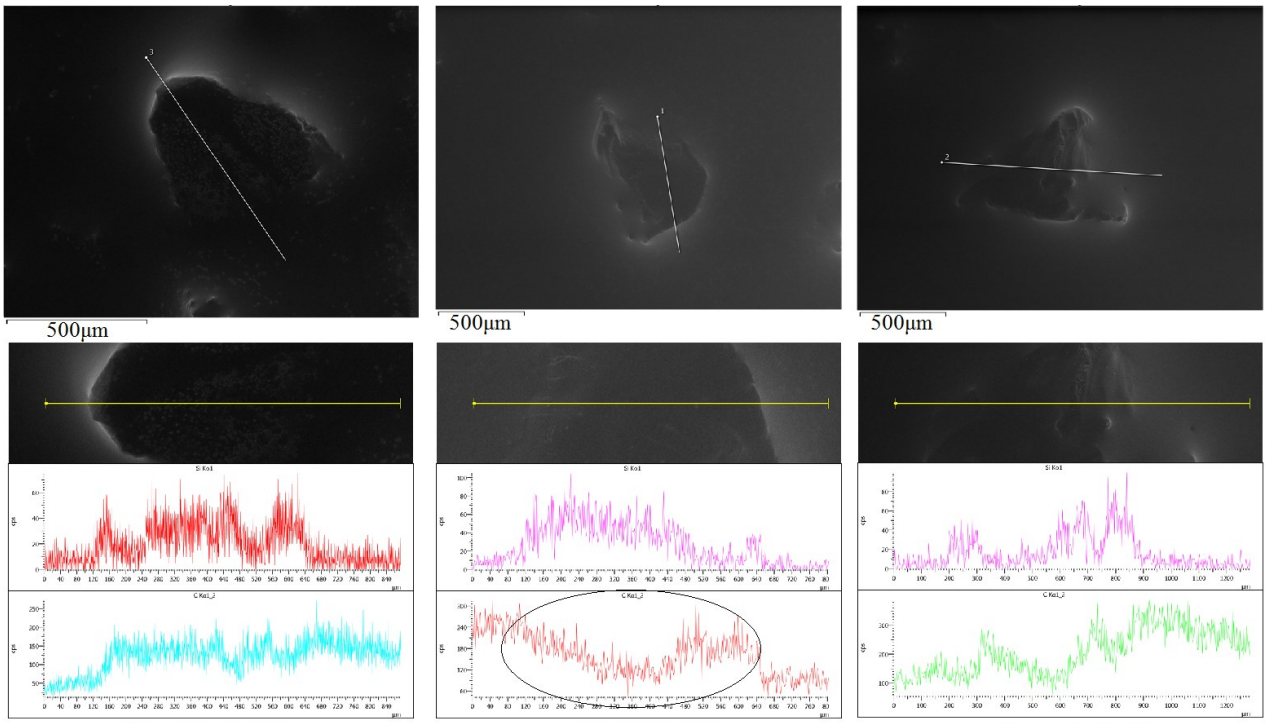

Figure 46 Line scans of samples in batch C with the well-like distribution of sample 1C circled in the graph; the top spectrum represents silicon (Si) and the bottom spectrum represents carbon (C)

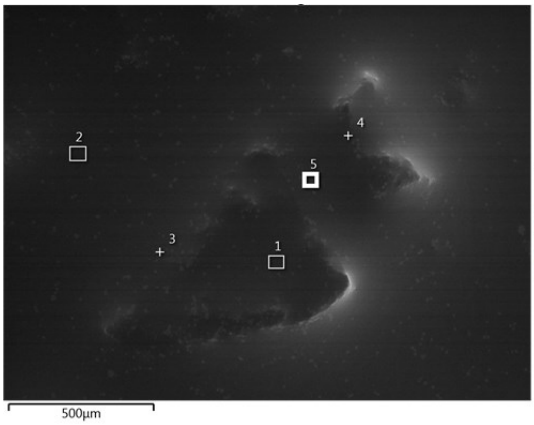

Spectrum Label	Spectrum 1	Spectrum 2	Spectrum 3	Spectrum 4	Spectrum 5
C	79.37	79.69	80.76	80.68	80
O	19.03	18.99	17.11	17.11	18.56
Si	0.24			1.01	0.26
Cl	1.36	1.32	2.13	1.19	1.18
Total	100	100	100	100	100

Figure 47 EDX analysis of Sample 0.5C (the elemental composition in the spectra are given in terms of weight percent)

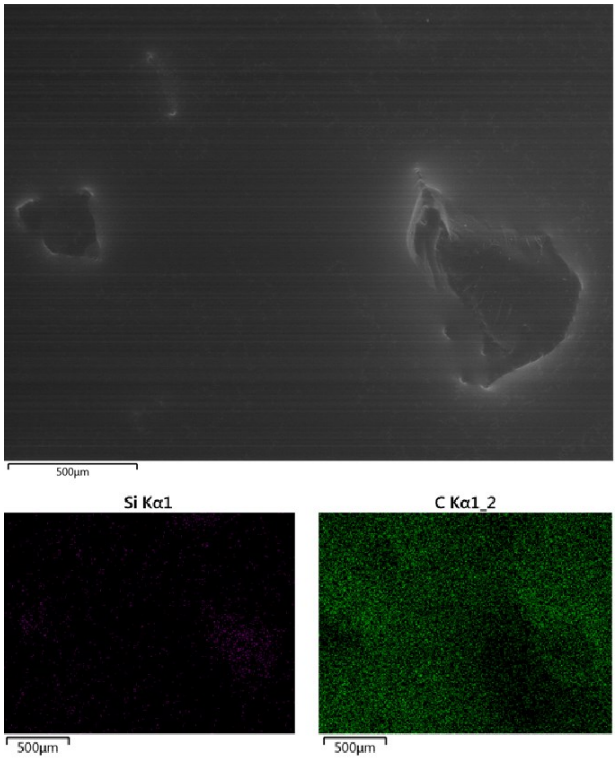

Figure 48 Spectrum map of sample 1C

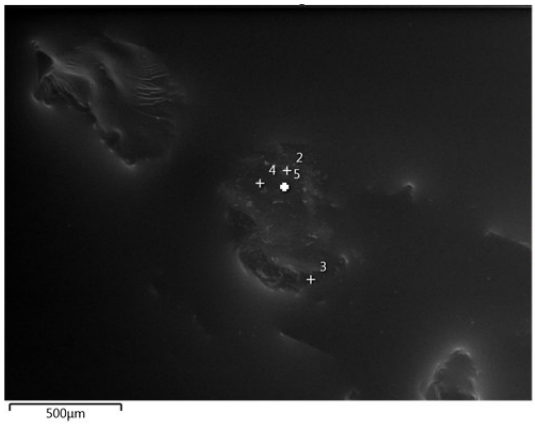

Spectrum Label	Spectrum 2	Spectrum 3	Spectrum 4	Spectrum 5
C	75.36	76.98	72.52	70.69
O	20.05	20.95	22.46	23.42
Si	3.9	1.27	4.19	5.17
Cl	0.69	0.8	0.84	0.72
Total	100	100	100	100

Figure 49 EDX analysis of Sample 1.5C (the elemental composition in the spectra are given in terms of weight percent)

4.2.3.3 Optical transmittance and scattering characteristics

As described previously, each of the three batches is further divided into 3 samples depending on the time of aerogel addition i.e., 0.5 hours, 1 hour and 1.5 hours. Additionally, each sample was subjected to 6 runs in the spectrophotometer at 5 minute intervals as shown in Table 22. The results for the aerogel-epoxy samples (batches B and C) at the 1 and the 1.5 hour mark are shown in Figure 50 and Figure 51 respectively. It was observed that the transmittance value for sample 1A increased from 79.6% to 85.8% at 665 nm from run 1 to run 6. However, the transmittance for the aerogel/epoxy composites had decreased for the samples 1B and 1C showing a change in value from 25.9% (run 1) to 16.6% (run 6) and 28.3% (run 1) to 21.1% (run 6) respectively at 665 nm. The 1.5 hour aerogel samples show similar trends to the 1 hour samples; sample 1.5A exhibits an increase in the transmittance values from 73.3% at run 1 to 80.7% at run 6. However, the values for the composite samples remained relatively constant with a minimal drop from 10.4% (run 1) to 9.9% (run 6) in sample 1.5B and 37.2% (run 1) to 35.8% (run 6) in sample 1.5C. Figure 50 also shows a part of the graph generated by sample 1C between 665nm and 1200nm which is zoomed in for a better illustration between the runs. Although, the transmittance is

only derived at a single wavelength (665 nm), the difference between the initial and final run over the whole range is illustrated in Figure 52 for batch C i.e., samples 1C and 1.5C.

Table 22 Time of transmittance measurement for all batches

Run	Time of measurement (mins)
1	0
2	5
3	10
4	15
5	20
6	25

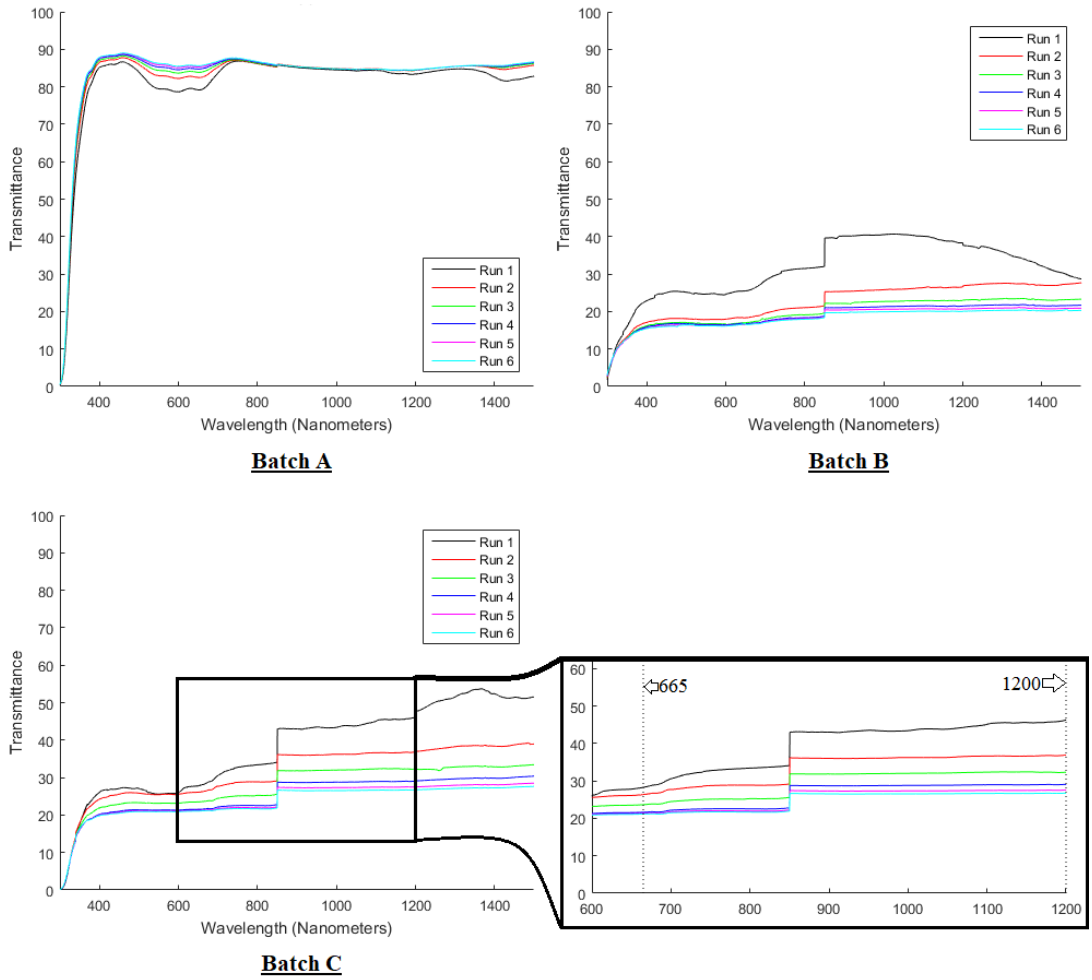

Figure 50 Transmittance of test samples, A, B and C at 1 hour. For sample 1C, a section is highlighted for comparison of various test run.

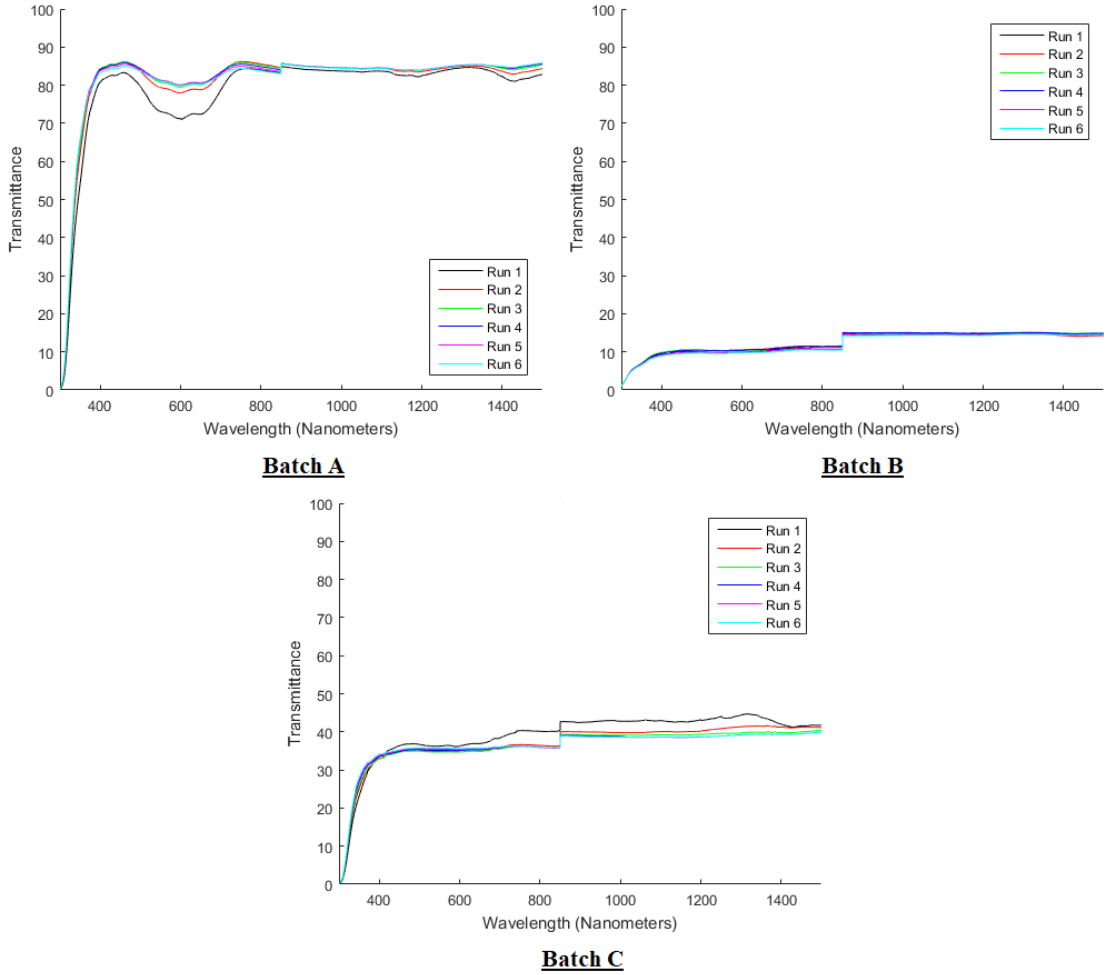

Figure 51 Transmittance of test samples, A, B and C at 1.5 hours

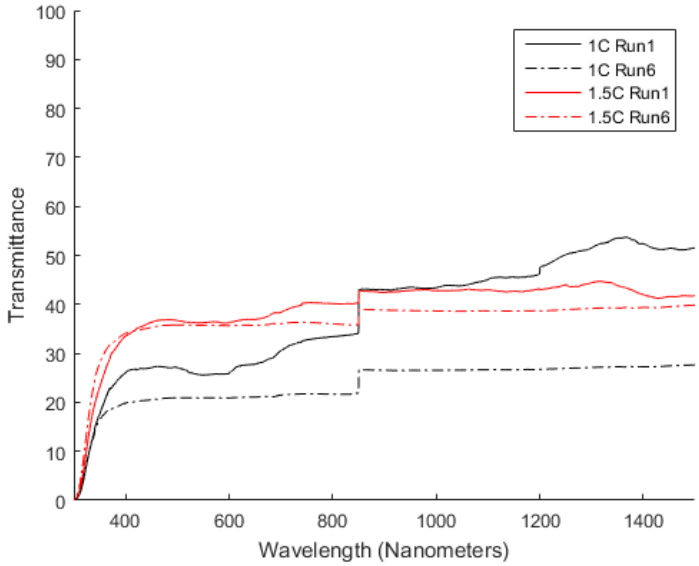

Figure 52 Comparison of the spectrophotometer results for samples 1C and 1.5C. For clarity only the initial (Run 1) and final (Run 6) runs are shown

Since a sharp decrease in the transmission between the epoxy resin and the aerogel/epoxy composite is observed, the total reflectance of the three batches was measured using an integrating sphere. Samples 1B and 1C were chosen since they are the most promising candidates to retain the aerogel structure and enable the production of complex shapes. The transparent resin-hardener sample whose refractive index of ~1.5 [188] is expected to exhibit a similar nature of diffuse reflectance obtained from a glass slide which has an index of 1.52. Here, the glass slide (typically, 8% reflectance) and S-1A are used as reference to study the nature of scattering. Figure 53 shows that all four samples have similar reflectance performance in the measured range of 400nm to 1500nm. The results demonstrate that all samples had negligible differences in scattering from the surface. However, the nature of scattering below 350nm is different for each sample with an increase from 8% to approximately 20% for all samples with the exception of the glass slide. As shown in Table 23, the absorption value (calculated by subtracting the value of transmittance and reflectance with 100) of sample 1A is low; 6.4% at 665nm and is mostly

transparent over visible and NIR bands. The absorption in samples B and C are 75.4% and 70.9% respectively at 665nm which are very high due to the particulate nature of aerogel and film thickness. The lower value of transmittance in samples B and C could be attributed to the opaque nature of the final solution following chemical mixing and curing since the aerogel has a complex nature of refractive index. The real part of the index is 1.02 [189] which is close to air, but it is believed that the imaginary index e.g., absorption coefficient plays a dominant role in the spectral performance thereby resulting in a lower transmittance [190]. It must be noted that although the transmission readings were taken during the cure of the resin (run 6), it is believed that the transmission characteristics of the epoxy resin after cure do not change appreciably as reported in [191]. Hence, the spectral transmission of sample A should remain constant as shown in Figure 50, and therefore, was used for comparative study in Table 23.

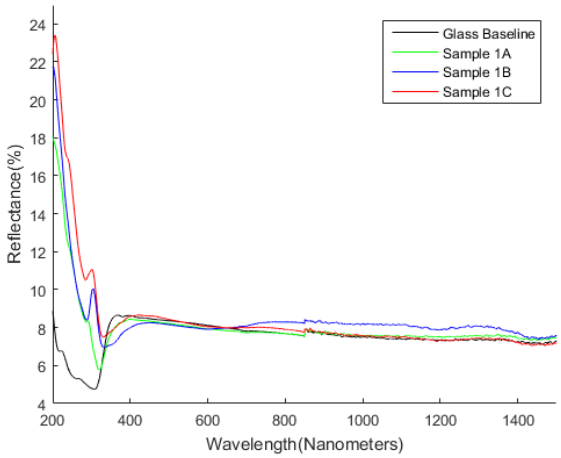

Figure 53 Reflection characteristics of Samples 1A, 1B and 1C. A plot of the glass slide is also given to establish a baseline

Table 23 Spectral characteristics of samples 1A, 1B and 1C (at 665 nm)

Sample	Transmission	Reflection	Absorption
1A	85.8	7.8	6.4
1B	16.6	8.0	75.4
1C	21.1	8.0	70.9

An increase in the reflectance at wavelengths below 350nm for samples A, B and C in Figure 53 could be associated with resin's intrinsic properties. To further understand this occurrence, the scattering performance of the various samples of batch C is compared with a resin sample-1A in the wavelength range of 200-350nm as shown in Figure 54. It is observed that the aerogel composite samples, 1C and 1.5C, show a sharper and a more distinctive peak as compared to the pure resin sample. Since the film thickness is not monitored precisely, the nature of plots cannot be quantitatively explained in this study. However, the presence of sharper peaks can be qualitatively described as arising from the presence of aerogel particulates in the samples since a similar peak below 250 nm is also seen in the work of Fernandes et al. [192] for the aerogel samples. Therefore, it is suggested that the sharper peaks of the composite samples in the present study indicate the existence of aerogel within the material at the end of the curing cycle. It is also seen that sample 0.5C does not show the same level of prominence and its value (8%) is similar to glass. This could be due to the low viscosity of the resin at the early stage of curing which would have resulted in its greater flow over the glass. The thinner layer of the sample would have caused the instrument to pick up the properties of the glass rather than the sample during the measurement.

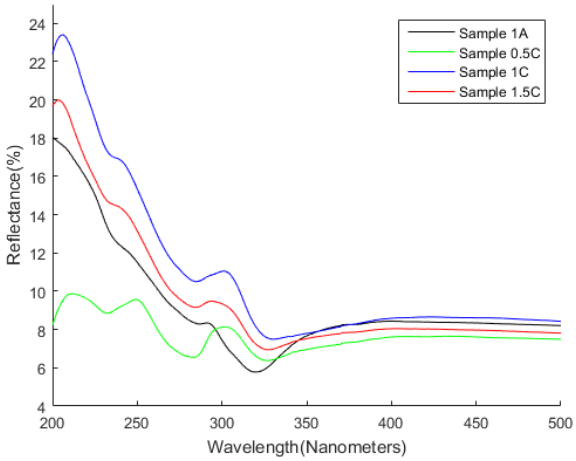

Figure 54 Reflection characteristics of Samples 0.5A, 0.5C, 1C and 1.5C

The analysis of the curing curves in Figure 50 and Figure 51 indicates two possible reasons for the difference in the results of each run for a particular sample. One explanation could be the downward movement of the resin during the measurements which would result in an increased transmission value due to the reduction of the resin thickness as time (and hence, the run number) progresses. This effect is seen in the samples of batch A, where an increase in the transmittance is seen with the number of runs with run 1 showing the lowest transmittance values for each sample. Additionally, the spacing between the graphs at higher run counts is smaller than at lower run counts; this provides further evidence for the downward flow of the resin since most of the liquid flow occurs initially and as time progress the film becomes more stable and hence less movement, resulting in a smaller distance between the graphs of each run. The difference in the graphs of the composite materials could be explained by the change in the density of aerogel due to the infiltration of the resin, which in turn would affect its refractive index [189] and hence the transmittance. Although, there is still a downward motion of the resin in these composites, it is thought the increased viscosity of these samples would limit this movement. In fact, the resin infiltration into the aerogel particle has a greater effect on the transmission

properties because of the reduction in the transmission, as opposed to the increased values (seen in batch A) with each run. However, if the flow of the resin during the experiment could be assumed to be mainly due to its viscosity which, would be valid in the present case due to the restriction of the resin to an almost 1D flow, it could be assumed that the rate of infiltration is proportional to the rate of flow into the periphery of the aerogel and hence any change in the graph is due to the flow of the resin.

The results for the samples at 1 hour (Figure 50) and 1.5 hours (Figure 51) show some variations when comparing similar batches across the two times. The results at 1 hour for the composites show a difference in the transmittance between the runs especially the first 3 runs after which, the material starts to stabilise. The difference could be primarily influenced by the resin infiltration into the aerogel particle which in turn is affected by the resin flow hence; most of the change happens initially corroborating the earlier results of batch A. This also suggests that the resin is still able to flow easily at this stage of the cure and the lower viscosity would enable the formation of more complex shapes and less force to stir the aerogel particles in. The results for the composite batches at 1.5 hours show almost identical values of transmission for each run. This is thought to be due to the limited resin flow which would reduce the infiltration as well as the mouldability of the sample. Therefore, it is believed that for both batches of aerogel/epoxy composites at 1.5 hours, the viscosity would be high for moulding in commercial applications and as mentioned previously, could result in an increased force during mixing that may destroy the aerogel. The batches B and C show similar results with a slightly increased flow in batch C due to the presence of the wetting agent which would contribute to a decrease in the viscosity of the resin.

Nevertheless, this difference is small enough to be neglected and the use of a wetting agent in the manufacturing process is recommended.

4.2.3.4 Thermal Conductivity

As observed, the addition of aerogel particles at the 1 hour mark show the most promise and the introduction of the wetting agent had little/no effect on the results. Therefore, the thermal conductivity for samples 1C along with the pure resin (sample 1P) were determined and presented in Table 24. 2 plates of 1C (1C and 1Cb) along with a plate of 1P were cut to a size of 30*30*4 (mm) from a plaque of the material for measurements. The results are the average of 10 measurements per plate along with the minimum and the maximum value for each sample.

Table 24 Thermal conductivity values

Sample	**Thermal Conductivity (W/(m*K))**		
	Average	**Maximum**	**Minimum**
1P	0.2309	0.2324	0.2282
1C	0.2002	0.2010	0.1987
1Cb	0.2001	0.2112	0.1969

The thermal conductivity results give the pure resin an average value of 0.2309 W/(m*K) and sample 1C an average value of 0.20015 W/(m*K). This decrease of 13.3% is thought to be due to the aerogel particles whose presence has already been confirmed by optical and electron microscopy.

4.2.3.5 Damage coefficient

Similar to the aerogel/PA-6 composites, the damage coefficient as originally described in [172] and given in Equation 6 was calculated to try and quantify the amount of damage to the aerogel structure.

As discussed, the values of k_l and k_u were calculated using the Hamilton and Crosser model [178] wherein the value of the continuous phase is that of the resin- 0.2309 W/(m*K) (sample 1P in Table 24), and the value for the discontinuous phase varied between 0.012 W/(m*K) [179] (thermal conductivity of the aerogel particles) for k_l and 1.4 W/(m*K) [180] (thermal conductivity of pure silica) for k_u. Finally, the volume fraction of the aerogel used was 0.21 which was calculated from the mass fraction (0.03) along with the density of the cured un-reinforced resin (1.19 g/cm^3) [167] and the density of the aerogel (0.135 g/cm^3) [179].

The values of k_l and k_u were determined as 0.1696 W/(m*K) and 0.3361 W/(m*K) respectively. This data was then substituted into Equation 6 along with the value of k_s, which was 0.20015 for sample 1C (from Table 24) and the damage coefficient of the aerogel within sample 1C was calculated to be 0.183.

4.3 Aerogel/Epoxy Coating

The experimental results for the aerogel/epoxy coating are given here and also published, along with the relevant discussion and inference, by the author in [193]. As stated in Chapter 3, the coatings are similar to the aerogel/epoxy samples discussed in the previous section since they showed the most promise amongst the materials considered in the current work. Examples of the dip coated samples used for characterisation in the present study are shown in Figure 55.

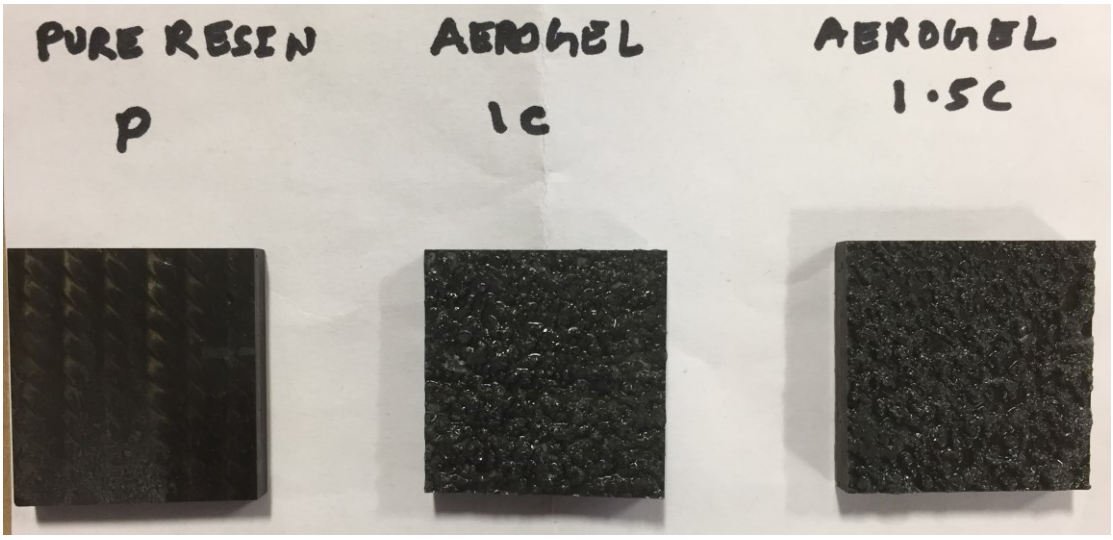

Figure 55 Coated CFRP samples made and used in the present study. From left to Right; pure resin coated samples (sample P), aerogel/epoxy coated samples (sample 1C) and aerogel/epoxy coated samples (sample 1.5C)

4.3.1 **Scattering/reflectance coefficient**

The scattering/reflectance plot for the samples obtained through the spectrophotometer with the integrating sphere is shown in Figure 56. It is seen that both the aerogel samples have similar curves and show a peak at the 200nm -250nm interval. As discussed in section 4.2.3.3, the higher prominence of the aerogel composites peak near the 200nm wavelength was also observed by Fernandes et al. [192] in their aerogel samples, thereby providing evidence for the material's existence in the coatings of the present work. Further, the pure resin coating shows an increase in this region as well, but the scattering intensity is not as high as the aerogel coated samples and the carbon fibre substrate does not exhibit this phenomenon thereby suggesting this to be an effect of the coating and in particular, that of the aerogel particles.

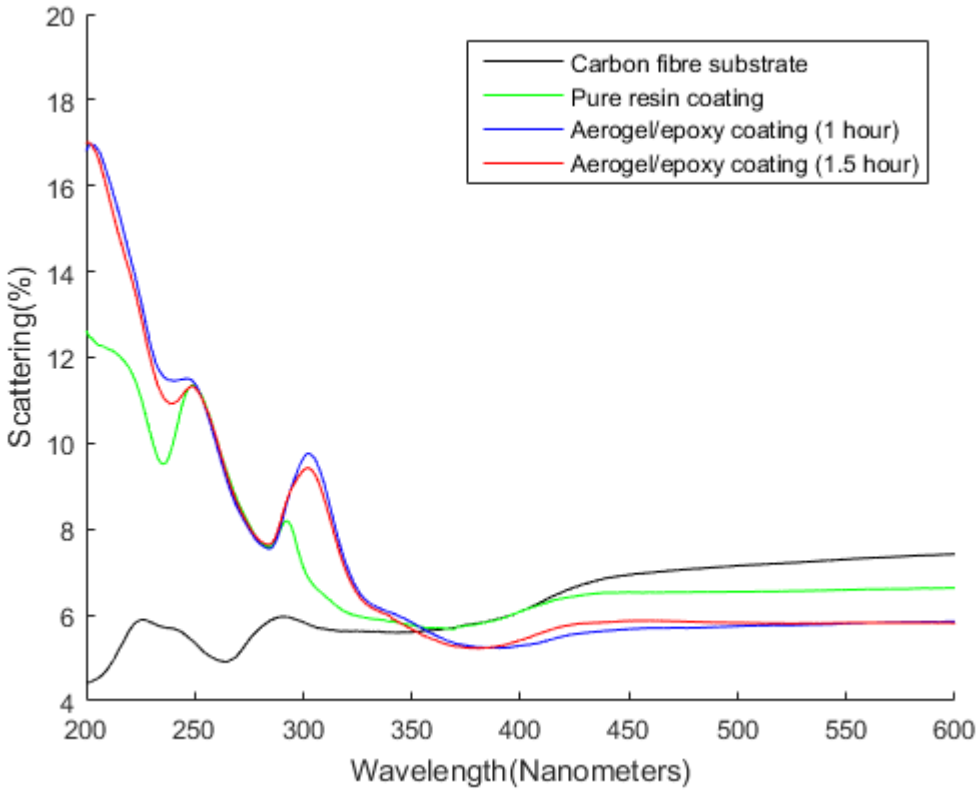

Figure 56 Scattering plot for the samples

4.3.2 **Heat flow across the sample**

Since the thermal conductivity values for each of the samples were to be calculated at three different temperatures- 50^0C, 75^0C and 100^0C, the heat flow across the sample at these temperatures had to be determined as described in section 3.2.6.2 and using Equation 4. The temperatures were measured using thermocouples with a Pyro Heater supplying the required heat. The results are given in Table 25 wherein the diameter and the thickness of the standard were 0.024m and 0.002m respectively. Further, the thermal conductivity of the standard used was 1.1 W/(m*K), as given in [194].

Table 25 Heat flow across the standard at different temperatures using Equation 4

Temperature (^{0}C)	Run	T1 (^{0}C)	T2 (^{0}C)	dT (^{0}C)	q (W)
50	1	44.7	41.8	2.9	0.72
	2	45	41.8	3.2	0.79
	3	44.2	40.9	3.3	0.82
	Average				**0.78**
75	1	65.5	59.6	5.9	1.46
	2	65.7	59.5	6.2	1.53
	3	65.1	58.7	6.4	1.58
	Average				**1.53**
100	1	86.6	77.7	8.9	2.20
	2	86.8	77.5	9.3	2.30
	3	86.3	76.9	9.4	2.33
	Average				**2.28**

The average of the three values calculated for each temperature was used in the subsequent thermal conductivity calculations.

4.3.3 Thermal conductivity

The thermal conductivity values along with the temperature difference between T1 and T2 thermocouples are shown in Table 26 for the samples in the study. Once again, Equation 4 in section 3.2.6.2 was used to calculate the thermal conductivities of the sample using the average q values obtained in Table 25. For the sake of comparison, the average thermal conductivity and the standard deviation values for each sample at the given temperature was also calculated and is shown in the table.

Table 26 Thermal Conductivity values for the samples at different temperatures

Sample	Thermal Conductivity					
	50°C		**75°C**		**100°C**	
	dT (K)	k (W/(m*K))	dT (K)	k (W/(m*K))	dT (K)	k (W/(m*K))
Pure Resin Coating (P)	6.4	0.67	11.9	0.71	17.8	0.70
	7.2	0.59	12.8	0.66	18.8	0.66
	6.1	0.72	11.7	0.74	17.6	0.73
	6.4	0.65	11.8	0.69	17.5	0.70
	6.2	0.65	12.1	0.65	18	0.65
	Average	**0.66**	**Average**	**0.69**	**Average**	**0.69**
	Std. Dev.	**0.047**	**Std. Dev.**	**0.037**	**Std. Dev.**	**0.033**
1 Hour Aerogel/Epoxy Coating (1C)	14.5	0.35	26.9	0.36	39.5	0.37
	13.8	0.39	24.7	0.43	35.3	0.45
	13.6	0.42	24.6	0.45	35.3	0.47
	15.2	0.36	27.5	0.39	39.9	0.40
	14.1	0.38	26.4	0.40	37.7	0.41
	Average	**0.38**	**Average**	**0.41**	**Average**	**0.42**
	Std. Dev.	**0.027**	**Std. Dev.**	**0.035**	**Std. Dev.**	**0.040**
1.5 Hour Aerogel/Epoxy Coating (1.5C)	15.9	0.33	27.1	0.38	39.5	0.39
	15.2	0.36	28.2	0.38	41.1	0.39
	17.8	0.29	30.1	0.34	44	0.35
	16.9	0.31	29.5	0.35	41.9	0.36
	17.6	0.31	32	0.33	45.9	0.34
	Average	**0.32**	**Average**	**0.36**	**Average**	**0.37**
	Std. Dev.	**0.026**	**Std. Dev.**	**0.023**	**Std. Dev.**	**0.023**

4.4 Modelling

4.4.1 Mesh optimisation and validation

To identify the most efficient element size, a model of the substrate was subjected to a constant temperature of 75^0C through all the nodes at the top of the geometry for 150 seconds. A random element towards the centre of the bottom surface was chosen and its temperature was plotted against time and compared with different element sizes; the results are shown in Figure 57. It is seen that regardless of the size of the mesh, all models attained steady state within 100 seconds. Mesh sizes lower than 0.0001m were not considered due to their complexity and resource constraints. The hybrid mesh model consisted of rectangular elements whose size was 0.001m in the plane perpendicular to the heat flow (x and y axes) and 0.0001m along the direction of the heat flow (z axis).

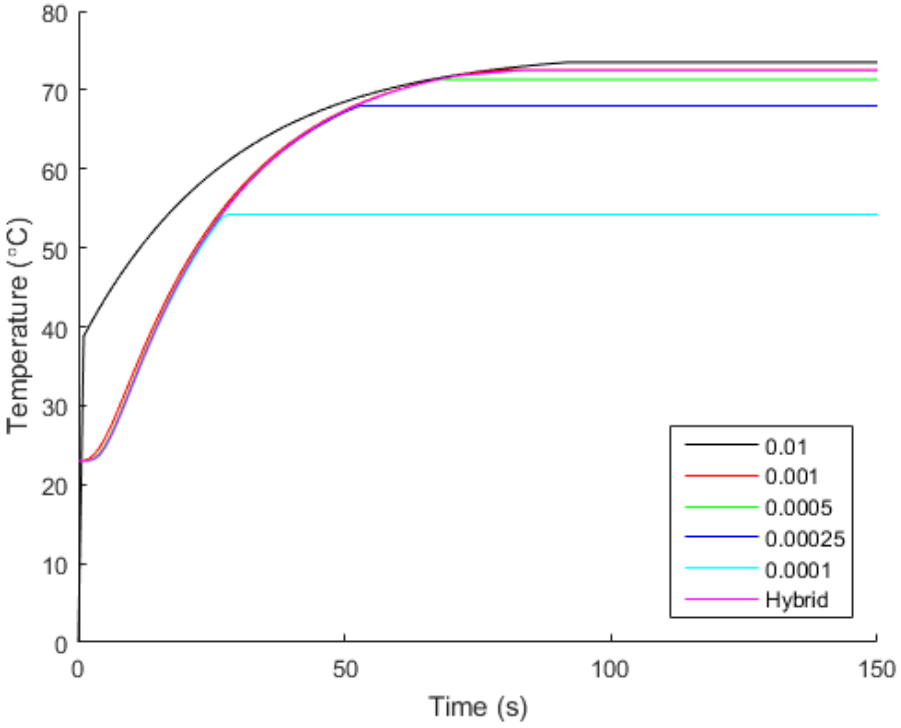

Figure 57 Mesh size comparison (sizes in m)

Table 27 Steady state temperatures for different mesh sizes

Mesh size (m)	**Steady state temperature (^{0}C)**
0.01	73.51
0.001	72.55
Hybrid	72.49
0.0005	71.35
0.00025	67.99
0.0001	54.22

From the results of Figure 57, which shows the temperature of the element in the bottom surface as a function of time, it is seen that 0.0001m and 0.00025m element sizes attained steady state conditions earlier and at lower temperatures than the coarser meshes, which displayed identical results. The results of the 0.01m mesh also

showed some difference from the other models especially at the beginning; this is thought to be due to the coarse nature of the mesh which resulted in the presence of the same element for both, top and bottom surfaces and would have resulted in the cross-sectional heat transfer occurring through a single element. Hence, this mesh is not considered further. When considering the steady state temperatures attained by the models (shown in Table 27), it is seen that none of them reached the input temperature of 75°C.

However, because no losses were defined in the original model, it is believed that temperatures at the bottom should ultimately reach the input temperature. Therefore, the convergence tolerance of the thermal solver (CGTOL in CONTROL_THERMAL_SOLVER) was decreased to reduce the error in the solution and hence, attain a more representative result. To find the most effective tolerance value, the 0.001m model was simulated with progressively smaller tolerance values starting from 1e-04 until 1e-14 with decrease of 0.01 for each successive step. The respective error from the equilibrium temperature (75^0C) was calculated and plotted as a function of the tolerance value in Figure 58. The temperature at the bottom was rounded off to two decimal places before calculating the error value. Once again, a random element towards the middle of the bottom surface was chosen for the calculation and the simulation time was increased to 300s.

As expected, Figure 58 shows a reduction in error as the convergence tolerance is lowered and stabilises at 0 from 1e-08 onwards. The results were also corroborated by the time taken to reach the steady-state (Table 28) which reaches a constant value of 221 seconds from 1e-08 as well. Hence, it is believed that the selection of 1e-08 would allow for more accurate simulation results. Although values lower than 1e-08

could also be chosen, they would result in more number of iterations and hence, larger simulation times and resource consumption.

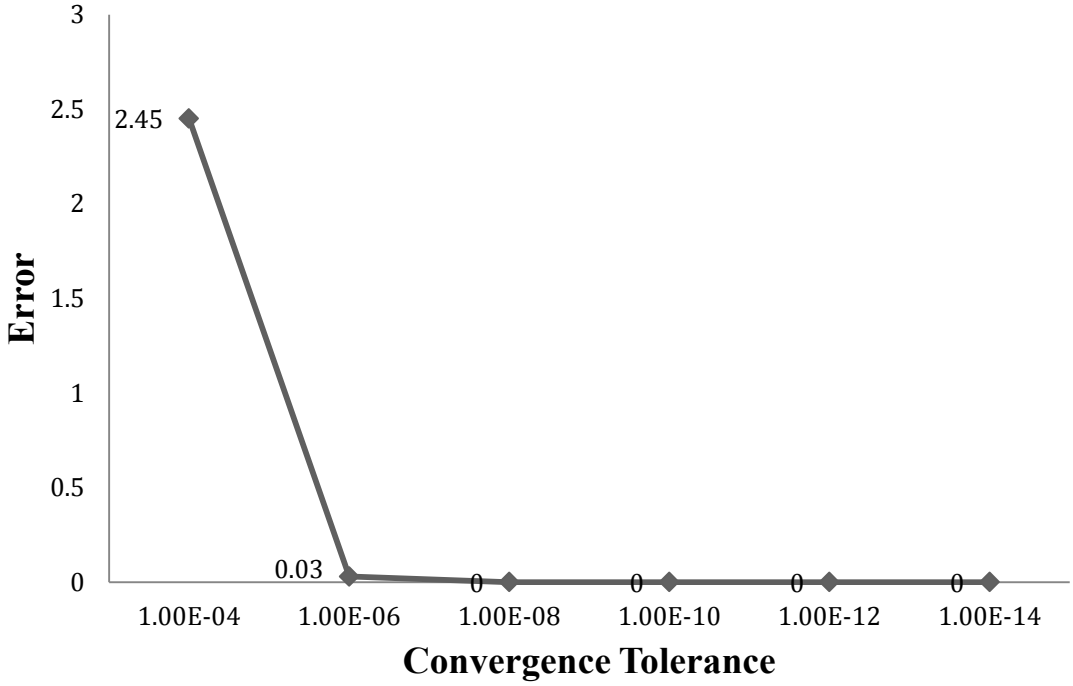

Figure 58 Simulation error as a function of convergence tolerance

Table 28 Steady state temperature times for different convergence tolerance values

Convergence Tolerance	Time to reach steady state (s)
1.00E-04	81
1.00E-06	177
1.00E-08	221
1.00E-10	221
1.00E-12	221
1.00E-14	221

Therefore to identify the most efficient mesh size, convergence tolerance value of 1e-08 was used to run the previously described models and the updated time-temperature plots are shown in

Figure 59. It is seen from the graphs that the models all reach 75^0C thereby overcoming the initial problem of lower temperatures. However, the mesh sizes tested in the present work show similar temperature profiles with respect to time and cannot be differentiated from one another. It must also be noted that the 0.01m mesh was not simulated for reasons identified previously. Therefore, the coarsest mesh was chosen to model future samples since it would consume the least resources and time. Additionally, the ineffectiveness of using hybrid meshes having different size perpendicular to and along the direction of heat flow is also shown in

Figure 59.

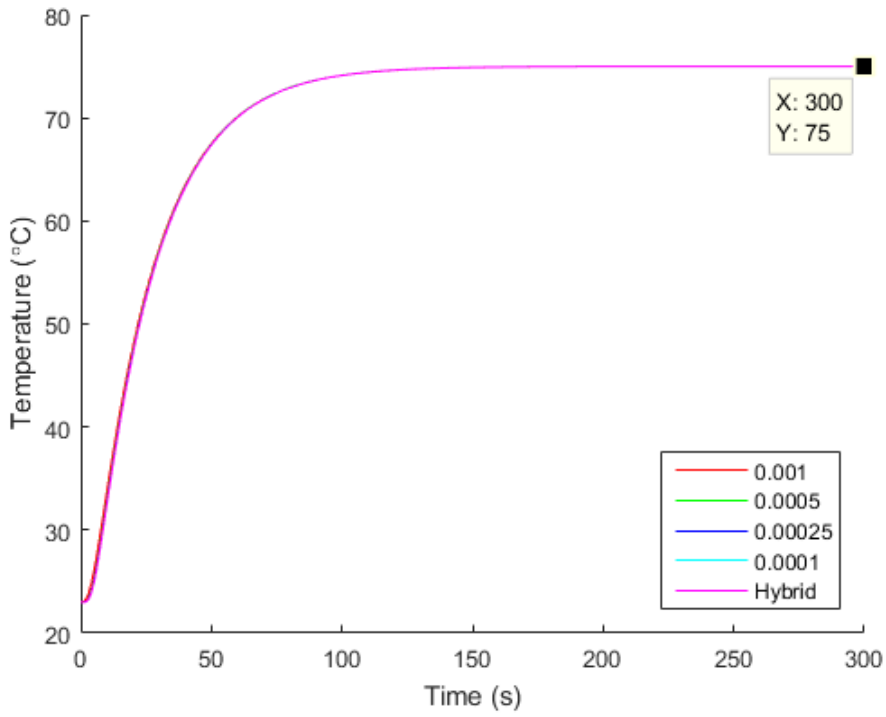

Figure 59 Updated mesh size comparison with a convergence tolerance value of 1e-08

According to the results presented in Figure 59, the selection of 0.001m mesh size would seem the most logical solution for future models. However, since a 0.7mm (0.0007m) coating was going to be applied onto the substrate, the mesh size needed to be smaller than the coating thickness since it is believed that a single element along a

materials cross section would result in a slightly different temperature profile as compared to the others (see Figure 57). Therefore a mesh size of 0.00025m was used for all future models. 0.0005m, although theoretically possibly, resulted in a single layer of elements due to the closeness of the mesh size to the coating thickness and hence was not considered.

To try and replicate the experimental setup given in section 4.3.3, two layers of coating were added to the top and bottom of the models as shown in Figure 60. This allowed a means of comparing the model with the experimental runs. To try and achieve this, three different temperatures- 50^0C, 75^0C and 100^0C were applied to the nodes at the top surface similar to the experimental setup and the model was allowed to run for 1800s (0.5 hours). The material properties for coating were defined according to Table 9 with the thermal conductivity value of 0.20015 W/(m*K) taken from Table 24. The output at the bottom surface is the steady-state temperature (rounded off to two decimal places) of a single random element taken towards the centre of the bottom surface for each run. This result, along with the time taken to reach the steady state is reported in Table 29 for the runs of 0.00025m model.

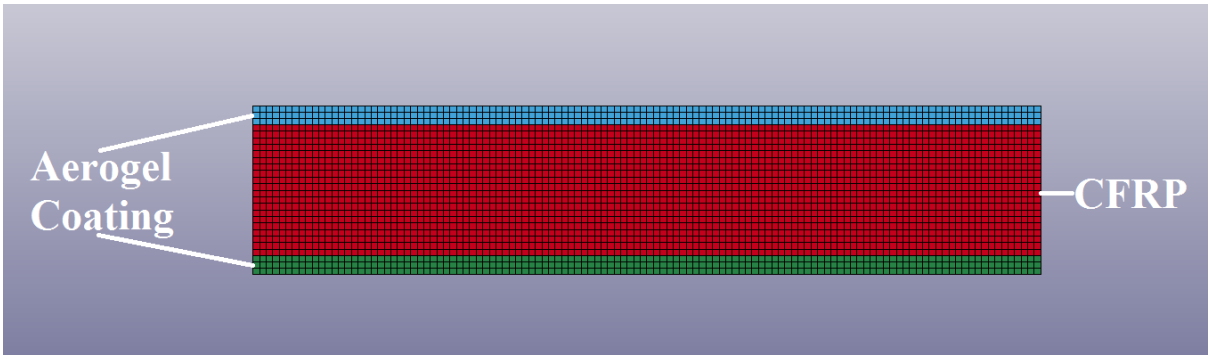

Figure 60 Sectional view of the coated sample

The results show that the temperature at the bottom of the specimen matches the input temperature for all three cases, thereby confirming the previous findings for this particular model and tolerance value. Further, the time taken to reach steady state

conditions increases with the input temperature. Hence, these results demonstrate the validity of using the present model to simulate coated samples across the range of temperatures considered in the present study.

Table 29 Surface temperature of coated models

Element size	Temperature on the top surface (^{0}C)	Temperature on the bottom surface (^{0}C)	Time to reach steady state (s)
0.00025	50	50	1419
	75	75	1525
	100	100	1589

Finally, the results of the coated samples were compared with the experimental runs 1C and 1.5C as shown in Figure 61. The predictions of the FE model (shown as a line) were higher when compared to experimental results (markers). However, this is believed to be due to the absence of any heat loss effects such as air convection cooling in the model and the use of theoretical values in the models using the rule of mixtures (with the exception of the coating thermal conductivity) which, does not assume any resin infiltration into the aerogel. Additionally, although the temperature set in the experiment was as described previously, the actual readings at T1 (top thermocouple) were lower. Therefore when accounted for these differences, the model does represent a fair reproduction of the experiment showing the right linear trend between the temperatures.

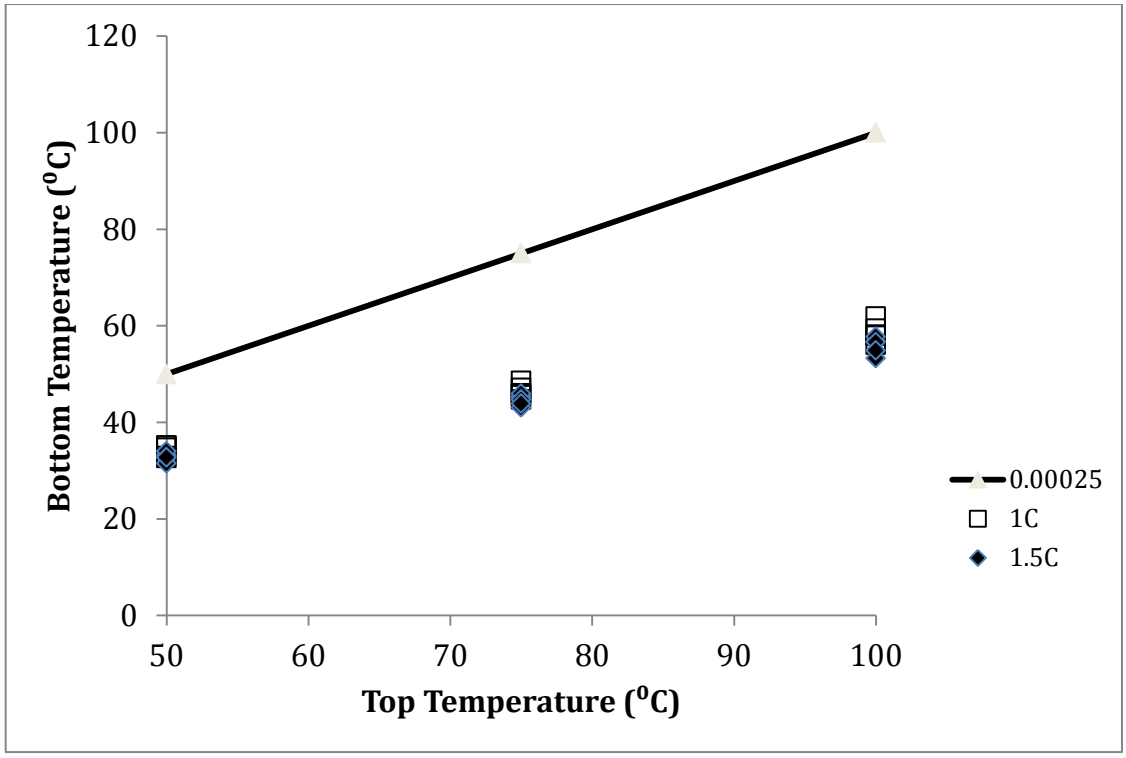

Figure 61 Comparison of FE and experimental data

4.4.2 Model predictions

To try and predict the performance of these coatings in a different loading case, the validated 0.00025m model was subjected to a load changing every 10 seconds between 50^0C and -50^0C for 1800 seconds as given in Figure 62; a reduced keyword file for this model is given in APPENDIX III. These models had an initial temperature of 23^0C applied to all the nodes. Due to numerous reasons such as resource availability and/or economics, it may not always be possible to use a double layered coating. Therefore, the FE model with only the top coating and only the bottom coating were also simulated and compared.

Once again, the temperature of a single element towards the middle of the bottom surface is shown in Figure 63 against time for the three different types of coatings. It is observed that the results of the three runs started at 23^0C due to the initial temperature definition and attained equilibrium around 0^0C. However, the time at

which they reached steady state varied with the type of coating used, with the double coating taking the longest at approximately 800 seconds and the bottom coating being quickest at around 200 seconds; the top coating was in-between taking close to 600 seconds. Additionally, the bottom coating resulted in bigger fluctuations in temperature at steady state conditions and the double coating had the lowest; once again, the top coating's behaviour was in the middle.

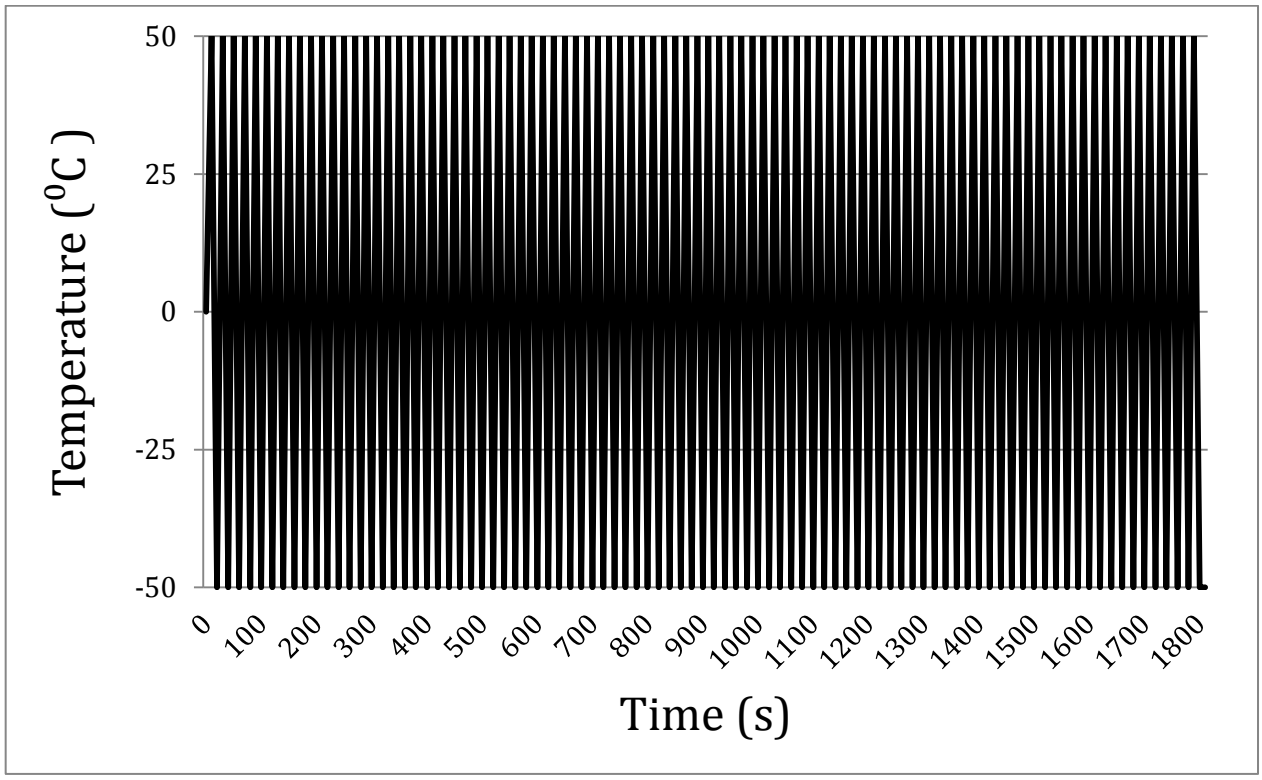

Figure 62 Input temperature profile

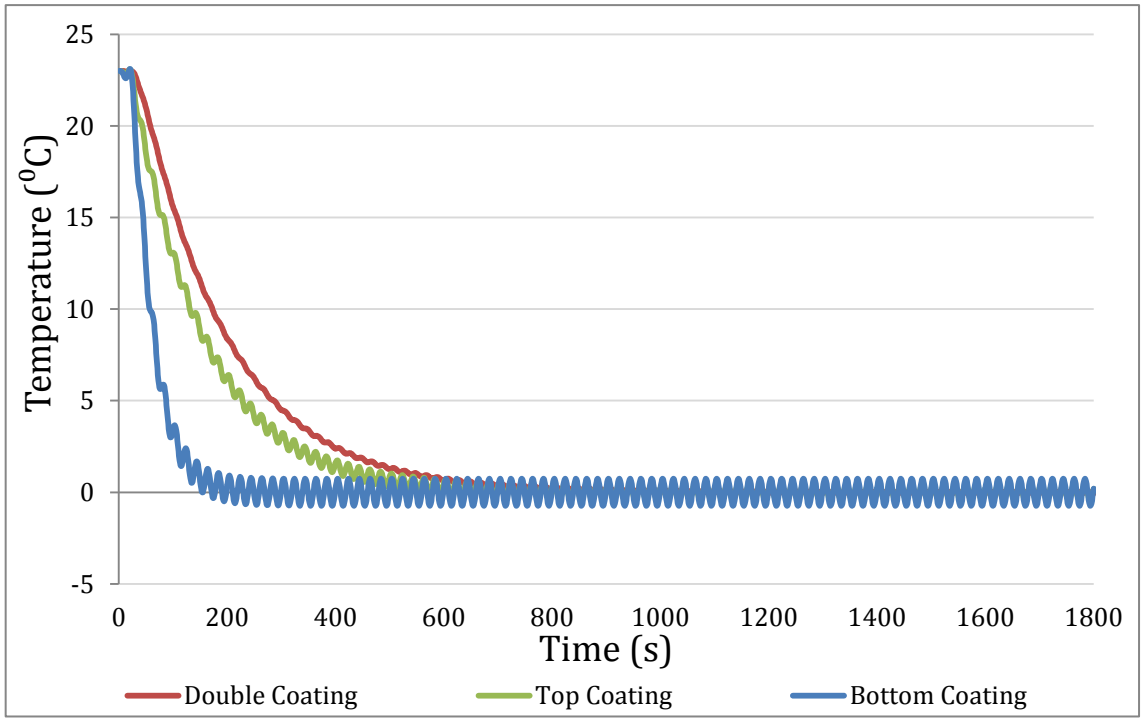

Figure 63 Performance of different coating types with a cyclic temperature load

4.5 Fatigue Performance

The current section describes the fatigue behaviour of unaged, aged and aerogel/epoxy coated CFRP composites. Since the fatigue loads were determined as percentage of the ultimate tensile load, 5 samples from each batch was subjected to a uniaxial tensile test, which is discussed initially, and then the fatigue results of the batches along with their SN curves are discussed. The aged samples were heated isothermally at 70^{0}C for approximately 10, 120 and 1000 hours thereby following a logarithmic scale. With regards to the coating samples, it was planned to heat them at 70^{0}C for 1000 hours as well; however, the oven was unexpectedly turned off in the middle and it is estimated that the samples received approximately 420 hours of heat. The results are nevertheless reported for all samples for information purposes. An example of a tabbed and coated specimen is shown in Figure 64. Finally it must be

noted that the aging hours are rounded off to the nearest 10 (hours) for the sake of simplicity.

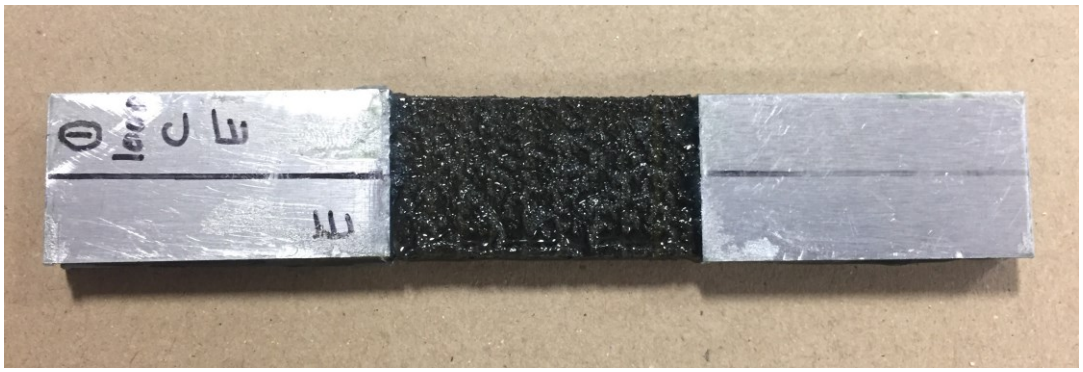

Figure 64 An aerogel/epoxy coated tabbed specimen used for tensile and fatigue testing

4.5.1 **Tensile Testing**

The ultimate tensile loads and the corresponding stresses for the different samples in the current work are listed in Table 30. It is seen that the loads and stresses of the unaged and aged CFRP specimens are similar, pointing towards a negligible effect of the aging process for the time durations used. However, the coated samples show a decreased stress of 135.61MPa at failure, which could be due to the application of the coating which would have increased the cross sectional area of the sample. Therefore, because the present work is interested in measuring the tensile and fatigue performance of the CFRP (and not the coating), load, rather than stress (at failure) is considered during subsequent calculations. This is done because the carbon fibres (in the CFRP substrates) will carry the majority of the load with the coating carrying negligible amounts during the testing process.

Table 30 Tensile Test results for unaged, aged and coated CFRP samples

Type	Sample	Failure Load (kN)	Stress (MPa)
CFRP Unaged Sample	1	20.94	175.18
	2	20.73	169.93
	3	21.06	172.56
	4	21.09	170.85
	5	20.48	170.77
	Average	**20.86**	**171.86**
CFRP Aged- 10 Hours	1	20.38	169.90
	2	19.57	167.41
	3	21.16	171.23
	4	21.12	172.23
	5	20.72	166.18
	Average	**20.59**	**169.39**
CFRP Aged- 120 Hours	1	20.00	168.14
	2	21.07	173.26
	3	21.56	176.49
	4	19.54	164.81
	5	20.99	176.36
	Average	**20.63**	**171.81**
CFRP Aged- 1000 Hours	1	19.47	163.28
	2	20.63	167.16
	3	20.19	168.77
	4	21.80	178.48
	5	22.35	185.91
	Average	**20.89**	**172.72**
Coated CFRP Aged- 420 Hours	1	21.63	129.89
	2	21.91	139.15
	3	22.34	138.77
	4	23.37	139.57
	5	21.30	130.69
	Average	**22.11**	**135.61**

The average failure loads shown in Table 30 were used in the calculation of various percentage loads required for fatigue testing discussed subsequently.

4.5.2 Fatigue Testing

The fatigue performances of the unaged, aged and coated CFRP materials are shown in Table 31 and graphically plotted in Figure 65. As expected the fatigue life of the materials is dependent on the load level applied with higher levels resulting in lower number of cycles before failure. The results between the aged and unaged CFRP specimens are identical thereby further confirming the negligible effect of the aging process undertaken in the present study. These results were also echoed by the coated sample which, given the similarity of the uncoated samples is expected.

Table 31 Fatigue performance of the unaged, aged and coated samples

Sample Type	Load Levels	Sample no	Load (kN)	Cycles
CFRP- Unaged Sample	50%	1	10.43	188,888
		2	10.43	340,016
		3	10.43	193,600
	55%	1	11.47	62,182
		2	11.47	61,288
		3	11.47	61,866
	65%	1	13.56	5976
		2	13.56	10,082
		3	13.56	4,781
	80%	1	16.69	798
		2	16.69	243
		3	16.69	619
CFRP Aged- 10 Hours	50%	1	10.30	149,968
		2	10.30	186,312
		3	10.30	151,000

	55%	1	11.32	62,742
		2	11.32	57,850
		3	11.32	63,484
	65%	1	13.38	2,184
		2	13.38	6,488
		3	13.38	7,649
	80%	1	16.47	465
		2	16.47	395
		3	16.47	219
CFRP Aged-120 Hours	50%	1	10.32	287,296
		2	10.32	101,820
		3	10.32	187,944
	55%	1	11.35	118,832
		2	11.35	40,450
		3	11.35	46,316
	65%	1	13.41	3,774
		2	13.41	2,873
		3	13.41	1,207
	80%	1	16.51	21
		2	16.51	23
		3	16.51	317
CFRP Aged-1000 Hours	50%	1	10.44	156,912
		2	10.44	231,800
		3	10.44	205,528
	55%	1	11.49	27,727
		2	11.49	62,084
		3	11.49	63,410
	65%	1	13.58	5,220
		2	13.58	11,452
		3	13.58	3,425
	80%	1	16.71	81
		2	16.71	277

		3	16.71	162
Coated CFRP Aged- 420 Hours	50%	1	11.06	57,870
		2	11.06	114,144
		3	11.06	79,012
	55%	1	12.16	26,642
		2	12.16	22,287
		3	12.16	22,106
	65%	1	14.37	5,028
		2	14.37	1,874
		3	14.37	3,909
	80%	1	17.69	84
		2	17.69	126
		3	17.69	83

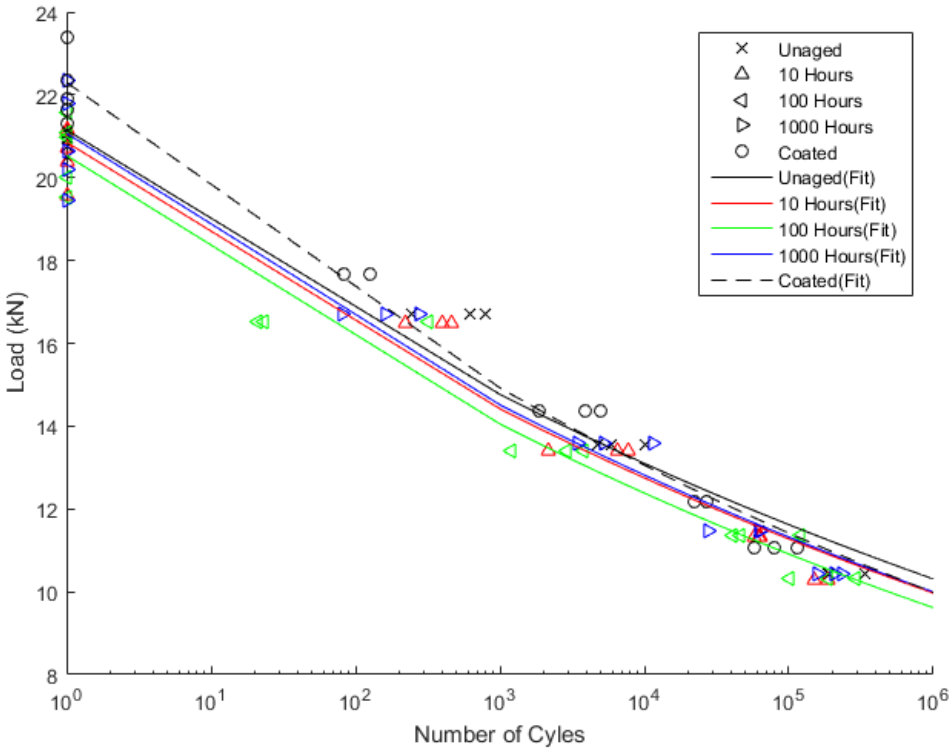

Figure 65 Graphical representation of the fatigue parameters

4.5.3 **LN Curves**

To allow a more universal representation of the LN (Load- Number of cycles) curves, the experimental data in the previous section was fitted with a power function as shown in Equation 14.

$$y = F * x^G$$

Equation 14

To fit the data, the value of the constants i.e. '*F*' and '*G*' in Equation 14 was determined using the 'power1' function in MATLAB. These values for the different samples are tabulated in Table 32. It must be noted that the r^2 values for all the fits were >0.96 thereby suggesting a good fit between the experimental data and the equation.

Table 32 LN curve parameters

Sample	F	G
CFRP- Unaged Sample	21.15	-0.05202
CFRP Aged- 10 Hours	20.86	-0.05344
CFRP Aged-120 Hours	20.53	-0.05492
CFRP Aged-1000 Hours	21.07	-0.05397
Coated CFRP Aged- 420 Hours	22.30	-0.05815

The constants were then used to plot an LN curve. The number of cycles was generated and input as a 10,000x1 array up to 1,000,000 cycles with the load being generated based on the corresponding equation for a given sample. The results are shown in Figure 66. Once again, a negligible difference between the unaged CFRP, aged CFRP and the coated samples is seen. Therefore, it is difficult to ascertain the effects (if any) of the coating on the aging performance of the substrate since the substrate themselves, did not show any variation for the aging process followed in the

present work. Nevertheless the results are still presented for the sake of information/database building and, as a possible reference for future research but no further discussion will be undertaken on this topic.

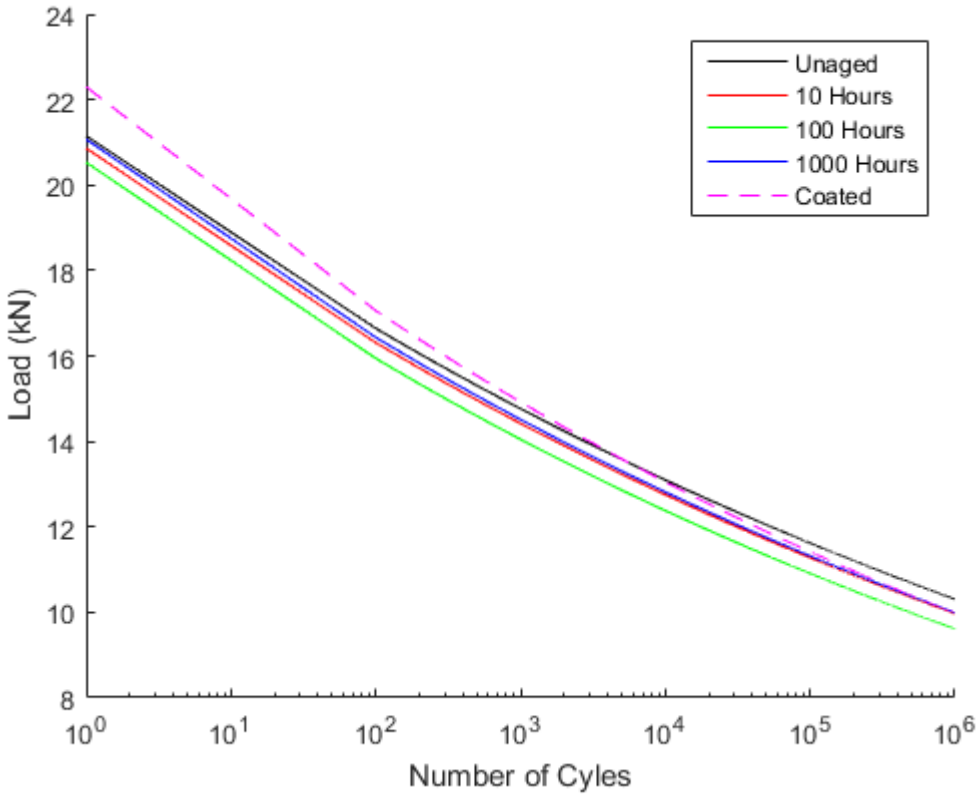

Figure 66 LN curve generation based on the model

5 Discussion

The results of the experiments carried out on the materials in the present work are analysed and put into perspective with the relevant literature in the following chapter. These are then used to tackle each objective defined in section 2.9 individually.

5.1 Nylon-6 (Thermoplastic) Matrix

The experimental results of the aerogel/PA-6 composites compare the thermal conductivity of PA-6/Aerogel composites extruded using two different extrusion speeds; 65 rpm and 5 rpm. The results point towards a lower thermal conductivity for the material processed using a lower extrusion speed. When considering values of the damage coefficients, sample B and sample C show values of 0.41 and 0.33 respectively; this could roughly be translated as sample B losing the structure of around 41% of the aerogel and sample C loosing around 33% of its aerogel. Therefore, although the lower extrusion conditions of sample C did provide a relatively better material with reference to thermal conductivity through a better retention of the aerogel structure, it is believed that the compression moulding contributed to the destruction of a significant number of the aerogel particles within the sample.

This statement is based on the initial ESEM and optical microscope studies, which showed an improvement in the retention of the aerogel in sample C compared to B. Further, it can be evidenced from the literature that the thermal conductivity of the 'as-extruded' aerogel/Nylon (MXD6) composite reduced as much as 47% when compared to the virgin polymer [131]. However, when comparing the results obtained in this study, it is seen that even sample C's value was only around 11% lower than that of sample A. Therefore, further research must look to negating this effect of

compression moulding by either studying the moulding parameters and/or other processing techniques which builds upon the initial advantage offered by the lower extrusion speeds. This is thought to be critical because the final moulding (of the extruded material into its final shape) is important for the material to attain the required shape for practical applications. Additionally, future research must also investigate the long term oxidation effects of the polyamide matrix and the subsequent addition of potential stabilisers, as discussed by Gijsman et al. [195].

Nevertheless, the results in this study do show some promising trends with respect to the thermal conductivity values with the aerogel composites showing lower thermal conductivity values. A similar trend was also seen in the work of Jabbari et al. [196] who show the reduction of thermal conductivity for a poly(vinyl chloride) matrix containing aerogel. This is believed to be due to the Knudsen effect which allows aerogels to have high insulation capabilities as discussed by Raed & Gross in Jabbari et al. [196]. When comparing the results of sample's B and C, it is observed the lower speeds of the extruder for sample C helped preserve more aerogel and hence a lower thermal conductivity. Additionally, because sample C showed a lower standard deviation during thermal diffusivity measurements, it is suggested that there would be a lower temperature gradient across its cross section during heat transfer and could result in a better thermal aging and fatigue performance. The more uniform distribution of heat in sample C also point towards a homogenous material and good mixing of the aerogel particles within the PA-6 matrix, thereby negating one of the limitations of using lower extrusion speeds.

5.2 Epoxy (Thermoset) Matrix

The microscopic images presented for the aerogel/epoxy material revealed the presence of aerogel particles within the epoxy resin matrix. Although, the images do

not allow the determination of the internal structure of the aerogel particle, they do permit the observation of the mechanical destruction of the particles seen in samples 1.5B and 1.5C. This is an important parameter because the destruction of the aerogel particle would afford a larger surface area for the liquid resin to infiltrate the nano-pores. The infiltration of the aerogel pores is a major factor in limiting the insulation performance of the aerogel/epoxy composites as shown by comparing the thermal conductivities of aerogel and HGM fillers within an epoxy matrix in [104]. Therefore, to limit this destruction, the mixing of the aerogel before 1.5 hours of the addition of the resin and hardener is recommended. On the other hand, lower viscosity values of the resin would also result in higher infiltration rates; hence the addition of the aerogel should be as delayed as possible. The microscopic images also showed that this balance can be achieved by adding the aerogel at around the 1 hour mark.

The EDX analysis also established similar results supporting the damage and resin infiltration phenomena. The smaller silica (aerogel) particles observed in sample 1.5B provides evidence for the mechanical damage of the aerogel particles. On the other hand, EDX scans of carbon (C) across an aerogel particle in sample 0.5B showed a very low rate of decrease when compared to sample 1B wherein, a decrease in the level of carbon is higher and more noticeable and, a well-like structure in the carbon spectrum is obtained. In fact, the spectral mapping of sample 1B in Figure 45 shows a reduction in the intensity of C and an increase in the intensity of Si across all aerogel particles. Another limitation of adding the aerogel at 1.5 hours is the reduction in the mouldability of the material due to the higher viscosity of the resin at this stage of the cure.

Nevertheless, the recommended timeframe for aerogel addition is valid for this resin system only. To derive a more universal solution, viscosity measurements of the

curing resin system at 0.5, 1 and 1.5 hours should be quantified. When comparing the effect of the wetting agent, the results of batch C are similar to batch B with the samples at 1 hour demonstrating the most promise for the retention of the aerogel structure and limiting the resin infiltration. But the presence of a wetting agent is expected to increase the adhesion between the aerogel particles and the resin thereby, improving the interface between the same. Hence, the use of a wetting agent i.e., batch C will be useful for durability of the composite structures in the present case. However, the use of any surface modification has the potential to increase the thermal conductivity due to the better filler-matrix adhesion which would reduce the interfacial thermal resistance [152]. Therefore, further/future additions should look to consider this as well.

The spectroscopic analysis at 665nm exhibited absorbance in samples 1B and 1C of approximately 75% and 70% respectively as compared to around 6% in sample 1A which is quite significant thereby providing evidence for existence of the aerogel particles. Furthermore, an increase in reflectance below 350nm for the aerogel composites that showed sharper peaks unlike the pure resin samples provide additional support for the former's existence and possible retention of nano-pores (as discussed in section 4.2.3.3). When comparing the transmittance results during the cure of the material, it is thought that the resin infiltration into the aerogel particles influences the results more than the flow of the resin through the glass slide. Finally, the transmittance plots of the samples at 1 hour showed a greater variance between the runs measured during the cure as compared to the samples at 1.5 hours establishing a higher degree of flow with a less viscous resin and hence, more mouldability for the former.

Therefore from the various experimental techniques and data, sample 1C is believed to be the most promising material. Hence, to assess the amount of resin infiltration into the aerogel particles and to quantify the material's performance, the thermal conductivity value was measured and compared with the pure resin sample. The pure resin sample had a thermal conductivity value of 0.2309 W/(m*K) and the aerogel/epoxy sample's (1C) value was measured at 0.20015 W/(m*K).

Zhao et al. [133] state that the aerogel/epoxy composites in their work showed values between 0.105-0.175 W/(m*K). However the thermal conductivity of the resin in their work is much lower- between 0.17-0.18 W/(m*K) which would reflect in the lower values as compared to the present study. Maghsoudi & Motahari [137] were able to attain aerogel/epoxy composites with thermal conductivities of 0.074 W/(m*K); however, their work used ground aerogel particles with diameters between 200 nm and 300 nm which were much smaller than their counterparts in the present work. Therefore, it is believed that for a given mass fraction, the number of aerogel particles was much higher thereby offering more interfaces/obstacles to the phonons. Alternatively, the greater destruction to aerogel due to the higher viscosity could have outweighed the advantages offered through the lower levels of resin infiltration. However, further research is needed to confirm either/both theory. In the work of Kim et al [136] the thermal conductivity of the 'as-received' aerogel/epoxy composites is close to 0.10 W/(m*K) compared to ~0.27 W/(m*K) of the epoxy. The greater decrease in their study could be explained by their choice of resin which is much more viscous than the one used in the present study hence, decreasing the resin infiltration into the aerogel. However as previously discussed, a more viscous resin would result in lower mouldability.

Nevertheless, the 13.3% decrease in thermal conductivity observed in the present work shows the potential in developing aerogel-epoxy composites using the method identified in the present study. To illustrate further, Yung et al. [105] also obtained a 13.3% decrease in thermal conductivity for HGM/epoxy composites using 51.3 vol% of the filler. This volume is more than double of what was used in the present work (21 vol%), thereby showing the effectiveness of aerogel as potential fillers for thermal insulation application. However, as seen by the work of Zhu et al. [106], this can potentially be decreased to 60% by increasing the volume fraction (to 60%) and decreasing the density of HGM (to 125g/cm^3), thus providing further developmental opportunities for aerogel based composites.

To further quantify the amount of resin infiltration, a damage coefficient of 0.183 for sample 1C was calculated using the method outlined previously; this could be roughly translated to 18.3% of the aerogel being damaged. Although, this method is by no means perfect, it does allow a quantification of the damage to the aerogel structure and hence, a means of comparison. However, although the damage coefficient considered in this study offers a quantification of the aerogel's structural destruction; it is still rudimentary because it only accounts for the thermal conductivity of the materials. For a more accurate description, additional parameters must be evaluated and incorporated into the calculation. One such method could potentially incorporate the change in volume fraction for the same mass of aerogel and silica particles due to the difference in density between the two. Another potential route could be the evolution of Equation 6 into Equation 15 thereby considering additional material properties.

$$D_c = \frac{\sum_n \left(\frac{(P_s - P_l)}{(P_u - P_l)}\right)}{n}$$

Equation 15

Where P_s = Required property of the sample, P_l = Lower bound of the required property, P_u = Upper bound of the required property and n = Number of properties tested.

As discussed earlier in section 2.6.2.1, the cure kinetic parameters are critical in the identification of the optimum cure conditions [141] [142]. Therefore, to ascertain any effects due to the addition of the aerogel and the wetting agent on the cure of the resin, these values were determined for the aerogel/epoxy composites in the present study. From the results, it is seen that the Sestak-Berggren equation models the experimental data quite accurately and can be used to represent the respective materials in the present study. Once again, there is a difference in the model parameters between the epoxy (batch 1) and the aerogel/epoxy (batches 2 and 3). However, the cure kinetic parameters of the aerogel/epoxy composite with the wetting agent (batch 3) are similar to that of a normal aerogel/epoxy composite (batch 2) indicating a similar rate of cure and cure kinetics. Hence, the use of a wetting agent is advocated due to it potentially increasing the adhesion between the aerogel particles and the resin (as identified previously).

5.2.1 **Coating**

The thermal conductivity results of aerogel/epoxy coatings (Table 26) show a decrease in the thermal conductivity between the pure resin samples and aerogel/coated samples. The percentage decrease compared to the pure resin coating is shown in Table 33 for the temperatures discussed in the present study wherein Coating 1C showed an average decrease of 40.7% decrease and 1.5C showed a 48.6%

average decrease in thermal conductivity values. Although sample 1.5C did show a greater decrease in thermal conductivity due to a lower amount of resin infiltration into the aerogel pores, it must be noted that the specimens were of a simple cuboid shape hence the higher viscosity of the resin at this stage of the cure would not have had a great effect on the final property. But more complex shapes could result in greater difficulty during the coating process. Also, these measurements are representative of the whole material not just the coating; hence comparison with the bulk material is not useful and is not carried out in the present study. But both results do show a decrease in thermal conductivity when comparing the aerogel/epoxy samples with just the resin. The existence of the aerogel particles with the nano-pores was also supported by the reflectance spectrums of the samples in the study which showed the presence of peaks at the 200-250nm interval for the aerogel coating. This peak was absent in the pure resin and the CFRP substrate samples. The reflectance spectrum of the aerogel coating also had a peak at 300nm which is believed to be the result of the wetting agent. However, further research is needed to confirm this speculation.

Table 33 Thermal conductivity percentage decrease of aerogel/epoxy coated samples

Sample	**50^{o}C**	**75^{o}C**	**100^{o}C**	**Average**
1C	42.4	40.6	39.1	**40.7**
1.5C	51.5	47.8	46.4	**48.6**

When considering the FE simulations of the three types of coating, the double coating showed less variation in temperature at steady state compared to both single coating systems. But the latter attained equilibrium quicker than the former. Therefore, the choice of the coating system would depend on the specific requirement of the application. The double coating system would be preferred in environments where

there are cyclic loads since the steady state is maintained at an almost constant temperature. Additionally, any change would be carried out at a slower rate resulting in a more comfortable environment for any living beings present. However, if a double coating system is not possible, a single top coating is advocated. But if there is a need to maintain the inside surface of the coating at a given bandwidth of temperature close to the equilibrium temperature in a randomised loading, then the single coating at the bottom is suggested.

However regardless of the coating system selected, the FE models do show an improvement in the thermal insulation performance of the material with an aerogel coating and recommends its usage. Nevertheless, it is believed that a more comprehensive model closer to experimental data is needed to make more accurate predictions. One possible route to achieving this, apart from accounting for the heat losses, would be the use of actual experimental data as input where the resin infiltration into the nano-pores of the aerogel would also be accounted for.

It must also be noted that the coatings chosen and characterised here were designed to increase the life of the CFRP substrates used in low-medium temperature applications hence, the temperatures in the present work don't exceed 100°C. This is a further reason for selecting epoxy as a thermoset binder since the high temperature limitations of the polymer can be ignored.

5.3 YSZ coatings

Although the main focus of this work was the incorporation of aerogel particles into a polymer matrix, the possibility of applying YSZ coatings using sol-gel were also briefly investigated. However because initial investigations were not successful, it was not included in the main body of the work. Nevertheless, some information regarding the process are discussed here and in APPENDIX I for future reference.

Since the existing sol-gel preparation of YSZ involves a drying/calcination process at high temperatures- 950^{0}C or 1150^{0}C [197] [198], a modified sol-gel process was tried in the present work. Here, a silica sol-gel with the YSZ particles embedded within its 3 dimensions framework was processed and applied. Spin coating was chosen as the method of application since, according to Kavitha et al. [199], the surfaces of thin films produced using this method offer, amongst other advantages, a smooth surface, high homogeneity and precursor purity with low processing temperature and cost. The work of Xu et al. [200] shows the possibility of applying YSZ through this process, even though it must be noted that the authors considered a different substrate and used much higher drying temperatures.

Although a visible coating was produced on the substrate **(**APPENDIX I**),** the results show the absence of a sol-gel network and were more akin to YSZ powder suspensions. This could have been due to the presence of the YSZ particles which might have chemically disrupted the process by replacing the expected reactions or by physically interrupting the 3 dimensional gel formation. Alternatively and more possibly, the absence of high temperatures would not have allowed the solution to gel. Therefore, although further research may have allowed a better insight into the low temperature sol-gel formation and the interactions of the YSZ particles in the 3 dimensional network; alternate materials and approaches were considered more appropriate due to the possible complexities that could arise from this process.

Additionally, even though YSZ is considered a good thermal insulator, newer materials such as aerogels are more effective and efficient. Hence, the incorporation of the latter in a polymer was adopted as the main objective of this study and considered throughout.

5.4 CFRP Fatigue

From the tensile and fatigue results of CFRP samples given in section 4.5, it is observed that the aging criteria adopted for present work has negligible effect on the material's performance. Therefore, only the parameters of the unaged and uncoated CFRP are considered further.

To try and offer a more universal applicability, the loads (at failure) were initially converted to their respective stress values using the cross sectional area of the specimen. These values along with their respective cycles to failure for the unaged and uncoated CFRP (henceforth referred to as just uCFRP) are listed in Table 34. These results are also plotted graphically in Figure 67. The data was once again fitted using the 'power1' function in MATLAB. However to try and achieve a better fit with the data, the 'power2' function was also tried and the resultant fit also shown in Figure 67.

Table 34 Stress parameters for unaged uCFRP

Load Levels	Sample no	Stress (MPa)	Cycles
Uniaxial Tensile (100%)	1	175.18	N/A
	2	169.93	
	3	172.56	
	4	170.85	
	5	170.77	
80%	1	137.70	798
	2	136.84	243
	3	133.91	619
65%	1	112.25	5976
	2	109.63	10,082
	3	111.14	4,781
55%	1	94.20	62,182
	2	93.06	61,288
	3	94.89	61,866
50%	1	85.77	188,888
	2	85.15	340,016
	3	85.77	193,600

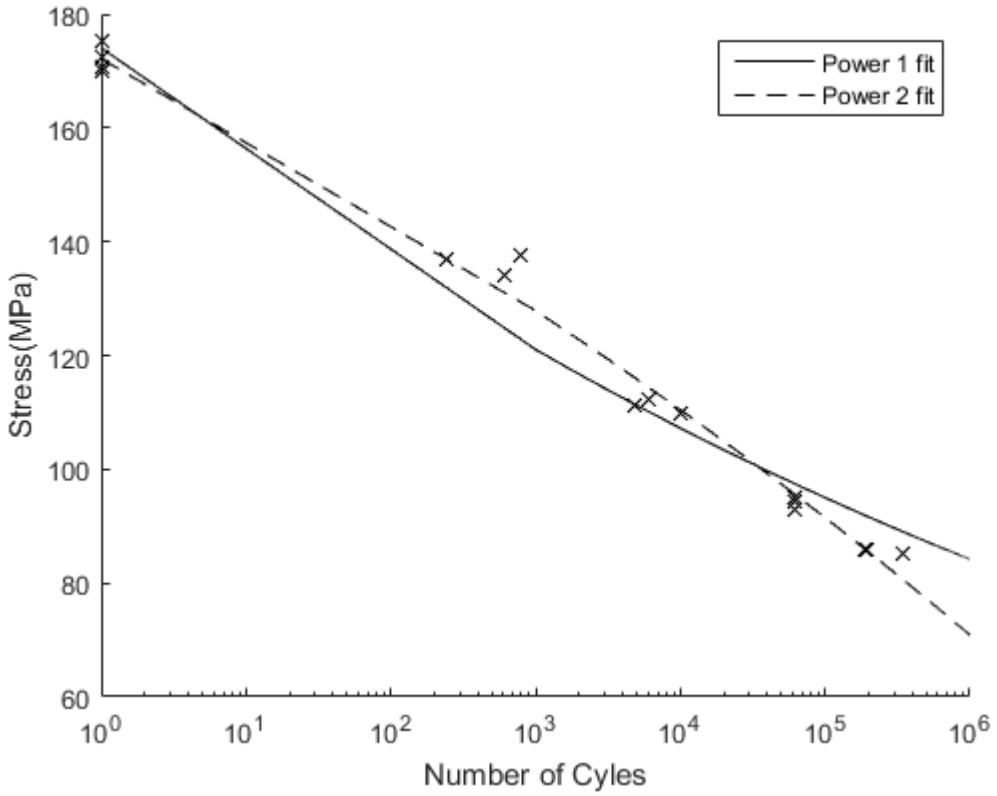

Figure 67 SN curve of uCFRP composites

The fitted constants for both, 'power1' and 'power2' functions are shown in Equation 16 and Equation 17 respectively. When comparing the closeness of fits (r^2 values), it is seen that the 'power1' function had a value of 0.97 which demonstrated a good fit with the data. However, the 'power2' function was able to go up to 0.99 thereby suggesting an excellent fit. Therefore the latter model, shown in Equation 17, was deemed to be more representative of the fatigue behaviour of the material in the current study.

$$\sigma = 174.1 * \left(N_f{}^{-0.05259}\right)$$

Equation 16

$$\sigma = \left(-153.7 * \left(N_f{}^{0.03664}\right)\right) + 325.8$$

Equation 17

Where σ = Stress (MPa) and N_f = Number of cycles.

The stresses in Figure 67 were then normalised using the average tensile strength from Table 34 and the resultant plot is shown in Figure 68. From the results it is seen that the stress of the current material decreases almost linearly with the number of cycles (in log scale). This was also seen in other composites tested by Harris et al [201] who, determined a linear S/logN plot for XAS/913 and 914 carbon fibre/epoxy composites. However, the results (particularly the UD laminates) for an intermediate modulus T800/6376 composite in their work had a slight downward trend towards higher cycles (>10^6 cycles). According to the authors this is due to the change in failure mode from a fibre dominated behaviour to a secondary stage and will eventually occur in any kind of reinforced plastic. This downward trend was also seen by Justo et al. [29] who noticed a non-linear behaviour for their carbon/epoxy (AS4/8552) composite fabric tested in the ±45 direction which, according to the authors, could be due to a significant thermal increase during the testing of these materials.

Therefore, it is believed that the CFRP in the present work will also exhibit this trend as the timescale for testing is increased. However some materials, such as the carbon fibre/PEEK in the study of Michel et al. [202], showed a linear behaviour right up to the gigacycle (10^9 cycles) region in the tensile and bending regime for both,

unidirectional and orthotropic lay-ups. Hence, the timescale at which the non-linearity sets in is thought to be material and/or configuration specific.

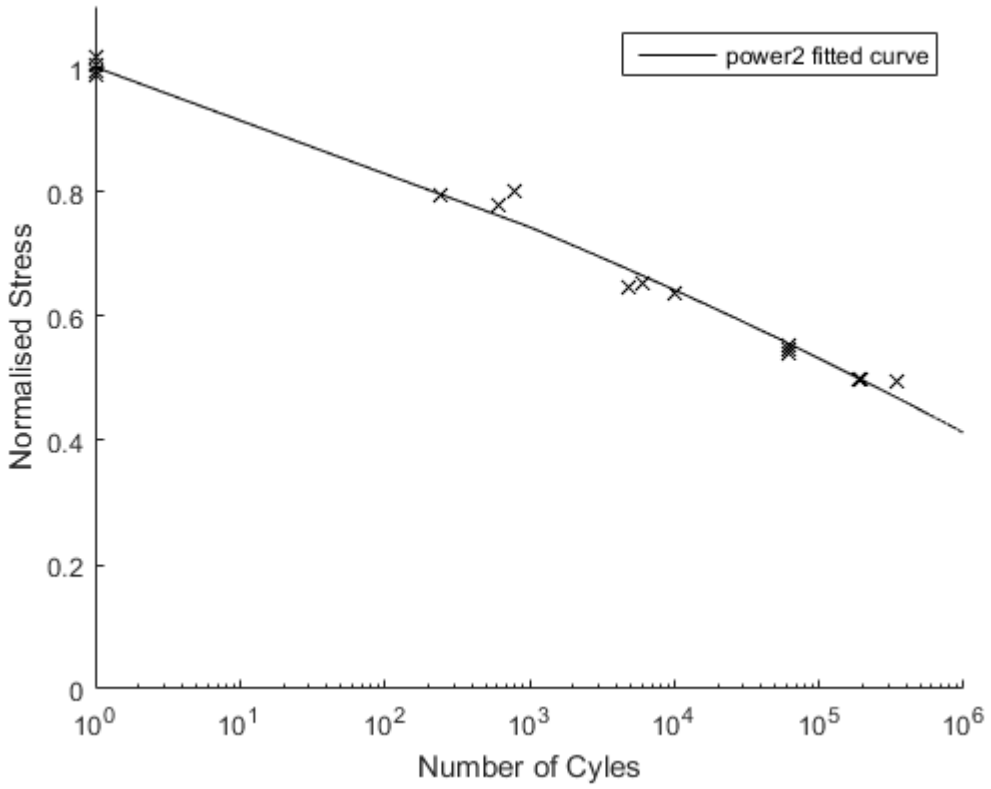

Figure 68 Normalised SN Data

To further compare these results, a fatigue ratio, as defined by Harris et al. [201] and shown in Equation 18 was calculated for the composite in this study.

$$FR = 1 - \left(\beta * \log\left(2 * N_f\right)\right)$$

Equation 18

Where FR = Fatigue ratio; β = slope of the normalised S vs log N curve and N_f = number of cycles (chosen as 10^6 to allow comparison with the materials in the original work).

The slope was calculated by fitting a linear polynomial function between the normalised value of stress and the logarithmic value of cycles to failure. By

substituting the required parameters into Equation 18, the fatigue ratio was calculated and compared with the relevant composites from [201] in Table 35. For the sake of simplicity only materials with 45^0 layers in them are shown in the table. It is seen that the parameters of the composite from the current study are very similar to that of the materials in literature. According to the authors in [201], the calculated slopes showed minimal variation between the materials they had tested despite their being marked differences in all other accepts and, the results from the present work further corroborate their statement.

Table 35 Fatigue Ratio Comparison

Material	**Lay-up**	**Slope** $-\beta$	**Intercept** σ/σ_t	**Fatigue ratio** *FR (at 10^6)*
MTM46/CF6657	$[(\pm 45F)_5]^+$	0.041	1.01	0.74
XAS/913*	$[(\pm 45,0,0)_2]_s$	0.033	0.98	0.79
XAS/914*	$[(\pm 45,0,0)_2]_s$	0.044	1.01	0.72
T800/6376*	$[(\pm 45,0,0)_2]_s$	0.035	1	0.78

+ 5 layers of biaxial non crimp fabric semi-prepreg in ±45 direction

* values taken from [201]

5.5 Summary

From the results and their subsequent analysis, it is seen that the application aerogel/polymer materials either, as a coating or separate (bulk) material has great promise for thermal insulation applications. This is particularly true for requirements where the operating temperature is less than 100°C.

From the materials investigated, it was seen that the aerogel/epoxy composite offers the most promise for such an application. The present work introduces a processing method that does not require the use of any solvents or other hazardous materials to protect the aerogel structure by taking advantage of the changing viscosity of a curing epoxy- hardener combination. This technique was also shown to work in a coating for

a CFRP substrate thus potentially increasing the life of the latter during operation through the reduction of temperatures experienced by the substrate. Although it was not possible to determine the performance of aged composites in the current study due to the aging criteria, which wasn't sufficient to affect the CFRP's fatigue performance, other studies discussed in section 2.1.2.1 show the mechanical degradation of CFRP specimens under elevated temperatures. Therefore, it is thought that the low thermal conductivity coatings in this work could potentially reduce the temperature of the substrate. It is also believed that the FE model of the coated specimens allowed insight into the difference in performance for the types of aerogel/epoxy coatings considered. The study also showed the possibility of using lower extruder speeds to retain the aerogel structure while processing it with a thermoplastic (PA-6) matrix. Additionally, the damage coefficient values defined in this study was used to quantify the aerogel destruction by comparing the composites' thermal conductivities with calculated/theoretical benchmarks.

It is thought the results and findings from the present work could further open the door for a practical and viable use of aerogels as insulating materials. By combing them with a polymer matrix, the fragility of aerogel is negated. As discussed previously, these materials are amongst the best known insulators and their successful incorporation could result in huge energy and economical savings.

However to fully realise the potential of the materials in this study, future studies, as discussed in the next chapter, are required. The infiltration and/or destruction of aerogel is still a concern. When comparing the experimental results with theoretical predictions, it is seen that there is still room for improvement. To illustrate, although the thermal conductivity of the aerogel/epoxy composites in the present study was

measured at 0.20015W/(m*K), theoretically it could be as low as 0.1696W/(m*K) (from sections 4.2.3.4 and 4.2.3.5 respectively).

5.5.1 Comparison with the objectives

In this section, the objectives identified in section 2.9 are evaluated against the findings presented in the current study. Although, the investigation started with possibility of applying YSZ coating onto a CFRP substrate, this method failed perhaps due to the lack of high processing temperatures. Hence, this particular process was not considered further and confined to a section of the discussion. However, the work found more potential in using aerogel as reinforcement in a polymer matrix. Two different binders were used – Nylon 6 (thermoplastic) and epoxy (thermoset) and it was found from the materials investigated that, the aerogel/epoxy composite is the most suitable coating for a CFRP substrate.

For the next objective, it is seen that the damage to the aerogel particles could be limited by using lower extrusion speeds when using a thermoplastic material. The introduction of the aerogel at the 1-hour mark during the cure of the epoxy resin system (used in the current study) is thought to limit its infiltration into the pores of the aerogel and still retain the mouldability of the material. Although certain previous studies in the literature reduced the thermoset resin infiltration by using additional solvents like ethanol, it is believed that they are hazardous especially for large scale processing. Hence the current work looked to limit this by trying to incorporate the aerogel without additional materials (with the exception of a wetting agent). The effect of the wetting agent was negligible on the morphology, cure kinetics and thermal properties tested here but, it is believed that it would increase the interface strength between the aerogel and resin thereby justifying its application. Therefore, the optimal processing conditions for the aerogel/epoxy composites is believed to be

similar to that of sample 1C (in this work) wherein 0.03 mass fraction of aerogel is added after 1 hour into the degassed matrix solution consisting of the epoxy resin, 3% (by weight) wetting agent and hardener.

The optimum processing conditions for both types of aerogel composites were developed through a series of tests and morphological characterisations. The primary property driving the material progression was thermal conductivity which was used to define the damage coefficient of aerogel particles. Additionally, microscopic images were also used to try and visualise this damage. Further properties such as the density, thermal diffusivity, specific heat capacity and optical characteristics for the thermoplastic and/or thermoset binders were also measured for a more comprehensive understanding of the material's structure-property relationship. Since curing is an integral part of thermoset resin application, the cure kinetics of aerogel/epoxy composites were also calculated and modelled.

Finally to satisfy the fourth (and last) objective, a finite element model was built and simulated using the LS-DYNA solver. Although the model used material properties from literature, its thermal performance was similar to the experimental values and thus, used to predict the performance of the coating under a cyclic thermal load. The validated model was also used to investigate single layered coatings to map their performance and put them in perspective with the dual coating system.

6 Conclusion

The present research explored and investigated the possibility of applying thermal coatings onto carbon fibre reinforced plastic (CFRP) substrates. The work initially reviewed the existing literature on thermal coatings by first identifying the limitations of using CFRP and then understating the existing TBC materials along with their benefits and limitations. It was then discovered that these materials may not be suitable for the current substrate and alternate coating materials were explored, amongst which, was aerogel.

To overcome the fragility of aerogels, they were embedded in both, a thermoplastic and a thermoset resin matrix:

- The combination of aerogel with a thermoplastic (PA-6) matrix resulted in a composite with a lower thermal conductivity than the pure polymer sample

    To prepare these samples, aerogel/Nylon-6 (PA-6) composites were mixed using a twin screw extruder and moulded using a compression press with two different speeds in the extruder (along with a pure nylon sample as a control). The lower rpm sample demonstrated improved thermal performance (0.39 W/(mK)) compared to the batch processed using a higher rpm (0.42 W/(mK)). These results were also corroborated with the calculated damage coefficient values. However more research is required to optimise the final moulding process since it is thought that the majority of the aerogel was destroyed in this step. On the other hand, thermoset (epoxy) binders do not require a compression press to reach their final form.

- The thermal conductivity of the aerogel/wetting agent/epoxy system with the aerogel added at 1 hour showed a 13.3% decrease in the thermal conductivity when compared with the pure resin sample

Once the optimum mass fraction of aerogel (3%) was identified, the non-isothermal cure kinetics of the aerogel/epoxy composite with and without a wetting agent was determined. The activation energy and frequency factors showed a higher value for the aerogel composites when compared to the pure resin thereby suggesting an increased viscosity in the former. The results also indicated similarities in the cure kinetic parameters between aerogel/epoxy composites with and without the wetting agent. Additionally, Microscopic, EDX and optical data showed the addition of aerogel at 1 hour as the most promising route for the composite. Since the addition of wetting agent demonstrated a negligible effect in terms of the retention of aerogel particles, its use is advocated due to the potentially increased adhesion between the aerogel and the resin

As the addition of aerogel at the 1 hour mark during the cure of the resin was seen as the most promising route, it, along with another sample (wherein the aerogel was added at the 1.5 hour mark) was applied as a coating onto a CFRP.

- The thermal conductivity results of the aerogel/epoxy/wetting agent coated samples showed a decrease of 41% and 49% wherein the aerogel was added after 1 hour and 1.5 hours respectively when compared with a pure resin coating

Once again, the reflectance spectrum and the thermal conductivity results for the coated samples showed evidence for the existence of the

aerogel particles with limited resin infiltration. The coatings, with different modes of application, were then modelled and simulated using an FE solver. From the simulations, it was seen that the double coating system showed the slowest rate of temperature change and the coating on the bottom surface had the fastest rate of drop. However, the latter showed the highest fluctuations at steady state with the former showing the least. Hence, it is believed that the double coating system would be preferable under cyclic thermal loading conditions since its deviation from the equilibrium temperature is the least. However, if the requirement is to maintain the bottom surface close to the equilibrium under a randomised thermal load, then the use of a bottom coating is advocated as it attains equilibrium faster than the other systems considered.

- Although the present study also considered fatigue performance of coated and uncoated samples after thermal aging them, no discernible inference or conclusion could be derived. This was due to the fact that the uncoated (control) samples showed no difference in fatigue performance with the increasing aging times employed. Hence, it was difficult to infer any effects/changes (if any) due to the coating.

Nevertheless, from the experimental and simulation data presented here, there is potential for applying the described aerogel/epoxy coating onto CFRP substrates. The automotive and aerospace industry where the use of composites is widespread could be a probable area. Additionally, industries where the requirement of thermal insulation from low-medium heat is a requirement (i.e., buildings) can also be considered a potential destination for these materials. Nevertheless the challenge in

using aerogel composites is to find the right balance between the retention of the aerogel structure and its thermal insulation capabilities. This needs to be explored further with the final compromise depending on the specific application.

6.1 Future Work

Although the results in the present work are promising and show potential routes for commercial application, there is always a case for future research and development. A few areas for such improvements are listed here. It must however be noted that this list is by no means exhaustive. Some points for consideration include:

- The development of YSZ coating by exploring alternate methodologies to apply the coating
- An investigation into alternatives to compression moulding for aerogel/PA-6 composites to try and reduce the aerogel destruction is also advocated. This would enable the production of an aerogel/PA-6 composite with superior thermal conductivity and a more efficient thermally insulating material. The use of 3D printers to form the final shape is worth further study.
- The current work modelled the cure kinetics using the Sestak-Beggeren equation [184] which was able to capture the behaviour of the materials adequately. However for a more accurate fit, models such as the one developed by Karkanas & Partridge [203] is worth exploring.
- Viscosity measurements of the resin's cure during the processing of the aerogel/epoxy composites would ensure a more universal solution
- The trend seen in the current paper does show a possibility of using the given processing route in commercial building applications and potentially as a thermal insulation coating on other substrates. It is also believed that a greater decrease in thermal conductivity can be achieved with higher volume fractions

of aerogel; however additional experimental data is needed to confirm this theory.

- Mechanical test data for both the thermoplastic and the thermoset composites would be beneficial in further determining its practical applicability.
- Further research towards an improved model, particularly in the input of actual experimental values as material properties is suggested.
- More research on the fatigue performance and other long term effects (such as the oxidation rates of polyamides [195]) of the substrate and the coating by increasing the aging temperature and/or time.

References

[1] Ganesh Rajput, “Thermal Barrier Coatings Market : Positive Long-Term Growth Outlook by 2024,” *CMFE News*, 2018. .

[2] “Thermal Insulation Coating Market Size, 2018-2025 | Industry Report,” *Grandview Research*, 2017. .

[3] S. Meier, D. Gupta, and K. Sheffler, “Ceramic thermal barrier coatings for commercial gas turbine engines,” *JOM*, vol. 43, no. 3, pp. 50–53, Mar. 1991.

[4] M. G. Hocking, V. Vasantasree, and P. S. Sidky, *Metallic & Ceramic Coatings: Production, High Temperarure Properties & Applications*. Harlow, UK: Longman Scientific & Technical, 1989.

[5] X. Q. Cao, R. Vassen, and D. Stoever, “Ceramic materials for thermal barrier coatings,” *J. Eur. Ceram. Soc.*, vol. 24, no. 1, pp. 1–10, Jan. 2004.

[6] F. Cernuschi, P. Bianchi, M. Leoni, and P. Scardi, “Thermal diffusivity/microstructure relationship in Y-PSZ thermal barrier coatings,” *J. Therm. Spray Technol.*, vol. 8, no. 1, pp. 102–109, Mar. 1999.

[7] J. T. DeMasi-Marcin and D. K. Gupta, “Protective coatings in the gas turbine engine,” *Surf. Coatings Technol.*, vol. 68–69, pp. 1–9, Dec. 1994.

[8] R. A. Miller, “Thermal barrier coatings for aircraft engines: history and directions,” *J. Therm. Spray Technol.*, vol. 6, no. 1, pp. 35–42, Mar. 1997.

[9] D. R. Clarke, M. Oechsner, and N. P. Padture, “Thermal-barrier coatings for more efficient gas-turbine engines,” *MRS Bull*, vol. 37, no. 10, pp. 891–898, 2012.

[10] J. H. Perepezko, “The Hotter the Engine, the Better,” *Science (80-.).*, vol. 326, no. 5956, pp. 1068–1069, Nov. 2009.

[11] E. Fitzer and R. Gadow, “Fiber-reinforced silicon carbide,” *Am. Ceram. Soc.*

Bull., vol. 65, no. 2, pp. 326–335, 1986.

[12] J. D. Buckley, "Carbon-carbon, an overview," *Ceram. Bull.*, vol. 67, no. 2, pp. 364–368, 1988.

[13] T. L. Dhami, O. P. Bahl, and B. R. Awasthy, "Oxidation-Resistant Carbon-Carbon Composites Up To 1700°C," *Carbon N. Y.*, vol. 33, no. 4, pp. 479–490, 1995.

[14] D. Gay and S. V. Hoa, *Composite Materials: Design and Applications*, 2nd ed. Boca Raton, FL: CRC Press, 2007.

[15] C. Peel, "Advances in aerospace materials and structures," in *Aerospace Materials*, B. Cantor, H. Assender, and P. Grant, Eds. Bristol: Institute of Physics Publishing, 2001, p. Chapter 9.

[16] R. Yancey, "Carbon fiber composites: Into the automotive mainstream," 2013. [Online]. Available: http://www.compositesworld.com/columns/carbon-fiber-composites-into-the-automotive-mainstream. [Accessed: 13-Jun-2015].

[17] M. Priestley, "FIA Formula E...Batteries Included," Nov-2014. [Online]. Available: http://f1elvis.com/2014/11/20/fia-formula-e-batteries-included/. [Accessed: 08-Apr-2015].

[18] L. A. Pilato and M. J. Michno, *Advanced Composite Materials*. Berlin Heidelberg: Springer-Verlag, 1994.

[19] B. T. Åström, *Manufacturing of Polymer Composites*. Cheltenham, UK: Nelson Thornes, 1997.

[20] P. J. Walsh, "Carbon Fibers," in *ASM handbook- composites*, vol. 21, D. B. Miracle and S. L. Donaldson, Eds. Materials Park, OH: ASM International, 2001, pp. 35–40.

[21] A. R. Bunsell and J. Renard, *Fundamentals of Fibre Reinforced Composite*

Materials. Bristol; Philadelphia: Institute of Physics Publishing, 2005.

[22] N. Marks, "Polymeric-based composite materials," H. M. Flower, Ed. London: Chapman & Hall, 1995, pp. 205–206.

[23] F. Smeacetto, M. Salvo, and M. Ferraris, "Oxidation protective multilayer coatings for carbon–carbon composites," *Carbon N. Y.*, vol. 40, no. 4, pp. 583–587, 2002.

[24] D. W. McKee, "Oxidation Behaviour and Protection of Carbon/Carbon Composites," *Carbon N. Y.*, vol. 25, no. 4, pp. 551–557, 1987.

[25] F. Smeacetto, M. Ferraris, and M. Salvo, "Multilayer coating with self-sealing properties for carbon–carbon composites," *Carbon N. Y.*, vol. 41, no. 11, pp. 2105–2111, 2003.

[26] M. E. Westwood, J. D. Webster, R. J. Day, F. H. Hayes, and R. Taylor, "Oxidation protection for carbon fibre composites," *J. Mater. Sci.*, vol. 31, no. 6, pp. 1389–1397, Jan. 1996.

[27] A. Vanaja and R. M. V. G. K. Rao, "Fibre Fraction Effects on Thermal Degradation Behaviour of GFRP, CFRP and Hybrid Composites," *J. Reinf. Plast. Compos.*, vol. 21, no. 15, pp. 1389–1398, 2002.

[28] J. Wolfrum, S. Eibl, and L. Lietch, "Rapid evaluation of long-term thermal degradation of carbon fibre epoxy composites," *Compos. Sci. Technol.*, vol. 69, no. 3–4, pp. 523–530, Mar. 2009.

[29] J. Justo, J. C. Marin, F. París, and J. Cañas, "The Effect of Frequency on Fatigue Behaviour of Graphite-Epoxy Composites," in *ECCM16 - 16TH EUROPEAN CONFERENCE ON COMPOSITE MATERIALS*, 2014, pp. 1–8.

[30] T. Naruse, T. Hattori, H. Miura, and K. Takahashi, "Evaluation of thermal degradation of unidirectional CFRP rings," *Compos. Struct.*, vol. 52, no. 3–4,

pp. 533–538, May 2001.

[31] M. Nakada, M. Maeda, T. Hirohata, M. Morita, and Y. Miyano, “Time and temperature dependence on the flexural fatigue strength in the transverse direction of unidirectional CFRP,” in *Proc. SPIE 2921, International Conference on Experimental Mechanics: Advances and Applications*, 1997, vol. 2921, pp. 492–497.

[32] N. P. Padture, M. Gell, and E. H. Jordan, “Thermal barrier coatings for gas-turbine engine applications,” *Science (80-.).*, vol. 296, no. 5566, pp. 280–284, 2002.

[33] D. R. Clarke and S. R. Phillpot, “Thermal barrier coating materials,” *Mater. Today*, vol. 8, no. 6, pp. 22–29, 2005.

[34] U. Schulz, K. Fritscher, and M. Peters, “Thermocyclic Behavior of Variously Stabilized EB-PVD Thermal Barrier Coatings,” in *International Gas Turbine and Aeroengtne Congress & Exhibition*, 1996, pp. 1–7.

[35] M. Peters, C. Leyens, U. Schulz, and W. A. Kaysser, “EB-PVD Thermal Barrier Coatings for Aeroengines and Gas Turbines,” *Adv. Eng. Mater.*, vol. 3, no. 4, pp. 193–204, Apr. 2001.

[36] U. Schulz, B. Saruhan, K. Fritscher, and C. Leyens, “Review on Advanced EB-PVD Ceramic Topcoats for TBC Applications,” *Int. J. Appl. Ceram. Technol.*, vol. 1, no. 4, pp. 302–315, 2004.

[37] A. U. Munawar, U. Schulz, G. Cerri, and H. Lau, “Microstructure and cyclic lifetime of Gd and Dy-containing EB-PVD TBCs deposited as single and double-layer on various bond coats,” *Surf. Coatings Technol.*, vol. 245, pp. 92–101, Apr. 2014.

[38] D. Stöver, G. Pracht, H. Lehmann, M. Dietrich, J.-E. Döring, and R. Vaßen,

"New material concepts for the next generation of plasma-sprayed thermal barrier coatings," *J. Therm. Spray Technol.*, vol. 13, no. 1, pp. 76–83, Mar. 2004.

[39] R. Vaßen, A. Stuke, and D. Stöver, "Recent Developments in the Field of Thermal Barrier Coatings," *J. Therm. Spray Technol.*, vol. 18, no. 2, pp. 181–186, Mar. 2009.

[40] L. Swadźba, G. Moskal, B. Mendala, and T. Gancarczyk, "Characterisation of air plasma sprayed TBC coating during isothermal oxidation at 1100 C," *J. Achiev. Mater. Manuf. Eng.*, vol. 21, no. 2, pp. 81–84, 2007.

[41] M. Saremi, A. Afrasiabi, and A. Kobayashi, "Microstructural analysis of YSZ and YSZ/Al2O3 plasma sprayed thermal barrier coatings after high temperature oxidation," *Surf. Coatings Technol.*, vol. 202, no. 14, pp. 3233–3238, Apr. 2008.

[42] C. H. Lee, H. K. Kim, H. S. Choi, and H. S. Ahn, "Phase transformation and bond coat oxidation behavior of plasma-sprayed zirconia thermal barrier coating," *Surf. Coatings Technol.*, vol. 124, no. 1, pp. 1–12, Feb. 2000.

[43] E. W. Leib, U. Vainio, R. M. Pasquarelli, J. Kus, C. Czaschke, N. Walter, R. Janssen, M. Müller, A. Schreyer, H. Weller, and T. Vossmeyer, "Synthesis and thermal stability of zirconia and yttria-stabilized zirconia microspheres," *J. Colloid Interface Sci.*, vol. 448, pp. 582–592, Jun. 2015.

[44] A. Suresh, M. J. Mayo, W. D. Porter, and C. J. Rawn, "Crystallite and Grain-Size-Dependent Phase Transformations in Yttria-Doped Zirconia," *J. Am. Ceram. Soc.*, vol. 86, no. 2, pp. 360–362, Feb. 2003.

[45] J. Moon, H. Choi, H. Kim, and C. Lee, "The effects of heat treatment on the phase transformation behavior of plasma-sprayed stabilized ZrO2 coatings,"

Surf. Coatings Technol., vol. 155, no. 1, pp. 1–10, Jun. 2002.

[46] H. B. Guo, R. Vaßen, and D. Stöver, "Thermophysical properties and thermal cycling behavior of plasma sprayed thick thermal barrier coatings," *Surf. Coatings Technol.*, vol. 192, no. 1, pp. 48–56, Mar. 2005.

[47] M. P. Schmitt, A. K. Rai, R. Bhattacharya, D. Zhu, and D. E. Wolfe, "Multilayer thermal barrier coating (TBC) architectures utilizing rare earth doped YSZ and rare earth pyrochlores," *Surf. Coatings Technol.*, vol. 251, pp. 56–63, Jul. 2014.

[48] H. Schneider, J. Schreuer, and B. Hildmann, "Structure and properties of mullite—A review," *J. Eur. Ceram. Soc.*, vol. 28, no. 2, pp. 329–344, 2008.

[49] H. Jian-Feng, Z. Xie-Rong, L. He-Jun, X. Xin-Bo, and H. Min, "Mullite-Al2O3-SiC oxidation protective coating for carbon/carbon composites," *Carbon N. Y.*, vol. 41, no. 14, pp. 2825–2829, 2003.

[50] R. Vassen, X. Cao, F. Tietz, D. Basu, and D. Stöver, "Zirconates as New Materials for Thermal Barrier Coatings," *J. Am. Ceram. Soc.*, vol. 83, no. 8, pp. 2023–2028, Aug. 2000.

[51] W. Ma, D. E. Mack, R. Vaßen, and D. Stöver, "Perovskite-Type Strontium Zirconate as a New Material for Thermal Barrier Coatings," *J. Am. Ceram. Soc.*, vol. 91, no. 8, pp. 2630–2635, Aug. 2008.

[52] W. Ma, M. O. Jarligo, D. E. Mack, D. Pitzer, J. Malzbender, R. Vaßen, and D. Stöver, "New Generation Perovskite Thermal Barrier Coating Materials," *J. Therm. Spray Technol.*, vol. 17, no. 5–6, pp. 831–837, Nov. 2008.

[53] T. Maekawa, K. Kurosaki, and S. Yamanaka, "Thermal and mechanical properties of perovskite-type barium hafnate," *J. Alloys Compd.*, vol. 407, no. 1–2, pp. 44–48, Jan. 2006.

[54] S. Yamanaka, T. Maekawa, H. Muta, T. Matsuda, S. Kobayashi, and K. Kurosaki, “Thermophysical properties of SrHfO3 and SrRuO3,” *J. Solid State Chem.*, vol. 177, no. 10, pp. 3484–3489, Oct. 2004.

[55] S. Yamanaka, K. Kurosaki, T. Maekawa, T. Matsuda, S. Kobayashi, and M. Uno, “Thermochemical and thermophysical properties of alkaline-earth perovskites,” *J. Nucl. Mater.*, vol. 344, no. 1–3, pp. 61–66, Sep. 2005.

[56] W. Ma, P. Li, H. Dong, Y. Bai, J. Zhao, and X. Fan, “Y2O3 and Yb2O3 Co-doped Strontium Hafnate as a New Thermal Barrier Coating Material,” *J. Therm. Spray Technol.*, vol. 23, no. 1–2, pp. 154–159, 2014.

[57] S. Yamanaka, T. Hamaguchi, T. Oyama, T. Matsuda, S. Kobayashi, and K. Kurosaki, “Heat capacities and thermal conductivities of perovskite type BaZrO3 and BaCeO3,” *J. Alloys Compd.*, vol. 359, no. 1–2, pp. 1–4, Sep. 2003.

[58] S. Yamanaka, M. Fujikane, T. Hamaguchi, H. Muta, T. Oyama, T. Matsuda, S. Kobayashi, and K. Kurosaki, “Thermophysical properties of BaZrO3 and BaCeO3,” *J. Alloys Compd.*, vol. 359, no. 1–2, pp. 109–113, Sep. 2003.

[59] M. O. Jarligo, D. E. Mack, R. Vassen, and D. Stöver, “Application of Plasma-Sprayed Complex Perovskites as Thermal Barrier Coatings,” *J. Therm. Spray Technol.*, vol. 18, no. 2, pp. 187–193, Mar. 2009.

[60] N. Schlegel, D. Sebold, Y. J. Sohn, G. Mauer, and R. Vaßen, “Cycling Performance of a Columnar-Structured Complex Perovskite in a Temperature Gradient Test,” *J. Therm. Spray Technol.*, pp. 1–8, Jun. 2015.

[61] R. Vaßen, M. O. Jarligo, T. Steinke, D. E. Mack, and D. Stöver, “Overview on advanced thermal barrier coatings,” *Surf. Coatings Technol.*, vol. 205, no. 4, pp. 938–942, Nov. 2010.

[62] R. Subramanian, “Thermal barrier coating having high phase stability,” US 6258467 B1, 2001.

[63] M. J. Maloney, “Thermal barrier coating systems and materials,” 6117560, 2000.

[64] X. Q. Cao, R. Vassen, W. Jungen, S. Schwartz, F. Tietz, and D. Stöver, “Thermal Stability of Lanthanum Zirconate Plasma-Sprayed Coating,” *J. Am. Ceram. Soc.*, vol. 84, no. 9, pp. 2086–2090, Sep. 2001.

[65] H. Lehmann, D. Pitzer, G. Pracht, R. Vassen, and D. Stöver, “Thermal Conductivity and Thermal Expansion Coefficients of the Lanthanum Rare-Earth-Element Zirconate System,” *J. Am. Ceram. Soc.*, vol. 86, no. 8, pp. 1338–1344, Aug. 2003.

[66] Z.-G. Liu, W.-H. Zhang, J.-H. Ouyang, and Y. Zhou, “Novel thermal barrier coatings based on rare-earth zirconates/YSZ double-ceramic-layer system deposited by plasma spraying,” *J. Alloys Compd.*, vol. 647, pp. 438–444, Oct. 2015.

[67] W. Ma, S. Gong, H. Xu, and X. Cao, “The thermal cycling behavior of Lanthanum–Cerium Oxide thermal barrier coating prepared by EB–PVD,” *Surf. Coatings Technol.*, vol. 200, no. 16–17, pp. 5113–5118, Apr. 2006.

[68] W. Ma, Y. Ma, S. K. Gong, H. Bin Xu, and X. Q. Cao, “Thermal Cycling Behavior of Lanthanum-Cerium Oxide Thermal Barrier Coatings Prepared by Air Plasma Spraying,” *Key Eng. Mater.*, vol. 336–338, pp. 1759–1761, 2007.

[69] J. Wu, X. Wei, N. P. Padture, P. G. Klemens, M. Gell, E. García, P. Miranzo, and M. I. Osendi, “Low-Thermal-Conductivity Rare-Earth Zirconates for Potential Thermal-Barrier-Coating Applications,” *J. Am. Ceram. Soc.*, vol. 85, no. 12, pp. 3031–3035, Dec. 2002.

[70] N. P. Bansal and D. Zhu, “Effects of doping on thermal conductivity of pyrochlore oxides for advanced thermal barrier coatings,” *Mater. Sci. Eng. A*, vol. 459, no. 1–2, pp. 192–195, Jun. 2007.

[71] J. Feng, B. Xiao, R. Zhou, and W. Pan, “Thermal expansions of Ln2Zr2O7 (Ln = La, Nd, Sm, and Gd) pyrochlore,” *J. Appl. Phys.*, vol. 111, no. 10, p. 103535, May 2012.

[72] R. Vaßen, F. Traeger, and D. Stöver, “New Thermal Barrier Coatings Based on Pyrochlore/YSZ Double-Layer Systems,” *Int. J. Appl. Ceram. Technol.*, vol. 1, no. 4, pp. 351–361, Oct. 2004.

[73] W. Ma, H. Dong, H. Guo, S. Gong, and X. Zheng, “Thermal cycling behavior of La2Ce2O7/8YSZ double-ceramic-layer thermal barrier coatings prepared by atmospheric plasma spraying,” *Surf. Coatings Technol.*, vol. 204, no. 21–22, pp. 3366–3370, Aug. 2010.

[74] S. Zhao, L. Gu, Y. Zhao, W. Huang, L. Zhu, X. Fan, B. Zou, and X. Cao, “Thermal cycling behavior and failure mechanism of La2(Zr0.7Ce0.3)2O7/Eu3+-doped 8YSZ thermal barrier coating prepared by atmospheric plasma spraying,” *J. Alloys Compd.*, vol. 580, pp. 101–107, Dec. 2013.

[75] X. Q. Cao, R. Vassen, F. Tietz, and D. Stoever, “New double-ceramic-layer thermal barrier coatings based on zirconia–rare earth composite oxides,” *J. Eur. Ceram. Soc.*, vol. 26, no. 3, pp. 247–251, 2006.

[76] Z. H. Xu, L. M. He, R. D. Mu, S. M. He, G. H. Huang, and X. Q. Cao, “Double-ceramic-layer thermal barrier coatings based on La2(Zr0.7Ce0.3)2O7/La2Ce2O7 deposited by electron beam-physical vapor deposition,” *Appl. Surf. Sci.*, vol. 256, no. 11, pp. 3661–3668, Mar. 2010.

[77] S. Zhao, Y. Zhao, B. Zou, X. Fan, J. Xu, Y. Hui, X. Zhou, S. Liu, and X. Cao, "Characterization and thermal cycling behavior of La2(Zr0.7Ce0.3)2O7/8YSZ functionally graded thermal barrier coating prepared by atmospheric plasma spraying," *J. Alloys Compd.*, vol. 592, pp. 109–114, Apr. 2014.

[78] B. R. Marple, J. Voyer, M. Thibodeau, D. R. Nagy, and R. Vassen, "Hot Corrosion of Lanthanum Zirconate and Partially Stabilized Zirconia Thermal Barrier Coatings," *J. Eng. Gas Turbines Power*, vol. 128, no. 1, pp. 144–152, 2006.

[79] L. Haoran, W. Chang-An, Z. Chenguang, and T. Shuyan, "Thermo-physical properties of rare-earth hexaaluminates LnMgAl11O19 (Ln: La, Pr, Nd, Sm, Eu and Gd) magnetoplumbite for advanced thermal barrier coatings," *J. Eur. Ceram. Soc.*, vol. 35, no. 4, pp. 1297–1306, Apr. 2015.

[80] X. Xie, H. Guo, S. Gong, and H. Xu, "Thermal cycling behavior and failure mechanism of LaTi2Al9O19/YSZ thermal barrier coatings exposed to gas flame," *Surf. Coatings Technol.*, vol. 205, no. 17–18, pp. 4291–4298, May 2011.

[81] D. A. Stewart, D. B. Leiser, R. R. DiFiore, and V. W. Katvala, "High efficiency tantalum-based ceramic composite structures," Aug. 2010.

[82] B. A. Nagaraj, J. F. Ackerman, W. R. Stowell, and C.-P. Lee, "Thermal barrier coating protected by tantalum oxide and method for preparing same," US 6933066 B2, 2005.

[83] B. S. Tryon, D. A. Litton, B. J. Zimmerman, and R. A. Beers, "Multi-layer metallic coating for TBC systems," US 8497028 B1, 2013.

[84] S. Bose, "Thermal Barrier Coatings (TBCs)," in *High Temperature Coatings*, Oxford: Butterworth-Heinemann, 2007, p. Chapter 7.

[85] H. E. Eaton, J. R. Linsey, and R. B. Dinwiddie, “The Effect of Thermal Aging on the Thermal Conductivity of Plasma Sprayed Fully Stabilized Zirconia,” in *Thermal Conductivity 22*, T. W. Tong, Ed. Lancaster, PA: Technomic, 1994, pp. 289–301.

[86] G. Mauer and R. Vaßen, “Current developments and challenges in thermal barrier coatings,” *Surf. Eng.*, vol. 27, no. 7, pp. 477–479, Aug. 2011.

[87] J. S. Subramanian, A. S. Praveen, J. Sarangan, S. Suresh, and S. Raghuraman, “Microstructure and Characterization of Thermal sprayed Ni-Cr/Al2O3 coating,” *Int. J. ChemTech Res.*, vol. 6, no. 3, pp. 1948–1951, 2014.

[88] A. Feuerstein, J. Knapp, T. Taylor, A. Ashary, A. Bolcavage, and N. Hitchman, “Technical and Economical Aspects of Current Thermal Barrier Coating Systems for Gas Turbine Engines by Thermal Spray and EBPVD: A Review,” *J. Therm. Spray Technol.*, vol. 17, no. 2, pp. 199–213, Feb. 2008.

[89] A. Jadhav, N. Padture, E. Jordan, M. Gell, P. Miranzo, and E. Fullerjr, “Low-thermal-conductivity plasma-sprayed thermal barrier coatings with engineered microstructures,” *Acta Mater.*, vol. 54, no. 12, pp. 3343–3349, Jul. 2006.

[90] N. P. Padture, K. W. Schlichting, T. Bhatia, A. Ozturk, B. Cetegen, E. H. Jordan, M. Gell, S. Jiang, T. D. Xiao, P. R. Strutt, E. García, P. Miranzo, and M. I. Osendi, “Towards durable thermal barrier coatings with novel microstructures deposited by solution-precursor plasma spray,” *Acta Mater.*, vol. 49, no. 12, pp. 2251–2257, Jul. 2001.

[91] D. V. Rigney, A. F. Maricocchi, D. J. Wortman, R. W. Bruce, and J. D. Rigney, “Method of forming a thermal barrier coating system,” US 6447854 B1, 2002.

[92] M. Belmonte, “Advanced Ceramic Materials for High Temperature

Applications," *Adv. Eng. Mater.*, vol. 8, no. 8, pp. 693–703, Aug. 2006.

[93] M. F. J. Koolloos and G. Marijnissen, "Burner rig testing of 'herringbone' EB-PVD Thermal Barrier Coatings," 2002.

[94] J. R. Davis, Ed., "General Information," in *Metals Handbook: Desk Edition*, 2nd ed., Materials Park, OH: ASM International, 1998, p. 65.

[95] B. K. Kandola, W. Bhatti, and E. Kandare, "A comparative study on the efficacy of varied surface coatings in fireproofing glass/epoxy composites," *Polym. Degrad. Stab.*, vol. 97, no. 11, pp. 2418–2427, Nov. 2012.

[96] P. Luangtriratana, B. K. Kandola, and P. Myler, "Ceramic particulate thermal barrier surface coatings for glass fibre-reinforced epoxy composites," *Mater. Des.*, vol. 68, pp. 232–244, Mar. 2015.

[97] S. Bourbigot, P. Bachelet, F. Samyn, M. Jimenez, and S. Duquesne, "Intumescence as method for providing fire resistance to structural composites: application to poly(ethylene terephtalate) foam sandwich–structured composite," *Compos. Interfaces*, vol. 20, no. 4, pp. 269–277, Jun. 2013.

[98] B. K. Kandola and P. Luangtriratana, "Evaluation of thermal barrier effect of ceramic microparticulate surface coatings on glass fibre-reinforced epoxy composites," *Compos. Part B Eng.*, vol. 66, pp. 381–387, Nov. 2014.

[99] "Zircotec Group." [Online]. Available: https://www.zircotec.com/. [Accessed: 05-Jun-2018].

[100] T. C. Prentice, "Article and a method of making an article," US 2014/0072799 A1, 2014.

[101] T. C. Prentice, "Article, an intermediate product, and a method of making an article," US 2012/0114915 A1, 2012.

[102] W. Huang, H. Cheng, and Y. Zhou, "Oxidation behavior of plasma-sprayed

stabilized zirconia/Al coated polymer matrix composites," *RSC Adv.*, vol. 5, no. 88, pp. 72331–72339, Aug. 2015.

[103] Y. Hao, F. Liu, and E.-H. Han, "Mechanical and Barrier Properties of Epoxy/Ultra-short Glass Fibers Composite Coatings," *J. Mater. Sci. Technol.*, vol. 28, no. 12, pp. 1077–1084, Dec. 2012.

[104] M. Vahtrus, S. Oras, M. Antsov, V. Reedo, U. Mäeorg, A. Lõhmus, K. Saal, and R. Lõhmus, "Mechanical and thermal properties of epoxy composite thermal insulators filled with silica aerogel and hollow glass microspheres," *Proc. Est. Acad. Sci.*, vol. 66, no. 4, pp. 339–346, 2017.

[105] K. C. Yung, B. L. Zhu, T. M. Yue, and C. S. Xie, "Preparation and properties of hollow glass microsphere-filled epoxy-matrix composites," *Compos. Sci. Technol.*, vol. 69, no. 2, pp. 260–264, 2009.

[106] B. Zhu, J. Ma, J. Wang, J. Wu, and D. Peng, "Thermal, dielectric and compressive properties of hollow glass microsphere filled epoxy-matrix composites," *J. Reinf. Plast. Compos.*, vol. 31, no. 19, pp. 1311–1326, 2012.

[107] A. Rahaman, M. Imran, and S. Pal, "A Review on Epoxy Composites using Hollow Glass Microspheres and Nanoreinforcements," *J. Chem. Pharm. Sci.*, no. Special Issue 3, pp. 23–30, 2016.

[108] A. Paul, D. D. Jayaseelan, S. Venugopal, E. Zapata-Solvas, J. G. P. Binner, B. Vaidhyanathan, A. Heaton, P. Brown, and W. E. Lee, "UHTC composites for hypersonic applications," *Am. Ceram. Soc. Bull.*, vol. 91, no. 1, pp. 22–29, 2012.

[109] E. Wuchina, E. Opila, M. Opeka, W. Fahrenholtz, and I. Talmy, "UHTCs: ultra-high temperature ceramic materials for extreme environment applications," *Electrochem. Soc. Interface*, vol. 16, no. 4, pp. 30–36, 2007.

[110] S. Shimada, “A thermoanalytical study on the oxidation of ZrC and HfC powders with formation of carbon,” *Solid state ionics*, vol. 149, no. 3, pp. 319–326, 2002.

[111] J. Xie, K. Li, H. Li, Q. Fu, and L. Guo, “Ablation behavior and mechanism of C/C–ZrC–SiC composites under an oxyacetylene torch at 3000 °C,” *Ceram. Int.*, vol. 39, no. 4, pp. 4171–4178, May 2013.

[112] M. Koebel, A. Rigacci, and P. Achard, “Aerogel-based thermal superinsulation: An overview,” *J. Sol-Gel Sci. Technol.*, vol. 63, no. 3, pp. 315–339, 2012.

[113] J. Stergar and U. Maver, “Review of aerogel-based materials in biomedical applications,” *J. Sol-Gel Sci. Technol.*, vol. 77, no. 3, pp. 738–752, Mar. 2016.

[114] S. S. Kistler, “Coherent Expanded Aerogels and Jellies,” *Nature*, vol. 127, no. 3211, p. 741, 1931.

[115] N. Gupta and W. Ricci, “Processing and compressive properties of aerogel/epoxy composites,” *J. Mater. Process. Technol.*, vol. 198, no. 1–3, pp. 178–182, Mar. 2008.

[116] J. Koravos, C. Norwood, P. Pescatore, and J. Pidhurney, “Aerogel Insulative Coatings: New Coating Technology Offers Personnel Protection,” *Paint and Coatings Industry*, 2013. [Online]. Available: http://www.pcimag.com/articles/98016-aerogel-insulative-coatings. [Accessed: 12-Feb-2016].

[117] A. Soleimani Dorcheh and M. H. Abbasi, “Silica aerogel; synthesis, properties and characterization,” *J. Mater. Process. Technol.*, vol. 199, no. 1–3, pp. 10–26, Apr. 2008.

[118] G. S. Kim and S. H. Hyun, “Effect of mixing on thermal and mechanical

properties of aerogel-PVB composites," *J. Mater. Sci.*, vol. 38, no. 9, pp. 1961–1966, 2003.

[119] N. Mazlan and T. C. Khoon, "Assessment on the Compressive Strength Behavior of Hybrid Filled Epoxy Nanocomposite," *J. Teknol.*, vol. 76, no. 10, p. 91:95, 2015.

[120] P. C. Thapliyal and K. Singh, "Aerogels as Promising Thermal Insulating Materials: An Overview," *J. Mater.*, vol. 2014, p. 10, 2014.

[121] R. Baetens, B. Petter Jelle, and A. Gustavsen, "Aerogel insulation for building applications: A state-of-the-art review," *Energy Build.*, vol. 43, no. 4, pp. 761–769, 2011.

[122] A. Du, B. Zhou, Z. Zhang, and J. Shen, "A Special Material or a New State of Matter: A Review and Reconsideration of the Aerogel," *Mater. (Basel, Switzerland)*, vol. 6, no. 3, pp. 941–968, Mar. 2013.

[123] L. W. Hrubesh, "Aerogel applications," *J. Non. Cryst. Solids*, vol. 225, pp. 335–342, 1998.

[124] M. Ibrahim, P. H. Biwole, E. Wurtz, and P. Achard, "A study on the thermal performance of exterior walls covered with a recently patented silica-aerogel-based insulating coating," *Build. Environ.*, vol. 81, pp. 112–122, Nov. 2014.

[125] A. Shaid, L. Wang, and R. Padhye, "The thermal protection and comfort properties of aerogel and PCM-coated fabric for firefighter garment," *J. Ind. Text.*, vol. 45, no. 4, pp. 611–625, Jan. 2016.

[126] M. A. B. Meador, E. F. Fabrizio, F. Ilhan, A. Dass, G. Zhang, P. Vassilaras, J. C. Johnston, and N. Leventis, "Cross-linking Amine-Modified Silica Aerogels with Epoxies: Mechanically Strong Lightweight Porous Materials," *Chem. Mater.*, vol. 17, no. 5, pp. 1085–1098, Mar. 2005.

[127] T.-Y. Wei, S.-Y. Lu, and Y.-C. Chang, “Transparent, Hydrophobic Composite Aerogels with High Mechanical Strength and Low High-Temperature Thermal Conductivities,” *J. Phys. Chem. B*, vol. 112, no. 38, pp. 11881–11886, Sep. 2008.

[128] M. Schmidt and F. Schwertfeger, “Applications for silica aerogel products,” *J. Non. Cryst. Solids*, vol. 225, pp. 364–368, 1998.

[129] M. Mielke and K.-H. von Dungen, “Moldings containing silica aerogel particles and their preparation,” 5656195, 1997.

[130] V. Vo, M. I. Maurer, F. Bunge, and H. H. Merkel, “Thermally insulating polymer foam/aerogel composite articles,” US 2012/0112117 A1, 2012.

[131] M. K. Williams, T. M. Smith, J. E. Fesmire, L. B. Roberson, and L. M. Clayton, “Aerogel/polymer composite materials,” US 7790787 B2, 2010.

[132] M. S. M. Basri, N. Mazlan, and F. Mustapha, “Effects of stirring speed and time on water absorption performance of silica aerogel/epoxy nanocomposite,” *ARPN J. Eng. Appl. Sci.*, vol. 10, no. 21, pp. 9982–9991, 2015.

[133] J. P. Zhao, D. T. Ge, S. L. Zhang, and X. L. Wei, “Studies on Thermal Property of Silica Aerogel/Epoxy Composite,” *Mater. Sci. Forum*, vol. 546–549, pp. 1581–1584, 2007.

[134] S. Achar and L. J. Procopio, “Developments in waterborne thermal insulation coatings,” *J. Prot. Coatings Linings*, vol. 30, no. 3, pp. 48–59, 2013.

[135] S. Y. Kim, Y. J. Noh, J. Lim, and N.-H. You, “Silica aerogel/polyimide composites with preserved aerogel pores using multi-step curing,” *Macromol. Res.*, vol. 22, no. 1, pp. 108–111, Jan. 2014.

[136] H. M. Kim, H. S. Kim, S. Y. Kim, and J. R. Youn, “Silica aerogel/epoxy composites with preserved aerogel pores and low thermal conductivity,” *e-*

Polymers, vol. 15, no. 2, pp. 111–117, Jan. 2015.

[137] K. Maghsoudi and S. Motahari, "Mechanical, thermal, and hydrophobic properties of silica aerogel-epoxy composites," *J. Appl. Polym. Sci.*, vol. 135, no. 3, p. 45706, Jan. 2018.

[138] D. Ge, L. Yang, Y. Li, and J. Zhao, "Hydrophobic and thermal insulation properties of silica aerogel/epoxy composite," *J. Non. Cryst. Solids*, vol. 355, no. 52–54, pp. 2610–2615, Dec. 2009.

[139] S. Kiil, "Quantitative analysis of silica aerogel-based thermal insulation coatings," *Prog. Org. Coatings*, vol. 89, pp. 26–34, Dec. 2015.

[140] G. Armstrong, "Composite Coating Developments," *Aerospace Manufacturing*, pp. 24–26, Nov-2010.

[141] M. Hayaty, M. H. Beheshty, and M. Esfandeh, "Isothermal differential scanning calorimetry study of a glass/epoxy prepreg," *Polym. Adv. Technol.*, vol. 22, no. 6, pp. 1001–1006, 2011.

[142] S. Montserrat and J. Malek, "A kinetic analysis of the curing reaction of an epoxy resin," *Thermochim. Acta*, vol. 228, no. C, pp. 47–60, 1993.

[143] J. Gonis, G. P. Simon, and W. D. Cook, "Cure properties of epoxies with varying chain length as studied by DSC," *J. Appl. Polym. Sci.*, vol. 72, no. 11, pp. 1479–1488, 1999.

[144] D. Roçu, C. N. Caçcaval, F. Mustaça, and C. Ciobanu, "Cure kinetics of epoxy resins studied by non isothermal DSC data," *Thermochim. Acta*, vol. 383, pp. 119–127, 2002.

[145] N. Sbirrazzuoli and S. Vyazovkin, "Learning about epoxy cure mechanisms from isoconversional analysis of DSC data," *Thermochim. Acta*, vol. 388, no. 1–2, pp. 289–298, 2002.

[146] M. J. Yoo, S. H. Kim, S. D. Park, W. S. Lee, J. W. Sun, J. H. Choi, and S. Nahm, "Investigation of curing kinetics of various cycloaliphatic epoxy resins using dynamic thermal analysis," *Eur. Polym. J.*, vol. 46, no. 5, pp. 1158–1162, 2010.

[147] N. El-Thaher, T. Mekonnen, P. Mussone, D. Bressler, and P. Choi, "Nonisothermal DSC study of epoxy resins cured with hydrolyzed specified risk material," *Ind. Eng. Chem. Res.*, vol. 52, no. 24, pp. 8189–8199, 2013.

[148] I.-K. Hong and S. Lee, "Cure kinetics and modeling the reaction of silicone rubber," *J. Ind. Eng. Chem.*, vol. 19, no. 1, pp. 42–47, 2013.

[149] S. Zhai, P. Zhang, Y. Xian, J. Zeng, and B. Shi, "Effective thermal conductivity of polymer composites: Theoretical models and simulation models," *Int. J. Heat Mass Transf.*, vol. 117, pp. 358–374, Feb. 2018.

[150] K. Bakker, "Using the finite element method to compute the influence of complex porosity and inclusion structures on the thermal and electrical conductivity," *Int. J. Heat Mass Transf.*, vol. 40, no. 15, pp. 3503–3511, Oct. 1997.

[151] B. Mortazavi, M. Baniassadi, J. Bardon, and S. Ahzi, "Modeling of two-phase random composite materials by finite element, Mori-Tanaka and strong contrast methods," *Compos. Part B Eng.*, vol. 45, no. 1, pp. 1117–1125, 2013.

[152] I. Tsekmes, R. Kochetov, P. Morshuis, and J. Smit, "Modeling the thermal conductivity of polymeric composites based on experimental observations," *IEEE Trans. Dielectr. Electr. Insul.*, vol. 21, no. 2, pp. 412–423, 2014.

[153] Y. Liao, X. Wu, H. Liu, and Y. Chen, "Thermal conductivity of powder silica hollow spheres," *Thermochim. Acta*, vol. 526, no. 1–2, pp. 178–184, Nov. 2011.

[154] J. Z. Liang and F. H. Li, “Simulation of heat transfer in hollow-glass-bead-filled polypropylene composites by finite element method,” *Polym. Test.*, vol. 26, no. 3, pp. 419–424, May 2007.

[155] C. Rauwendaal, *Polymer Extrusion*. Munich: Carl Hanser Verlag, 1986.

[156] M. Ivankovic, I. Brnardic, H. Ivankovic, and H. J. Mencer, “DSC study of the cure kinetics during nanocomposite formation: Epoxy/poly(oxypropylene) diamine/organically modified montmorillonite system,” *J. Appl. Polym. Sci.*, vol. 99, pp. 550–557, 2006.

[157] N. Poisson, G. Lachenal, and H. Sautereau, “Near-and mid-infrared spectroscopy studies of an epoxy reactive system,” *Vib. Spectrosc.*, vol. 12, pp. 237–247, 1996.

[158] Centre for Disease Control and Prevention, “ETHANOL (ANHYDROUS) - International Chemical Safety Cards - NIOSH,” *National Institute for Occupational Safety and Health (NIOSH)*, 2014. [Online]. Available: https://www.cdc.gov/niosh/ipcsneng/neng0044.html. [Accessed: 31-Jan-2018].

[159] United States Department of Labor, “Green Job Hazards: Biofuels,” *Occupational Safety & Health Administration* . [Online]. Available: https://www.osha.gov/dep/greenjobs/biofuels.html. [Accessed: 31-Jan-2018].

[160] PRF Composites, “Epoxy Resin System RS-L135,” *Product Data Sheet*, 2013. [Online]. Available: http://www.prfcomposites.com/store/image/data/PDF/RS-L135.pdf. [Accessed: 22-Dec-2016].

[161] D. Halliday, R. Resnick, and J. Walker, *Fundamentals of physics*, 7th ed. Hoboken, NJ: Wiley, 2005.

[162] M. J. O’neill, “Measurement of Specific Heat Functions by Differential Scanning Calorimetry.,” *Anal. Chem.*, vol. 38, no. 10, pp. 1331–1336, 1966.

[163] Thermal Wave Imaging Inc., “ThermoScope® II: Advanced Thermography for In-Service Inspection.” [Online]. Available: http://www.thermalwave.com/1/376/thermoscope_ii.asp. [Accessed: 16-Nov-2016].

[164] Y. A. Çengel, *Introduction to Thermodynamics and Heat Transfer*. New York: McGraw-Hill, 1997.

[165] ASM Committee on Forms and Properties of Composite Materials, “High-Strength Medium-Temperature Thermoset Matrix Composites,” in *Engineered Materials Handbook: Volume 1*, ASM International Handbook Committee, Ed. Ohio: ASM International, 1987.

[166] Cabot Corporation, “Enova Aerogel Fine Particles,” *Safety Data Sheet*, 2012. [Online]. Available: http://www.buyaerogel.com/wp-content/uploads/2014/02/NGFPA-EUR-EN.pdf. [Accessed: 08-Aug-2016].

[167] PRF Composites, “Ultra Low Viscosity Epoxy Resin System RS-M135,” *Product Data Sheet*, 2013. [Online]. Available: http://www.prfcomposites.com/store/image/data/PDF/RS-M135.pdf. [Accessed: 13-Oct-2017].

[168] Active Space Technologies, “Aerogels – Product Datsheet at Active Space Technologies,” *The Future of Thermal Insulation for Space Applications*, 2011. [Online]. Available: http://esther.ist.utl.pt/pages/yurisnight2011/ActiveSpaceTech.pdf. [Accessed: 02-Feb-2018].

[169] A. B. Shapiro, “Heat Transfer in LS-DYNA,” in *4th European LS-DYNA Users Conference*, 2003, p. H-I01-08.

[170] Tobias Erhart, “Review of Solid Element Formulations in LS-DYNA,”

Entwicklerforum, 2011. [Online]. Available: https://www.dynamore.de/de/download/papers/forum11/entwicklerforum-2011/erhart.pdf. [Accessed: 06-Feb-2018].

[171] LSTC, *LS-DYNA® Keyword user's Manual I– version R8.0*, vol. I. 2015.

[172] S. Krishnaswamy, L. Tinsley, V. Marchante, S. Addepalli, Z. Huang, and H. Abhyankar, "Effect of extrusion and compression moulding on the thermal properties of nylon-6/silica aerogel composites," *J. Thermoplast. Compos. Mater.*, vol. 31, no. 7, pp. 992–1009, 2018.

[173] "Durethan B30 S 000000 Data Sheet," 2016. [Online]. Available: https://techcenter.lanxess.com/scp/emea/en/products/type/datasheet.jsp?ref=&gid=9413&pid=47. [Accessed: 04-Sep-2016].

[174] S. Shepard, "Automated binary processing of thermographic sequence data," US 8449176 B2, 2013.

[175] Durethan B 30 S 000000, "Safety Data Sheet." Lanxess Corporation, 2012.

[176] S. V. Levchik, G. F. Levchik, A. I. Balabanovich, G. Camino, and L. Costa, "Mechanistic study of combustion performance and thermal decomposition behaviour of nylon 6 with added halogen-free fire retardants," *Polym. Degrad. Stab.*, vol. 54, no. 2, pp. 217–222, Nov. 1996.

[177] D. A. Ditmars, S. Ishihara, S. S. Chang, G. Bernstein, and E. D. West, "Enthalpy and heat-capacity standard reference material: synthetic sapphire (a-Al2O3) from 10 to 2250 K," *J. Res. Natl. Bur. Stand. (1934).*, vol. 87, no. 2, pp. 159–163, 1982.

[178] R. L. Hamilton and O. K. Crosser, "Thermal conductivity of heterogeneous two-component systems," *Ind. Eng. Chem. Fundam.*, vol. 1, no. 3, pp. 187–191, 1962.

[179] “BuyAerogel.com | Enova® Aerogel IC3110 Particles.” [Online]. Available: http://www.buyaerogel.com/product/enova-aerogel-ic3110/. [Accessed: 08-Aug-2016].

[180] “Silica-Silicon Dioxide (SiO2) properties.” [Online]. Available: http://www.azom.com/properties.aspx?ArticleID=1114. [Accessed: 29-Sep-2016].

[181] S. Krishnaswamy, V. Marchante, H. Abhyankar, Z. Huang, and J. Brighton, “Non Isothermal cure kinetics of Aerogel/Epoxy composites using Differential Scanning Calorimetry,” *Polym. Technol. Mater.*, 2019.

[182] H. E. Kissinger, “Reaction Kinetics in Differential Thermal Analysis,” *Anal. Chem.*, vol. 29, no. 11, pp. 1702–1706, 1957.

[183] S. H. Nordeng, “Determination of Activation Energy and Frequency Factor for Samples of the Bakken Formation (Miss . – Dev .): Williston Basin , ND,” *North Dakota Geol. Surv.*, no. 163, pp. 1–15, 2012.

[184] J. Šesták and G. Berggren, “Study of the kinetics of the mechanism of solid-state reactions at increasing temperatures,” *Thermochim. Acta*, vol. 3, no. 1, pp. 1–12, 1971.

[185] L. A. Pérez-Maqueda, J. M. Criado, and P. E. Sánchez-Jiménez, “Combined kinetic analysis of solid-state reactions: A powerful tool for the simultaneous determination of kinetic parameters and the kinetic model without previous assumptions on the reaction mechanism,” *J. Phys. Chem. A*, vol. 110, no. 45, pp. 12456–12462, 2006.

[186] S. Vyazovkin, A. K. Burnham, J. M. Criado, L. A. Pérez-Maqueda, C. Popescu, and N. Sbirrazzuoli, “ICTAC Kinetics Committee recommendations for performing kinetic computations on thermal analysis data,” *Thermochim.*

Acta, vol. 520, no. 1–2, pp. 1–19, 2011.

[187] S. Krishnaswamy, D. Bhattacharyya, H. Abhyankar, V. Marchante, Z. Huang, and J. Brighton, "Morphological, optical and thermal characterisation of aerogel-epoxy composites for enhanced thermal insulation," *J. Compos. Mater.*, 2018.

[188] Hexion Inc., "EPIKOTE Resin MGS RIMR 135 and EPIKURE Curing Agent MGS RIMH 134–RIMH 137," *Technical Data Sheet*, 2006. [Online]. Available: http://www.metyx.com/wp-content/uploads/PDF_Files/Hexion/TDS/TDS RIMH 137.pdf. [Accessed: 20-Jan-2018].

[189] A. R. Buzykaev, A. F. Danilyuk, S. F. Ganzhur, E. A. Kravchenko, and A. P. Onuchin, "Measurement of optical parameters of aerogel," *Nucl. Instruments Methods Phys. Res. Sect. A Accel. Spectrometers, Detect. Assoc. Equip.*, vol. 433, no. 1–2, pp. 396–400, Aug. 1999.

[190] D. Bhattacharyya, M. Targa, and J. R. Nicholls, "Electron beam physical vapour deposited zirconia based ceramics for developments of solar surface coatings," *Surf. Eng.*, vol. 28, no. 2, pp. 122–128, Mar. 2012.

[191] Epoxy Technology, "Understanding Optical Properties for Epoxy Applications," *Tech Tip 18*, 2012. [Online]. Available: http://www.epotek.com/site/files/Techtips/pdfs/tip18.pdf. [Accessed: 10-Jan-2018].

[192] C. D. Fernandes, J. C. Bridges, and M. M. Grady, "UV and Visible Wavelength Reflectance Spectroscopy of Aerogel and of Stardust Grains," *Lunar Planet. Sci.*, vol. XXXVIII, 2007.

[193] S. Krishnaswamy, H. Abhyankar, V. Marchante, Z. Huang, and J. Brighton,

"Aerogel/epoxy thermal coatings for carbon fibre reinforced plastic substrates," *J. Adhes. Sci. Technol.*, 2019.

[194] Physik Instrumente, "Piezo Ceramic Materials and Products," *Piezo Materials & Components*, 2011. [Online]. Available: http://www.piezo.ws/pdf/Piezo_Materials_Piezo_Technology_Piezo_Components.pdf. [Accessed: 02-Jan-2018].

[195] P. Gijsman, W. Dong, A. Quintana, and M. Celina, "Influence of temperature and stabilization on oxygen diffusion limited oxidation profiles of polyamide 6," *Polym. Degrad. Stab.*, vol. 130, pp. 83–96, Aug. 2016.

[196] M. Jabbari, D. Akesson, M. Skrifvars, and M. J. Taherzadeh, "Novel lightweight and highly thermally insulative silica aerogel-doped poly(vinyl chloride)-coated fabric composite," *J. Reinf. Plast. Compos.*, vol. 34, no. 19, pp. 1581–1592, 2015.

[197] C. Viazzi, J. P. Bonino, and F. Ansart, "Synthesis by sol-gel route and characterization of Yttria Stabilized Zirconia coatings for thermal barrier applications," *Surf. Coatings Technol.*, vol. 201, no. 7, pp. 3889–3893, Dec. 2006.

[198] C. Viazzi, A. Deboni, J. Zoppas Ferreira, J.-P. Bonino, and F. Ansart, "Synthesis of Yttria Stabilized Zirconia by sol–gel route: Influence of experimental parameters and large scale production," *Solid State Sci.*, vol. 8, no. 9, pp. 1023–1028, Sep. 2006.

[199] A. Kavitha, N. S. Subaramanian, and S. Vadivel, "Influence of Sol Concentration on the Properties of Spin Coated Zirconia Thin Films," *IOP Conf. Ser. Mater. Sci. Eng.*, vol. 73, p. 012005, Feb. 2015.

[200] X. Xu, C. Xia, S. Huang, and D. Peng, "YSZ thin films deposited by spin-

coating for IT-SOFCs," *Ceram. Int.*, vol. 31, no. 8, pp. 1061–1064, Jan. 2005.

[201] B. Harris, H. Reiter, T. Adam, R. Dickson, and G. Fernando, "Fatigue behaviour of carbon fibre reinforced plastics," *Composites*, vol. 21, no. 3, pp. 232–242, 1990.

[202] S. A. Michel, R. Kieselbach, and H. J. Martens, "Fatigue strength of carbon fibre composites up to the gigacycle regime (gigacycle-composites)," *Int. J. Fatigue*, vol. 28, no. 3, pp. 261–270, 2006.

[203] P. I. Karkanas and I. K. Partridge, "Cure modeling and monitoring of epoxy/amine resin systems. I. Cure kinetics modeling," *J. Appl. Polym. Sci.*, vol. 77, no. 7, pp. 1419–1431, Aug. 2000.

APPENDIX I

Coating a C/Ep Composite with YSZ- Experiment Report

Aim

The aim of this experiment was to successfully coat a carbon/epoxy composite with an YSZ sol-gel using HCl as a catalyst.

Procedure

The chemicals used for this experiment were:

- YSZ (Yttria Stabilised Zirconia)
- Ethanol
- TEOS (Tetraethyl Orthosilicate)
- Distilled Water
- HCl (Hydrochloric Acid)

Sol-gel Preparation

To prepare the sol, 2ml of TEOS was mixed with 6ml of Ethanol, 8ml of water and 2 drops (approximately 0.002 ml) of HCl whilst stirring at 350 rpm. After the chemicals were added the stirring speed was increased to 1100 rpm for 5 minutes. Then 0.6gms of YSZ powder was added to the mixture and then the solution was allowed to react at 70°C with 700rpm for 2.5 hours. After this the stirring was stopped but the heating was continued for a further 90 mins.

Drying

To dry the solution, the temperature was increased to 135^0C and the stirring was resumed (at 700 rpm) (Figure A 1). After 70 mins, the stirring was again stopped and the temperature was increased by another 10^0C (145^0C). This setup was continued for another hour, after which, the heating was stopped and the sol was left at room

temperature overnight (approximately 18 hrs). Figure A 2 shows the sedimentation of YSZ after it was left overnight

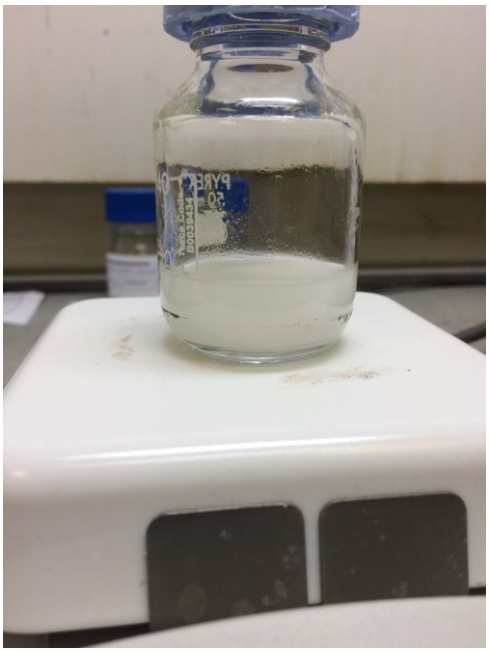

Figure A 1 Drying of the sol-gel

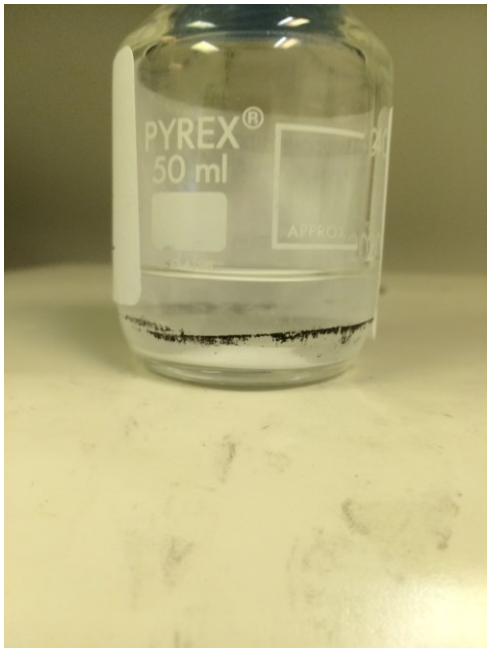

Figure A 2 YSZ sedimentation after leaving the mixture overnight

Figure A 3 Sol-gel after heat treatment

The mixture was again stirred at 700 rpm and reheated to 140^{0}C for a further 6 hrs (Figure A 3) and left at room temperature for 67 hrs and 40 mins. The solution was then physically shaken by hand and left again for another 12 hrs. Finally the solution was stirred at 1100 rpm at room temperature for 2hrs and 35 mins (Figure A 4 and Figure A 5 show the sol-gel before and after stirring respectively). The solution was then coated onto the carbon/epoxy substrate using a spin coater (Figure A 6).

Figure A 4 sample showing the sedimentation of YSZ

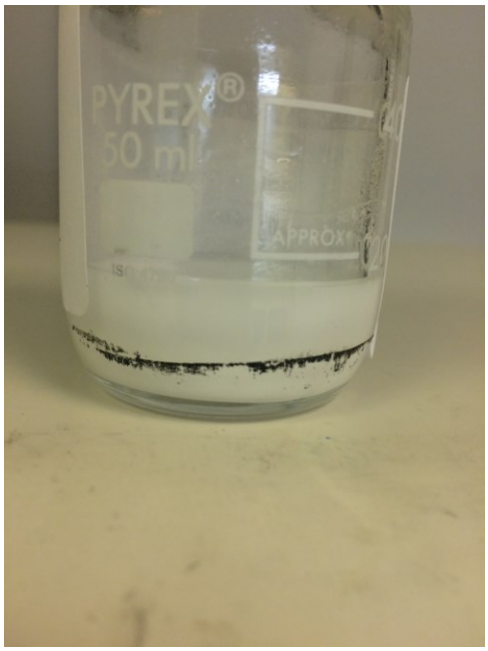

Figure A 5 sol-gel after the final stirring

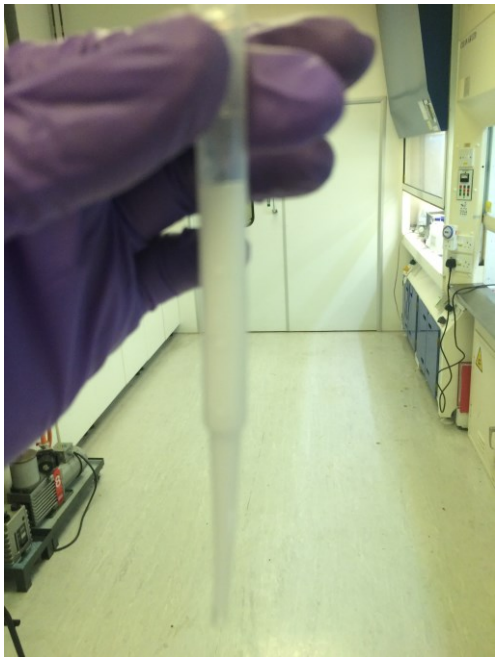

Figure A 6 sol-gel prior to coating

Three samples were coated in this batch:

1) B2: 400 rpm for 90 seconds (Figure A 7)
2) B3: 600 rpm for 60 seconds (Figure A 8)
3) B4: 500 rpm for 40 seconds and 1000 rpm for 60 seconds (Figure A 9)

All the samples had acceleration and deceleration time of 3 seconds and were heated at 100°C for 10 minutes to evaporate the solvents.

Figure A 7 Sample B2

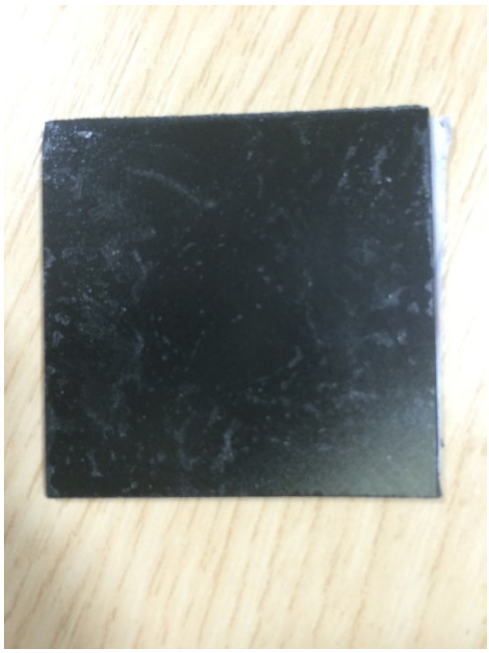

Figure A 8 Sample B3

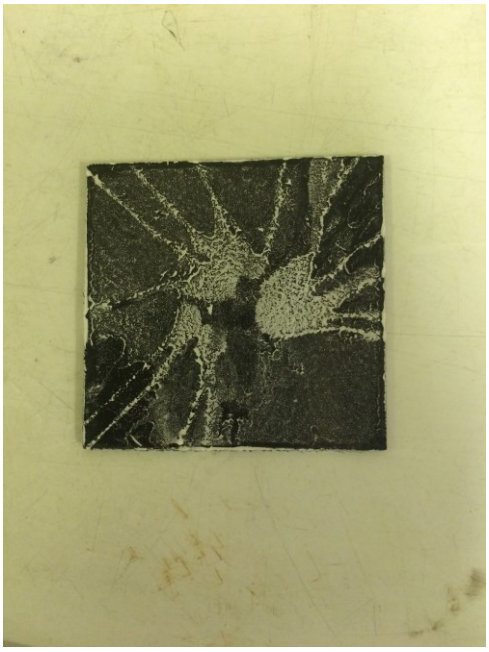

Figure A 9 Sample B4

Observation

There was no bubbling during the heating of the sol-gel suggesting that the constituents did not evaporate. Additionally, after leaving the sample without stirring for some period of time, precipitation of the YSZ particles was observed but the solution was made homogenous by just shaking/agitating the solution by hand; suggesting that the YSZ particles does not dissolve in the solution.

When considering the coating on the composites, it is seen that the coating in all three cases show better adhesion to the substrate compared to the previous batch and that they are more uniformly dispersed. It is also believed that sample B4 had the best adhesion properties (but this has to be confirmed by further testing).

Inference

The solution was homogenous and able to dissipate the YSZ particles uniformly within it. However, the latter showed sedimentation after leaving the solution without stirring. Nevertheless because the solution was initially homogenous, the coating on

the composite substrate was uniform. It is also seen that the different coating parameters also affect the final coating properties with the two-stage coating showing the most promising results.

But it must be noted that there was no formation of a sol-gel network and the coating was if anything, just YSZ particles. It is believed that the absence of sol-gel could be put down to the low temperatures used.

Conclusion

Although the coating is no means perfect at this stage, there is an improvement from the previous batch of sol-gel; the solution was more homogenous and the coating itself was more uniform and adhesive.

Additionally, the two stage coating process shows a lot of potential. However, it believed that the coating has to be characterized to identify the reaction (if any) between the solvents to further understand and improve its chemistry.

APPENDIX II

MATLAB code to compare the Sestak-Beggeren model with the experimental data

The code is defined only for the pure epoxy sample but could easily be adapted to the other materials in the study as well.

```
%Read Experimental Values from Excel Spreadsheet
clc
dadt5 = xlsread('Epoxy5.xlsx','J3:J2378');
a5 = xlsread('Epoxy5.xlsx','F3:F2378');
T5 = xlsread('Epoxy5.xlsx','I3:I2378');

dadt10 = xlsread('Epoxy10.xlsx','J3:J1200');
a10 = xlsread('Epoxy10.xlsx','F3:F1200');
T10 = xlsread('Epoxy10.xlsx','I3:I1200');

dadt15 = xlsread('Epoxy15.xlsx','J3:J860');
a15 = xlsread('Epoxy15.xlsx','F3:F860');
T15 = xlsread('Epoxy15.xlsx','I3:I860');


dadt20 = xlsread('Epoxy20.xlsx','J3:J643');
a20 = xlsread('Epoxy20.xlsx','F3:F643');
T20 = xlsread('Epoxy20.xlsx','I3:I643');


%Plot dadt vs Temperature as scatter plots
figure;
hold on;

a1 = scatter(T5,dadt5,30,'o','k')
a2 = scatter(T10,dadt10,30,'d','k')
a3 = scatter(T15,dadt15,30,'s','k')
a4 = scatter(T20,dadt20,30,'p','k')

%Define the model parameters derived previously
R = 8.31447;
Ea = (53.04*1000);
n5 = 1.86;
m5 = 0.16;
A = 15.51;

%Build the model at different heating rates using the model
parameters at different values of a
for k = 1:1:2376
   e5(k,1) = ((exp((-Ea)/(R*(T5(k,1)+273.15)))));
   d5(k,1) = ((1-a5(k,1))^n5)*(a5(k,1)^m5);
   da5(k,1) = (exp(A)*(e5(k,1))*d5(k,1));
end

for k = 1:1:1198
   e10(k,1) = ((exp(-Ea/(R*(T10(k,1)+273.15)))));
```

```
   d10(k,1) = ((1-a10(k,1))^n5)*(a10(k,1)^m5);
   da10(k,1) = (exp(A)*(e10(k,1))*d10(k,1));
end

for k = 1:1:858
   e15(k,1) = ((exp(-Ea/(R*(T15(k,1)+273.15)))));
   d15(k,1) = ((1-a15(k,1))^n5)*(a15(k,1)^m5);
   da15(k,1) = (exp(A)*(e15(k,1))*d15(k,1));
end

for k = 1:1:641
   e20(k,1) = ((exp(-Ea/(R*(T20(k,1)+273.15)))));
   d20(k,1) = ((1-a20(k,1))^n5)*(a20(k,1)^m5);
   da20(k,1) = (exp(A)*(e20(k,1))*d20(k,1));
end

%Plot the model against the experimental values and compare
p1 = plot(T5,da5,'-r','LineWidth',2)
p2 = plot(T10,da10,'--r','LineWidth',2)
p3 = plot(T15,da15,'-.r','LineWidth',2)
p4 = plot(T20,da20,':r','LineWidth',2)

%Define the plot parameters
legend([a1,a2,a3,a4,p1,p2,p3,p4],{'5C/min Experimental','10C/min
Experimental','15C/min Experimental','20C/min Experimental','5C/min
Model','10C/min Model','15C/min Model','20C/min
Model'},'Location','northeast');
axis([30,275,0,0.3]);
grid off;
xlabel('Temperature(\circC)','FontSize',20);
ylabel('d\alpha/dt','FontSize',20);
```

APPENDIX III

Reduced Input Deck for Dual Coated sample subjected to cyclic load

LS-DYNA .k file

```
LS-DYNA keyword deck by LS-PrePost
*CONTROL_SOLID
$#   esort   fmatrix   niptets    swlocl    psfail   t10jtol
icohed    tet13k
         1         0         4         2         0       0.0
0         0
$#   pm1     pm2     pm3     pm4     pm5     pm6     pm7     pm8
pm9    pm10
       0       0       0       0       0       0       0       0
0       0
*CONTROL_SOLUTION
$#    soln       nlq     isnan     lcint
         1         0         0       100
*CONTROL_TERMINATION
$#  endtim    endcyc     dtmin    endeng    endmas
    1800.0         0       0.0       0.01.000000E8
*CONTROL_THERMAL_SOLVER
$#   atype     ptype    solver     cgtol       gpt    eqheat
fwork       sbc
         1         0         31.00000E-8         8       1.0
1.0       0.0
$#  msglvl    maxitr    abstol    reltol     omega    unused
unused       tsf
         0       5001.0000E-101.00000E-4       1.0
1.0
*CONTROL_THERMAL_TIMESTEP
$#      ts       tip       its      tmin      tmax     dtemp
tscp      lcts
         0       1.0       0.1       0.0       0.0       1.0
0.5         0
*DATABASE_BINARY_D3PLOT
$#      dt      lcdt      beam     npltc    psetid
       1.0         0         0         0         0
$#   ioopt
         0
*BOUNDARY_TEMPERATURE_SET
$#    nsid      lcid     cmult       loc
         1         1       1.0         1
*CONTACT_AUTOMATIC_SURFACE_TO_SURFACE_SMOOTH_THERMAL
$#     cid
title
$#    ssid      msid     sstyp     mstyp    sboxid    mboxid
spr       mpr
         1         2         3         3         0         0
0         0
$#      fs        fd        dc        vc       vdc    penchk
bt        dt
       0.0       0.0       0.0       0.0       0.0         0
0.01.00000E20
$#     sfs       sfm       sst       mst      sfst      sfmt
fsf       vsf
       1.0       1.0       0.0       0.0       1.0       1.0
1.0       1.0
```

```
$#      cf      frad       htc      lmin      lmax    ftoslv
bc_flg      algo
       0.0       0.0     100.02.00000E-4       1.0       0.5
0         0
*CONTACT_AUTOMATIC_SURFACE_TO_SURFACE_SMOOTH_THERMAL_ID
$#     cid
title
         2
$#    ssid      msid     sstyp     mstyp    sboxid    mboxid
spr       mpr
         1         3         3         3         0         0
0         0
$#      fs        fd        dc        vc       vdc    penchk
bt        dt
       0.0       0.0       0.0       0.0       0.0         0
0.01.00000E20
$#     sfs       sfm       sst       mst      sfst      sfmt
fsf       vsf
       1.0       1.0       0.0       0.0       1.0       1.0
1.0       1.0
$#      cf      frad       htc      lmin      lmax    ftoslv
bc_flg      algo
       0.0       0.0     100.02.00000E-4       1.0       0.5
0         0
*PART
$#
title
CFRP
$#     pid     secid       mid     eosid      hgid      grav
adpopt      tmid
         1         1         0         0         0         0
0         1
*SECTION_SOLID_TITLE
Solid
$#   secid    elform       aet
         1         3         0
*PART
$#
title
Coating Top
$#     pid     secid       mid     eosid      hgid      grav
adpopt      tmid
         2         1         0         0         0         0
0         2
*PART
$#
title
Coating Bottom
$#     pid     secid       mid     eosid      hgid      grav
adpopt      tmid
         3         1         0         0         0         0
0         2
*MAT_THERMAL_ORTHOTROPIC_TITLE
CFRP
$#    tmid       tro     tgrlc    tgmult      aopt      tlat
hlat
         1    1460.0         0       0.0       0.0       0.0
0.0
$#      hc        k1        k2        k3
    1170.0     14.57     14.57      0.75
$#      xp        yp        zp        a1        a2        a3
```

```
       0.0       0.0       0.0       0.0       0.0       0.0
$#      d1        d2        d3
       0.0       0.0       0.0
*MAT_THERMAL_ISOTROPIC_TITLE
Coating
$#    tmid       tro     tgrlc    tgmult      tlat      hlat
         2    968.45       0.0       0.0       0.0       0.0
$#      hc        tc
    1934.1   0.20015
*INITIAL_TEMPERATURE_SET
$#    nsid      temp       loc
         2      23.0         0
*DEFINE_CURVE_TITLE
Temperature
$#    lcid      sidr       sfa       sfo      offa      offo
dattyp     lcint
         1         0       1.0       1.0       0.0       0.0
0         0
$#                a1                  o1
                0.0                 0.0
               10.0                50.0
               20.0               -50.0
               30.0                50.0
               40.0               -50.0
               50.0                50.0
               60.0               -50.0
               70.0                50.0
               80.0               -50.0
               90.0                50.0
              100.0               -50.0
              110.0                50.0
              120.0               -50.0
              130.0                50.0
              140.0               -50.0
              150.0                50.0
              160.0               -50.0
              170.0                50.0
              180.0               -50.0
              190.0                50.0
              200.0               -50.0
              210.0                50.0
              220.0               -50.0
              230.0                50.0
              240.0               -50.0
              250.0                50.0
              260.0               -50.0
              270.0                50.0
              280.0               -50.0
              290.0                50.0
              300.0               -50.0
              310.0                50.0
              320.0               -50.0
              330.0                50.0
              340.0               -50.0
              350.0                50.0
              360.0               -50.0
              370.0                50.0
              380.0               -50.0
              390.0                50.0
              400.0               -50.0
              410.0                50.0
```

420.0	-50.0
430.0	50.0
440.0	-50.0
450.0	50.0
460.0	-50.0
470.0	50.0
480.0	-50.0
490.0	50.0
500.0	-50.0
510.0	50.0
520.0	-50.0
530.0	50.0
540.0	-50.0
550.0	50.0
560.0	-50.0
570.0	50.0
580.0	-50.0
590.0	50.0
600.0	-50.0
610.0	50.0
620.0	-50.0
630.0	50.0
640.0	-50.0
650.0	50.0
660.0	-50.0
670.0	50.0
680.0	-50.0
690.0	50.0
700.0	-50.0
710.0	50.0
720.0	-50.0
730.0	50.0
740.0	-50.0
750.0	50.0
760.0	-50.0
770.0	50.0
780.0	-50.0
790.0	50.0
800.0	-50.0
810.0	50.0
820.0	-50.0
830.0	50.0
840.0	-50.0
850.0	50.0
860.0	-50.0
870.0	50.0
880.0	-50.0
890.0	50.0
900.0	-50.0
910.0	50.0
920.0	-50.0
930.0	50.0
940.0	-50.0
950.0	50.0
960.0	-50.0
970.0	50.0
980.0	-50.0
990.0	50.0
1000.0	-50.0
1010.0	50.0
1020.0	-50.0

1030.0	50.0
1040.0	-50.0
1050.0	50.0
1060.0	-50.0
1070.0	50.0
1080.0	-50.0
1090.0	50.0
1100.0	-50.0
1110.0	50.0
1120.0	-50.0
1130.0	50.0
1140.0	-50.0
1150.0	50.0
1160.0	-50.0
1170.0	50.0
1180.0	-50.0
1190.0	50.0
1200.0	-50.0
1210.0	50.0
1220.0	-50.0
1230.0	50.0
1240.0	-50.0
1250.0	50.0
1260.0	-50.0
1270.0	50.0
1280.0	-50.0
1290.0	50.0
1300.0	-50.0
1310.0	50.0
1320.0	-50.0
1330.0	50.0
1340.0	-50.0
1350.0	50.0
1360.0	-50.0
1370.0	50.0
1380.0	-50.0
1390.0	50.0
1400.0	-50.0
1410.0	50.0
1420.0	-50.0
1430.0	50.0
1440.0	-50.0
1450.0	50.0
1460.0	-50.0
1470.0	50.0
1480.0	-50.0
1490.0	50.0
1500.0	-50.0
1510.0	50.0
1520.0	-50.0
1530.0	50.0
1540.0	-50.0
1550.0	50.0
1560.0	-50.0
1570.0	50.0
1580.0	-50.0
1590.0	50.0
1600.0	-50.0
1610.0	50.0
1620.0	-50.0
1630.0	50.0

1640.0	-50.0
1650.0	50.0
1660.0	-50.0
1670.0	50.0
1680.0	-50.0
1690.0	50.0
1700.0	-50.0
1710.0	50.0
1720.0	-50.0
1730.0	50.0
1740.0	-50.0
1750.0	50.0
1760.0	-50.0
1770.0	50.0
1780.0	-50.0
1790.0	50.0
1800.0	-50.0
1810.0	-50.0

And no one sings me lullabies

And no one makes me close my eyes

So I throw the windows wide

And call to you across the sky

- Echoes (Pink Floyd)